Polarisation Effects of Exciton Migration and Singlet Fission in TIPS-Pentacene Nanoparticles

Elisabeth Schrefl

B.Sc. (Advanced)

A thesis submitted in partial fulfilment of the requirements for the degree of Master of Philosophy (Chemical Science)

November 2018

Department of Chemistry
The University of Adelaide
North Terrace Campus
Adelaide, South Australia 5005

Contents

Abstract

Converting solar energy into electricity using photovoltaic (PV) cells is a renewable and environmentally friendly way to meet the world's energy requirements. One of the major shortcomings of conventional solar cells is their 34% theoretical efficiency limit. Singlet fission (SF) may be exploited to increase this limit to 46%. SF can split the energy of a high-energy photon by producing two triplet excited states (excitons) from one singlet exciton. This process enables the excess energy above the band gap of the PV material to be harvested rather than being lost through thermal relaxation. However, many aspects of the SF process are still heavily debated and further research is required to exploit its full potential. Molecular arrangement, or morphology, affects the electronic coupling between molecules and is known to be critical in obtaining a high SF yield. Morphology also influences exciton migration, which is important because singlet migration can limit SF, and triplet migration to a donor-acceptor interface is essential for harvesting triplets. Therefore, the morphology of a SF layer must be optimised for favourable coupling between chromophores to allow for complete SF as well as efficient exciton migration. Previous research has focused on exploring the effect of average interchromophore separation on the SF rate and yield by studying amorphous 6,13-bis(triisopropylsilylethynyl) pentacene (TIPS-Pn) nanoparticles (NPs). By embedding TIPS-Pn in an amorphous polymer matrix, the mass ratio of TIPS-Pn to the host polymer can be varied to change the average intermolecular TIPS-Pn separation. Here, we present ultrafast time-resolved fluorescence and transient absorption (TA) polarisation anisotropy to investigate exciton migration in this system. We also developed a Monte Carlo (MC) simulation to offer insight into singlet migration and SF in these NPs. Our analyses show that diffusion-limited SF acts to increase (or suppress the decay of) the fluorescence anisotropy in an amorphous system. Furthermore, we find that with the SF model employed in our MC simulation, the experimental fluorescence and anisotropy data can only be reproduced by assuming that the TIPS-Pn molecules form amorphous clusters within the NP systems. The data presented in this thesis highlight the applications of time-resolved polarisation anisotropy which, along with a MC simulation, provides a means to model and analyse the dependence of morphology on SF and exciton migration in amorphous systems.

Declaration

I certify that this work contains no material which has been accepted for the award of any other degree or diploma in my name, in any university or other tertiary institution and, to the best of my knowledge and belief, contains no material previously published or written by another person, except where due reference has been made in the text. In addition, I certify that no part of this work will, in the future, be used in a submission in my name, for any other degree or diploma in any university or other tertiary institution without the prior approval of the University of Adelaide and where applicable, any partner institution responsible for the joint-award of this degree.

I give permission for the digital version of my thesis to be made available on the web, via the University's digital research repository, the Library Search and also through web search engines, unless permission has been granted by the University to restrict access for a period of time.

I acknowledge the support I have received for my research through the provision of an Australian Government Research Training Program Scholarship.

Elisabeth Schrefl
November 2018

Acknowledgements

I would like to thank all the people who have helped me throughout the last two years of my master's degree. Firstly, I am incredibly grateful to my supervisor Assoc. Prof. Tak W. Kee, for his knowledge, guidance and patience. Thank you also to my co-supervisors Assoc. Prof. David M. Huang and Prof. Gregory F. Metha. To Dr. Patrick Tapping, thank you for your invaluable skills and knowledge, and your incredible willingness to help. I have to especially acknowledge the handy LaTeX template, his countless plotting scripts, and all his assistance with data collection and analysis.

The MC simulation in this Thesis was based on a previous simulation of exciton migration by Patrick. Jessica M. de la Perrelle then modified the simulation for the NP systems studied here, during her undergraduate research placement and summer research scholarship. The simulation turned out to be a key part of this Thesis, and for that I cannot thank Jess enough. I'd like to extend my thanks to the all the Kee group members. Especially to Alex, who taught me how to make the NPs and use various equipment. She also guided me with data analysis and kept me sane with her ongoing positive attitude.

I would also like to acknowledge the Sumby/Doonan/Keene group for the continuous supply of distilled THF and Matthew Bull for letting me invade the teaching labs to use the steady-state spectrometers.

Lastly, I'd like to thank my family and friends, for always being there to support me.

Abbreviations

2D two-dimensional

3D three-dimensional

ΔA change in absorbance

BBO β-barium borate

CO-520 poly(oxyethylene)nonylphenylether

DET Dexter excitation transfer

EET excitonic energy transfer

ES electrostatic

ESA excited-state absorption

FRET Förster resonance energy transfer

FWHM full width half maximum

GSB ground-state bleach

HPLC high-performance liquid chromotography

IRF instrument response function

ISC intersystem crossing

LJ Lennard-Jones

MC Monte Carlo

MD molecular dynamics

MEG multiple exciton generation

MSD mean squared displacement

NIR near-infrared

NP nanoparticle

OPA optical parametric amplifier

P3HT poly(3-hexylthiophene)

PBC periodic boundary condition

PMMA poly(methyl methacrylate)

Pn pentacene

PV photovoltaic

SE stimulated emission

SF singlet fission

SFG sum frequency generation

SQ Shockley-Queisser

TA transient absorption

TCSPC time-correlated single photon counting

THF tetrahydrofuran

TIBS-Pn 6,13-bis(triisobutylsilylethynyl) pentacene

TIPS triisopropylsilylethnyl

TIPS-Pn 6,13-bis(triisopropylsilylethynyl) pentacene

TPES total primary energy supply

UC upconversion

UV ultraviolet

UV-Vis ultraviolet-visible

VDW van der Waals

List of Figures

List of Tables

CHAPTER 1
Introduction

1.1 Photovoltaics

The world's demand for energy supply is continuously increasing, with the world total primary energy supply (TPES) having more than doubled in the last 40 years.[1] Fossil fuels (oil, coal and natural gas) are still the dominant source of energy generation, accounting for 81% of the world TPES in 2016.[1]

Fossil fuels have until now been cheap and supported the world's growing energy needs. However, fossil fuels are non-renewable, meaning their supply is limited. It has been predicted that the economically viable reserves of oil and gas will become depleted in the next 25 years, and coal within the next 100 years.[2] At the same time, the world's energy needs have been predicted to double within the next 50 years.[3] Additionally, the combustion of fossil fuels results in release of carbon dioxide (CO_2) into the atmosphere, which has been widely regarded as a leading cause of climate change.[4,5] Consequently, due to the environmental concerns of climate change and depleting fossil fuel supply, clean and renewable energy sources have begun to emerge.

Solar energy is the world's most abundant energy resource, dwarfing all fossil fuel and renewable energy resources combined.[6] In fact, more energy from sunlight hits the Earth's surface in a single hour than is consumed by humans in an entire year.[6] Effectively and economically harvesting even a fraction of this solar energy would meet the world's growing energy consumption needs.

Sunlight can be harvested and converted into electricity by means of photovoltaics (PVs), also known as solar cells. Single-junction solar cells contain only one absorbing material, known as the "active material". Upon absorption of a photon of equal or greater energy than the band gap of the active material, an excited electron is produced. By separating it from the positively charged vacancy, or "hole", current is generated. The most widespread single-junction solar cells contain silicon as the active material.[7] However, solar cells currently only account for $\sim$1.3% of the world's domestic electricity generation.[1] Solar cells must be economically competitive with fossil fuels to become a viable option to sustain the world's energy requirements. Achieving this would require reduction in manufacturing, installation and operational costs, as well as advances in material research and cell design to increase device efficiency and stability.[8]

1.2 The Shockley-Queisser Limit

One of the major shortcomings of single-junction solar cells is their 34% theoretical efficiency limit, known as the Shockley-Queisser (SQ) limit.[9] The maximum theoretical efficiency of a single-junction solar cells with varying band gaps was first calculated and presented by Shockley and Queisser in 1961.[9] In this original paper the maximum theoretical efficiency of 30% was calculated for a band gap of 1.1 eV using a 6000 K black-body spectrum. Later, recalculations with the air-mass 1.5 global spectrum led

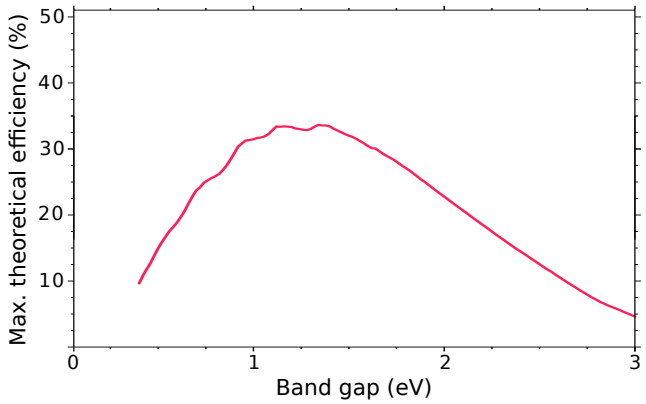

Figure 1.1: The maximum theoretical power conversion efficiency for varying band gap single-junction solar cells according to the SQ limit.[12]

to a maximum theoretical efficiency of 33.7% for an optimum band gap of 1.34 eV, as shown in Figure 1.1.[10,11]

The SQ limit arises because photons with energy less than the band gap of the absorber material remain unabsorbed, and those with energy greater than the band gap have excess energy which is lost as heat through thermalisation, or non-radiative decay.[13,14] This is illustrated in Figure 1.2.

To date, the highest efficiency single-junction solar cell is a thin-film gallium-arsenic solar cell with an efficiency of 28.9%.[16] In an effort to surpass the SQ limit, new technologies have emerged. Multi-junction solar cells consist of multiple active layers with different band gaps, thereby allowing absorption of different sections of the solar spectrum.[14] Although they are the best developed so far, their manufacturing complexity results in increased costs.[17] Hot carrier solar cells aim to collect "hot carriers" before thermalisation, to address the issue of excess energy of higher energy photons being lost as heat. However, slowing the thermalisation process to allow for enough time to collect the hot carriers is very difficult.[14] Photon down-conversion is the process of converting high energy photons (of at least twice the band gap) to two lower energy photons,

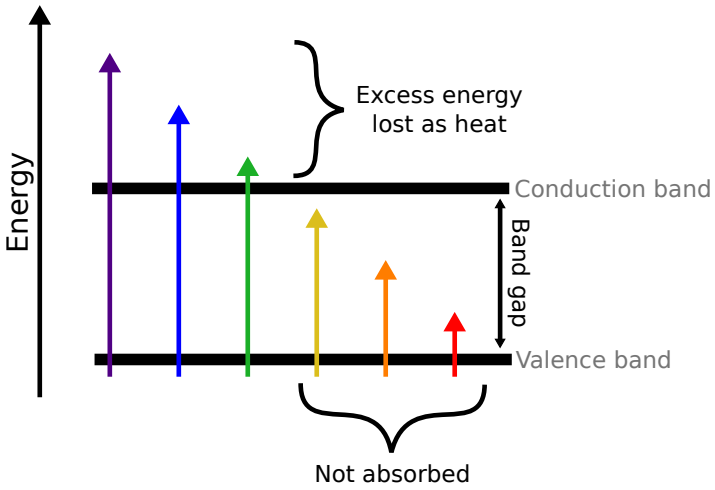

Figure 1.2: The SQ limit arises from two major efficiency losses: lower energy photons not being absorbed (30.6%) and excess energy from higher energy photons being lost through thermal relaxation (22.9%).[15]

while photon up-conversion is the process of absorbing at least two below-band-gap photons and emitting one above-band-gap photon. By pairing a down/up-converting material with a single-junction solar cell, a higher proportion of photons with energy equal to the band gap can be absorbed, effectively increasing the solar cell efficiency. In a similar sense, singlet fission (SF) is a type of multiple exciton generation (MEG) process in organic semiconductors[18] in which a high energy absorbed photon is split into two lower energy excitons capable of charge separation. This process has received much attention in the last decade, as highlighted in various reviews.[13,19–25]

1.3 Singlet Fission

SF is the process in which a molecule in the singlet excited state, S_1, combines with a neighbouring ground-state molecule, S_0, to produce two triplets, T_1. The S_0 and S_1 states are first converted into $^1(TT)$, a pair of triplet states coherently coupled into an overall singlet state, in a spin-allowed process. The correlated triplet-pair, $^1(TT)$, then diffuses apart to produce two first excited triplet states, T_1, which have lost electronic coherence but remain spin-coherent for longer times. This process can be represented by the two-molecule picture as[26]

$$S_0 + S_1 \rightleftharpoons {}^1(TT) \rightleftharpoons T_1 + T_1 \tag{1.1}$$

and is illustrated schematically in Figure 1.3.

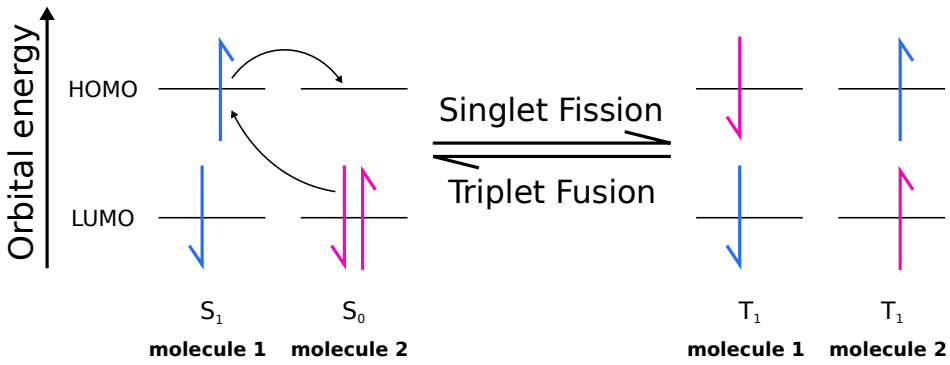

Figure 1.3: A schematic of SF in which a singlet exciton, S_1, and ground-state molecule, S_0, are converted into a pair of triplet excitons, T_1. The reverse process is triplet fusion. Note that the energy axis denotes molecular orbital energies, and not energies of the molecular spin states. Typically, an efficient SF molecule will have $E(S_1) \geq 2E(T_1)$, as discussed in Section 1.3.1.

The first identification of SF was in 1965 in crystalline anthracene.[27] Research spiked with Hanna and Nozik suggesting its potential use to increase the efficiency of solar cells past the SQ limit.[20,25,28]

SF is an effective way to reduce energy loss through thermal relaxation of high energy photons as it provides an alternative pathway to use the excess energy above the band gap of the PV material. This is illustrated in Figure 1.4. The basic idea is to combine a SF layer with a PV layer (such as silicon). A high energy photon passes through the PV layer and upon absorption by the SF layer generates a singlet exciton, S_1. SF then occurs, producing two triplet excitons, T_1. These triplets can be transferred into the PV layer, whose conduction band must be lower than the energy

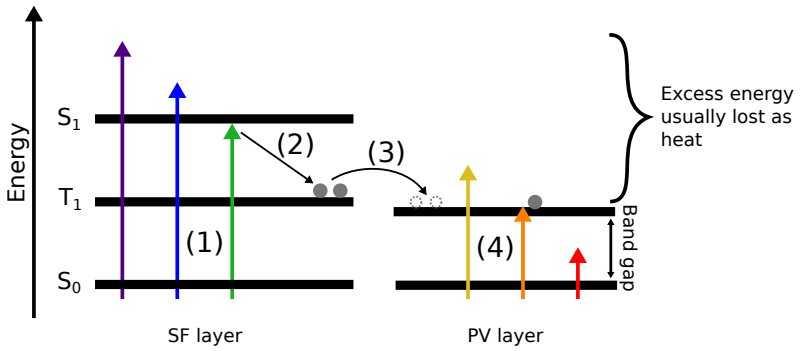

Figure 1.4: Application of SF in solar cells. (1) The higher energy photons pass through the PV layer and are absorbed by the SF layer. (2) SF occurs, producing two triplet excitons. (3) The triplets are transferred to the PV layer. (4) The low band gap PV layer absorbs the lower energy photons.

of the T_1. The lower energy photons are absorbed by the PV layer as usual. In this way, the current is increased without compensation of the voltage.[13,29] SF thereby has the potential to increase the theoretical efficiency limit of solar cells to ~46%.[11,28] as shown by Figure 1.5. Despite this potential, SF solar cells have yet to achieve an efficiency of 5%.[30,31] There are several reasons for this, including the lack of a concrete understanding of the SF mechanism limiting the efficiency of SF process, as well as efficient migration of excitons through the SF layer and the harvesting of triplets by the PV layer.

To effectively implement SF into photovoltaic devices and exploit its full potential, the SF process itself must be efficient. The SF efficiency is determined by the SF quantum yield, defined by the number of triplets produced per singlet,

$$\phi_{SF} = \frac{\max[T_1]}{\max[S_1]}, \tag{1.2}$$

where $[S_1]$ and $[T_1]$ are the concentrations of singlet and triplet excitons, respectively. A SF yield of 2 (i.e. two triplets produced for every singlet) represents completely efficient SF.

The number of known molecules which are able to undergo SF, and produce a reasonable SF yield, are limited due to the strict requirements of SF.

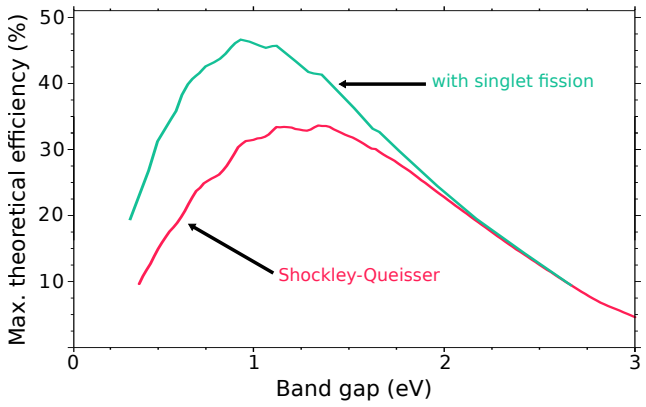

Figure 1.5: The modified maximum theoretical power conversion efficiency for varying band gap single-junction solar cells when SF is used.[12]

1.3.1 Requirements for Effective Singlet Fission

Several requirements are imposed on molecules for them to be able to undergo SF. Firstly, for SF to be faster than competing processes, it is best for SF to be slightly exoergic, which is achieved when the energy of the singlet exciton is greater than or equal to the energy of two triplet excitons, $E(S_1) \geq 2E(T_1)$. In addition, for long lived triplets, triplet annihilation should be slow, which is achieved by the above condition as well as ensuring that the energy of the next highest molecular triplet state is greater than two times the energy of the lowest triplet state, $E(T_2) \geq 2E(T_1)$.[20]

Energy requirements are not the only criterion for efficient SF. For intermolecular SF, the SF rate and yield depend on molecular arrangement and the coupling between molecules,[24,32,33] as will be discussed in Section 1.3.3. For SF to be favourable and out-compete other events including fluorescence, coupling between chromophores must be strong enough to allow for fast enough formation of ^{1}(TT). However, coupling that is too strong results in a bound ^{1}(TT) state and so triplets cannot separate on the available timescale.[20]

SF sensitisers must meet these thermodynamic and coupling requirements, but they should also have strong visible absorption, redox potentials for effective charge separation, long-term stability in light and long triplet lifetimes.[20] Meeting all these requirements is difficult and highly efficient SF has been demonstrated in only a limited amount of molecules.[22] Among the most studied SF sensitisers are tetracene,[34–38] triisopropylsilylethnyl (TIPS) tetracene,[39–41] pentacene[18,30,35,42–49] and pentacene derivatives[50] including 6,13-bis(triisopropylsilylethynyl) pentacene (TIPS-Pn).[31,33,51–64] Intramolecular SF has also been studied in tetracene dimers[65–67] and pentacene dimers.[68–76]

1.3.2 Mechanism of Singlet Fission

Some aspects of the SF mechanism are still not fully understood, including the exact nature of the intermediate triplet-pair, how it forms and how it dissociates.

A study by Korovina et al. showed the triplet-pair in dimers decays to the ground state without forming separated triplets, suggesting that triplet energy transfer from ^{1}(TT) to a nearby molecule is crucial for producing free triplets.[65] Triplet-pair separation was also found to be frustrated in amorphous nanoparticles (NPs),[60] with its separation found to strongly depend on intermolecular coupling.[64] Ultimately, the triplet-pair must dissociate into free triplets which can be harvested individually, in order to increase solar cell efficiencies.

Although strong coupling might facilitate the first part of Equation 1.1 (triplet-pair formation), the second step (dissociation of ^{1}(TT) into free triplets) could be hindered by coupling that is too strong.[19] Consequently, there may exist some ideal coupling strength between chromophores for an overall efficient SF process.

1.3.3 Effect of Morphology on Singlet Fission

Morphology has a profound effect on the coupling of chromophores and thus can significantly impact the SF efficiency.[41,54,55,60,61,64,67,68,77–85] In particular, tuning the intermolecular packing arrangement of chromophores has shown to increase the SF rate by more than an order of magnitude.[68] There has been some debate over whether SF occurs better in crystalline or amorphous systems.[60,83] A study by Pensack et al. demonstrated that SF occurs most rapidly in highly ordered NPs.[54] A later study also

revealed SF to occur rapidly in crystalline NPs, with frustrated triplet-pair separation in amorphous NPs hindering effective SF.[60]

Cofacial slip-stacked chromophores with strong π-π interactions is generally considered optimum for highly efficient SF.[20,25,68,86] Thus, crystalline systems could be advantageous if chromophores are packed in a favourable arrangement. However, as amorphous systems have a higher number of different configurations between neighbouring chromophores, there may be a higher probability of sites which are favourable for SF. Furthermore, inexpensive solution processing (e.g. roll-to-roll printing) has limited control over crystallinity. If effective SF can be obtained with disordered molecular systems, high-efficiency solar cells could be fabricated at a low cost.[87] It is evident that making an informed decision on the morphology of SF materials can help increase the SF yield.

Morphology does not only affect the rate of SF, but also the rate of exciton migration.[88] The rate of exciton migration is important as excitons must migrate to a donor-acceptor interface in order for triplets to be harvested and used to generate photocurrent.[24]

1.4 Exciton Migration Mechanism

Exciton migration occurs through a process called excitonic energy transfer (EET). This can occur through a dipolar coupling mechanism governed by Förster resonance energy transfer (FRET) or an exchange mechanism known as Dexter excitation transfer (DET). These two processes are illustrated in Figures 1.6 and 1.7.

Exciton migration via the FRET process occurs as discrete "hops" between chromophores. Donor and acceptor molecules must be close in space (within $\sim$10 nm), but do not have to be in intimate contact, as no exchange takes place in the resonance energy transfer process. FRET generally occurs for singlets only, because electronic transitions must be spin allowed. Exciton migration via the DET process occurs when donor and acceptor molecules have sufficient orbital overlap, so the molecules must be in very close proximity ($<$10 Å). Because an electron exchange occurs, there are no restrictions on individual molecules, but the combined total spin of the donor and acceptor must be constant. For example, the donor changes from the triplet to singlet state while the acceptor changes from the singlet to triplet state (refer to Figure 1.7). Accordingly, DET is the dominant process for triplet migration.

These two different exciton migration mechanisms can have distinct dependencies on interchromophore separation,[84,89] so morphology is critical in maximising exciton migration.[54,90]

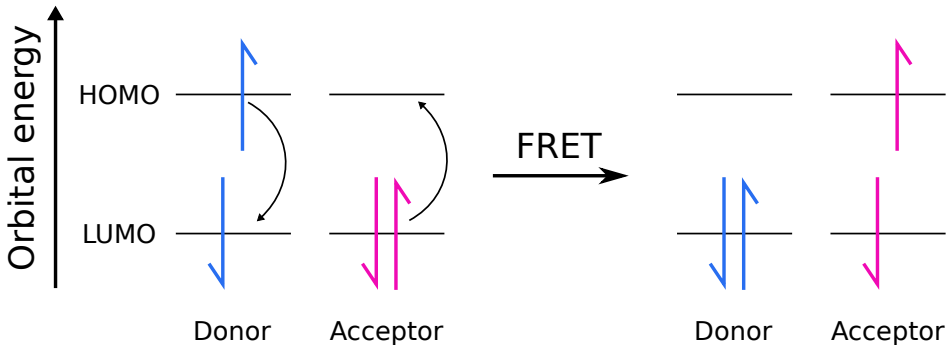

Figure 1.6: A schematic of FRET between a donor and acceptor molecule via a non-radiative dipole coupling mechanism. FRET usually occurs for singlet states as transitions between individual donor and acceptors must be spin-allowed. Note that the energy axis denotes molecular orbital energies, and not energies of the molecular spin states.

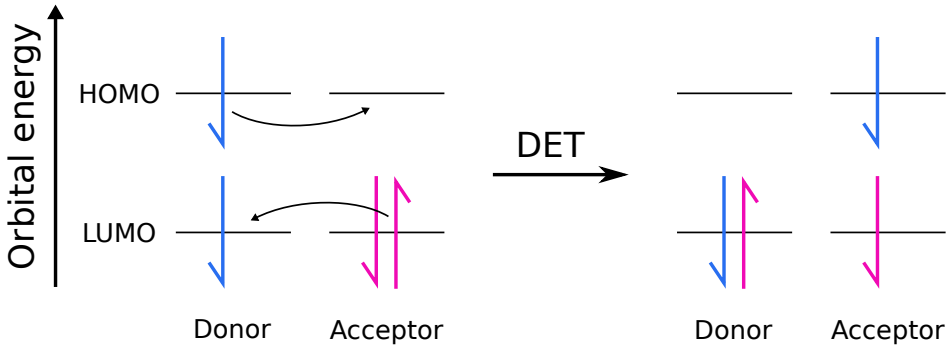

Figure 1.7: A schematic of DET between a donor and acceptor molecule via an electron exchange mechanism. Therefore, the donor and acceptor must be within ~10 Å to allow for sufficient orbital overlap. DET usually occurs for triplet states as the total spin of the donor-acceptor pair must be conserved. Note that the energy axis denotes molecular orbital energies, and not energies of the molecular spin states.

1.4.1 Rate of Singlet and Triplet Migration

The non-radiative singlet energy migration rate between a donor and acceptor, k_{DA}, can be calculated using Fermi's Golden Rule,

$$k_{\mathrm{DA}} = \frac{2\pi}{\hbar} J_{\mathrm{DA}}^2 X_{\mathrm{DA}} \tag{1.3}$$

where X_{DA} is the spectral overlap between the donor and acceptor and can be calculated by integrating over the product of the emission spectrum of the donor and absorption spectrum of the acceptor. J_{DA} is the transition dipole coupling term given by

$$J_{\mathrm{DA}} = \frac{\mu_0^2}{4\pi\varepsilon_{\mathrm{r}}\varepsilon_0} \frac{\hat{r}_{\mathrm{D}} \cdot \hat{r}_{\mathrm{A}} - 3(\hat{R}_{\mathrm{DA}} \cdot \hat{r}_{\mathrm{D}})(\hat{R}_{\mathrm{DA}} \cdot \hat{r}_{\mathrm{A}})}{|R_{\mathrm{D}} - R_{\mathrm{A}}|^3}, \tag{1.4}$$

where μ_0 is the transition dipole moment magnitude, ε_{r} is the relative permittivity of the material, ε_0 is the vacuum permittivity, and $\hat{r}_{\mathrm{D}}$ and $\hat{r}_{\mathrm{A}}$ are the unit transition dipole moment vectors of the donor and acceptor molecules, respectively. $\hat{R}_{\mathrm{DA}}$ is the unit vector between the pair of molecules and $|R_{\mathrm{D}} - R_{\mathrm{A}}|$ is the distance between the molecules. Therefore, the rate of singlet migration depends on the distance between

the donor and acceptor molecules, the alignment of their transition dipoles, and their spectral overlap.

The rate of Dexter energy migration, k_{Dexter}, is given by

$$k_{\text{Dexter}} = \frac{|J_{\text{DA}}^2|}{\hbar}\sqrt{\frac{\pi}{\lambda k_{\text{B}} T}}\exp\left[-\frac{\lambda}{4k_{\text{B}}T}\left(1+\frac{\Delta G}{\lambda}\right)^2\right], \tag{1.5}$$

where J_{DA} is the electronic coupling between the donor and acceptor, λ is the reorganisation energy, T is temperature, k_{B} is the Boltzmann constant, and ΔG is the difference in Gibbs free energy between the donor and acceptor.

1.5 Polarisation Anisotropy

Time-resolved polarisation anisotropy is a technique which can be used to measure exciton migration. In this section, we define anisotropy and describe the causes leading to depolarisation in a homogeneous sample.

1.5.1 Definition of Anisotropy

Consider a partially polarised light travelling in the x direction. The polarised component is defined as $I_z - I_y$. Anisotropy, r, of a light source is defined as the ratio of the polarised component to the total intensity I_{T},

$$r = \frac{I_z - I_y}{I_{\text{T}}} = \frac{I_z - I_y}{I_x + I_y + I_z}. \tag{1.6}$$

When the light is polarised along the z-axis, the emission is symmetric around the z-axis, hence $I_x = I_y$. If we define $I_z = I_{\parallel}$ and $I_y = I_{\perp}$, we arrive at

$$r = \frac{I_{\parallel} - I_{\perp}}{I_{\parallel} + 2I_{\perp}}. \tag{1.7}$$

A more detailed derivation of the anisotropy is given by Lakowicz.[91]

1.5.2 Excitation by Polarised Light

We now consider a sample containing randomly oriented chromophores. Upon illumination of a sample with polarised light, chromophores with absorption transition dipole moments aligned along the electric field vector of the excitation light have the highest probability of excitation. The transition dipole moment of a chromophore does not need to be precisely aligned with the electric field vector to be excited. The probability of excitation is proportional to $\cos^2\theta$, where θ is the angle between the transition dipole moment and the electric field vector of the excitation. This means excitation with polarised light results in photoexcited chromophores with absorption transition moments partially oriented along, and symmetric around, the electric field vector (refer to Figure 1.8). This phenomenon is termed “photoselection”.

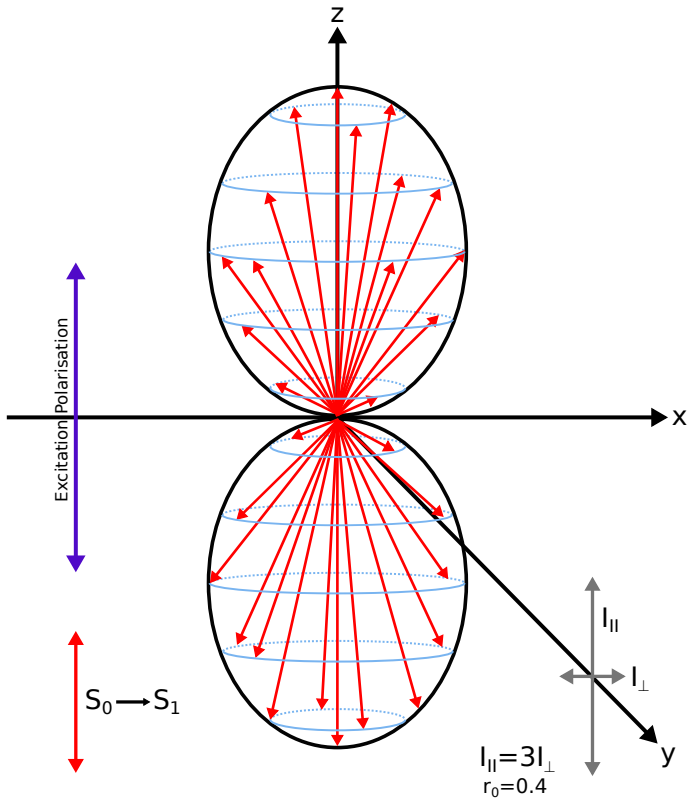

Figure 1.8: Initial excited-state distribution for a system with randomly orientated chromophores, upon excitation with polarised light.

1.5.3 Anisotropy from a Homogeneous Sample

Upon excitation with polarised light, the emission from many samples is also polarised. The extent of the polarisation of the emission relative to the excitation is described in terms of anisotropy, r. A single chromophore, with collinear absorption and emission transition dipoles, that is orientated along the electric field vector of the excitation has an anisotropy of 1. However, the anisotropies are always less than 1 in a homogeneous solution as it is not possible to obtain a perfectly oriented excited-state population (as discussed in Section 1.5.2). The observed anisotropy of the emission of randomly oriented chromophores is therefore calculated using appropriate averaged intensities based on the excitation photoselection ($\frac{2}{5}$) and the measured intensity of the selected chromophores. The anisotropy of selected chromophores depends on the angle between the absorption and emission polarisation. The fundamental anisotropy, r_0, is the anisotropy observed in absence of any depolarisation processes (e.g. rotational diffusion or energy migration). For a sample with randomly oriented chromophores and an angle of β between absorbing and emitting dipole moment directions, the fundamental anisotropy is given by

$$r_0 = \frac{2}{5}\left(\frac{3\cos^2\beta - 1}{2}\right). \tag{1.8}$$

A maximum anisotropy value of 0.4 occurs for fully correlated absorption and emission ($\beta = 0$). The anisotropy takes a negative value of -0.2 if the emission polarisation is rotated 90° relative to the excitation polarisation ($\beta = 90$). An anisotropy value of zero represents emission from completely randomly polarised chromophores, corresponding to an average β of 54.7°, known as the "magic angle".

1.5.4 Causes of Depolarisation

By observing anisotropy over time, one can monitor the depolarisation of the excitons. As excitons become depolarised, their emission also becomes depolarised. This depolarisation from the initial excitation polarisation can occur in various ways.

A common cause of depolarisation is rotational diffusion. Consider a chromophore with collinear absorption and emission dipoles. If the chromophore rotates by some angle β before it emits, the emission from that exciton has become depolarised with respect to the initial excitation polarisation. The anisotropy is given by Equation 1.8. Time-resolved polarisation anisotropy measurements can thus reveal the average angular displacement of chromophores between absorption and emission. The rotational correlation time, θ, of a sphere is the average time for it to rotate one radian, and is given by

$$\theta = \frac{\eta V}{RT}, \tag{1.9}$$

where η is the viscosity, T is temperature in °K, R is the gas constant, and V is the volume of the rotating unit. The angular displacement, θ, is related to the anisotropy by

$$r(t) = r_0 e^{-\frac{t}{\theta}} = r_0 e^{-6Dt}, \tag{1.10}$$

where r_0 is the anisotropy at $t = 0$ and D is the rotational diffusion coefficient ($D = \frac{1}{6\theta}$). It is only spherical molecules which display single exponential anisotropy decay.[91]

Therefore, by measuring the anisotropy of a sample in which only rotational diffusion occurs (i.e. no exciton migration), and in which the spherical chromophores have collinear absorption and emission dipoles, the rotational correlation time can be extracted using Equation 1.10. If the correlation time is much larger than the lifetime ($\theta \gg \tau$), then the effect of rotational diffusion is negligible, and the measured anisotropy, r, at any time, t, is equal to r_0.

Another cause of depolarisation is exciton migration, such as FRET or DET. Excitons are initially correlated with the polarised excitation light. As excitons "hop" between chromophores in a disordered system, the excitons become less correlated with the excitation light (refer to the illustration in Figure 1.9). Measuring the exciton polarisation over time can therefore be a direct observation of the migration of excitons. The presence of energy migration can usually be predicted from the concentration of the sample, and if it is the only cause of depolarisation, time-resolved polarisation anisotropy can reveal the average rate of exciton migration.

The two processes above, rotational diffusion and exciton migration, are two common causes of exciton depolarisation. There is another, more subtle way in which anisotropy can change, namely by preferentially eliminating excitons that are more (less) correlated with the initial exciton polarisation. This selective elimination leaves a population of excitons with less (more) correlation, thus acting to decrease (increase) the overall anisotropy. An example of selective elimination of less polarised excitons can occur through diffusion-limited SF in an amorphous system. This will be explained in more detail in Section 5.1.

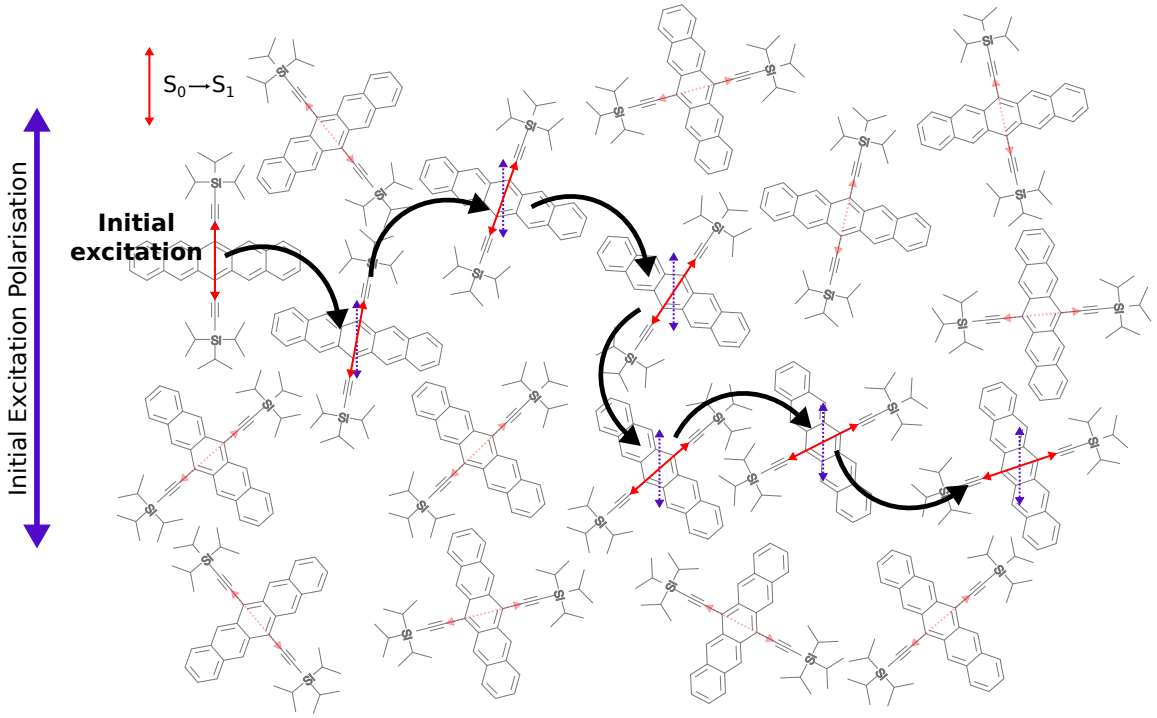

Figure 1.9: The schematic shows excitation of a single TIPS-Pn molecule and migration of the exciton through the system.

1.6 Aims and Research Questions

1.6.1 Previous Research in Our Group

It has been demonstrated that enhanced electronic coupling, gained from short interchromophore separations, results in a higher triplet yield,[33] suggesting that modifying interchromophore separation can be used to adjust the SF efficiency.

Our research group has developed a NP system allowing fine control over the average separation between TIPS-Pn molecules within the NPs. Changing the interchromophore separation has allowed us to explore the effect of electronic coupling on SF rates. TIPS-Pn (shown in Figure 1.10a is an ideal molecule to study, as fast SF has already been identified in solution,[52] film[63] and NPs.[62] Additionally, the TIPS groups make TIPS-Pn soluble in tetrahydrofuran (THF), but not water, allowing formation of aqueous NP suspensions by the reprecipitation method. Poly(methyl methacrylate) (PMMA) (shown in Figure 1.10b was chosen as the host polymer matrix as it has no absorption or emission in the visible spectrum. By embedding TIPS-Pn in an amorphous polymer matrix and varying the mass ratio of TIPS-Pn to polymer, the TIPS-Pn concentration within a NP, and thereby the average intermolecular TIPS-Pn separation, can be controlled. Furthermore, an aqueous suspension of NPs allows continuous sampling of new material, avoiding problems such as photodegradation and inhomogeneity of the sample which are often difficulties encountered when studying films.

Stuart et al. showed that increasing the proportion of polymer, corresponding to a larger average intermolecular TIPS-Pn separation, resulted in a decrease in SF yield.[57]

This decrease in SF efficiency was attributed to a larger amount of singlets requiring to diffuse to a specific site where they can undergo SF, termed "SF site", and an increase in singlet trap sites. Diffusion-limited SF has also been identified in several other studies,[39,87,92] suggesting efficient SF requires specific geometries between the S_0 and S_1 molecules. Stuart et al. further found a significant proportion of the triplet-pair population to decay radiatively, rather than dissociating to separate triplets.[57] This process increased with decreasing average intermolecular TIPS-Pn separation, suggesting that the triplet-pair separation requires molecules close by for triplet to migrate to.[65]

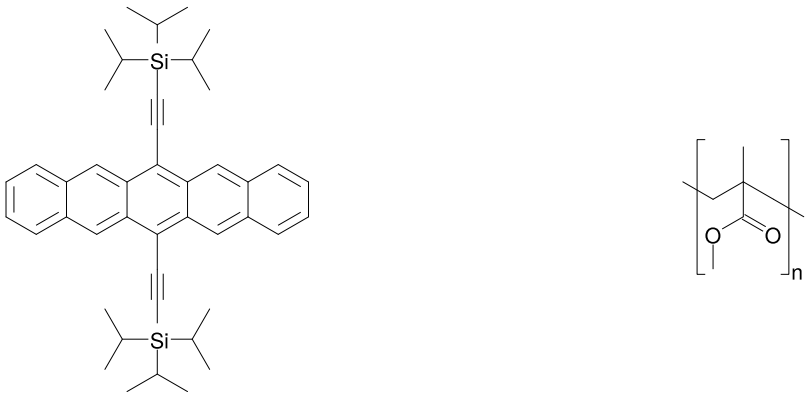

(a) **(b)**

Figure 1.10: Structure of **(a)** triisopropylsilylethnyl pentacene (TIPS-Pn) and **(b)** poly(methyl methacrylate) (PMMA).

1.6.2 Specific Aims

Even though SF is a growing field in research, there are some basic aspects of SF that remain unresolved. Effective implementation of SF in solar cells requires optimising each step in the operation of SF devices. This requires an increased knowledge of the SF mechanism, exciton migration and energy collection. Research has focused heavily on achieving efficient SF. Yet, understanding exciton migration in SF layers is critical for engineering a high-performance SF-based solar cell. This is because singlet migration can limit the rate of SF,[39,57,87,92] and excitons must migrate to a donor-acceptor interface in order for triplets to be harvested and used to generate photocurrent.[24] Consequently, the morphology of the SF layer must be optimised for favourable coupling between chromophores to allow for complete SF as well as efficient exciton migration. To develop new and effective SF materials with an optimal morphology, powerful tools to analyse and understand both the ultrafast SF and exciton migration processes are necessary.

Time-resolved fluorescence and transient absorption (TA) spectroscopy are common techniques for identifying SF, which is characterised by a triplet yield greater than 100%, ultrafast triplet formation, and ground-state bleaching concurrent with a decrease in excited-state singlets and formation of triplets. Specifically, they allow identification of the species involved (S_0, S_1 and T_1) as well as their evolution over time, which can provide valuable insight into the SF mechanism.

Time-resolved polarisation anisotropy measurements are a useful tool in measuring the depolarisation of a sample and can be used to investigate the rate of migration

of excited-state species.[91] There have been some previous SF studies utilising time-resolved polarisation anisotropy measurements.[47,54,55] Tayebjee et al. demonstrated the use of time-resolved fluorescence anisotropy to distinguish between two different morphologies in TIPS-Pn NPs, due to the different rates of singlet migration in amorphous and crystalline-like NPs. Moreover, the long-lived anisotropy component could reveal the presence of exciton trap sites.[55] Similarly, Pensack et al. obtained TA anisotropy decay measurements of the ground-state bleach (GSB) feature of TIPS-Pn NPs and other NPs of pentacene derivatives, to differentiate between the morphology of their NPs. NPs displaying a rapid anisotropy decay were explained to have little long-range order, while those with a slower anisotropy decay were explained to have extensive long-range solid-state order.[54] McDonough et al. presented the first TA anisotropy of pentacene. But, the poor quality anisotropy data did not allow for any other analysis apart from a comment on the magnitude of the anisotropy.[47]

In this thesis, we aim to present a completer picture, obtaining both time-resolved fluorescence and TA magic-angle and anisotropy data of various TIPS-Pn/PMMA NPs with different average intermolecular TIPS-Pn separations. The presented data highlight the usefulness of time-resolved polarisation anisotropy in identifying exciton migration. Additionally, a Monte Carlo (MC) simulation provides a means to model and analyse SF and exciton migration in these amorphous TIPS-Pn/PMMA NPs.

Details of experimental and computational methods are given in Chapter 2. Characteristics of the NPs, as well as evidence that TIPS-Pn does not form crystalline domains within the NPs, are presented in Chapter 3. In Chapter 4, time-resolved fluorescence and TA spectra provide confirmation of the increased SF rate with decreasing average intermolecular TIPS-Pn separation. With the aim of acquiring a better understanding of the system and the exciton migration within the NPs, time-resolved fluorescence and TA polarisation anisotropy measurements were obtained, as presented in Chapter 5. Finally, a MC simulation of the NP systems is presented in Chapter 6, explaining observed trends in the fluorescence anisotropy.

This project will hopefully inspire further utilisation of time-resolved polarisation anisotropy techniques to develop new morphology optimisation strategies for efficient SF and energy migration processes. Controlling and optimising the SF yield and energy migration is a crucial step towards the implementation of SF to construct highly efficient, commercially viable solar cells.

CHAPTER 2
Methods

2.1 Preparation of Aqueous Nanoparticle Suspensions

2.1.1 Materials

6,13-bis(triisopropylsilylethynyl) pentacene (TIPS-Pn) (99.9%) was purchased from Ossila and used as supplied. Poly(methyl methacrylate) (PMMA) (average MW: 120000) and the surfactant poly(oxyethylene)nonylphenylether (CO-520) (average M_n: 441) were purchased from Sigma-Aldrich and also used as supplied. High-performance liquid chromotography (HPLC) grade tetrahydrofuran (THF) was purchased from RCI Labscan and freshly distilled prior to use. Water used in the nanoparticle (NP) preparation was purified with a 18 MΩ Millipore Milli-Q Reagent Water System fitted with a 0.45 µm filter.

2.1.2 Nanoparticle Preparation

An aqueous dispersion of TIPS-Pn/PMMA NPs was prepared by the reprecipitation method, first described by Kasai et al.,[93] and since used for preparation of TIPS-Pn NPs.[50,55,60,64] Briefly, this method involves rapidly injecting a mixture of TIPS-Pn and PMMA in a "good" solvent (THF) into a larger volume of "poor" solvent (water). Because of the miscibility of THF and water, the polymer chains disperse, collapse and fold into roughly spherical particles to minimise unfavourable interactions between the polymer chains and the poor solvent.[94] This process is illustrated in Figure 2.1.

Temperature, solvent and polymer concentration are all determining factors when it comes to the size of NPs prepared by the reprecipitation method. Generally, they are within 10 to a few hundred nanometres.[93,95,96] TIPS-Pn NPs have been reported to be ∼80 nm by Pensack et al. and ∼160 nm by Tayebjee et al.[55,60]

At low concentrations, negative surface charge of NP can provide enough repulsive forces to keep the NP from aggregating and thus keeps them in suspension.[97] As the concentration of the NPs is increased, the repulsive forces become less dominant and so the likelihood of the NPs aggregating and precipitating out of solution increases. To avoid this, surfactants can be used to extend the range of possible NP concentrations and keep them stable.

To achieve the necessary range of TIPS-Pn:PMMA mass ratios while keeping the TIPS-Pn concentration constant, higher mass ratios required surfactant for stabilisation.[57] For consistency, the surfactant (CO-520) used for each NP sample was equal to the total NP concentration (i.e. concentration of TIPS-Pn + PMMA).

The TIPS-Pn/PMMA NPs were prepared as follows. Stock solutions of 400 ppm TIPS-Pn, 400 ppm PMMA and 750 ppm CO-520 in freshly distilled THF were prepared (Note: different concentrations of stock solutions were used for the 1:100 sample, they

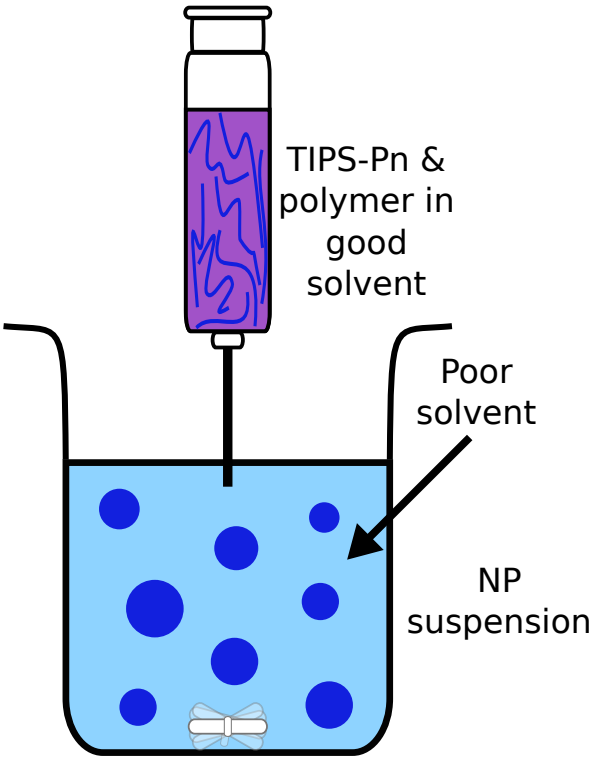

Figure 2.1: Preparation of conjugated polymer NPs by the reprecipitation method. TIPS-Pn/PMMA in a good solvent (THF) is rapidly injected into a poor solvent (water) to form an aqueous NP suspension.

are given in Table 2.1). A volume of each stock solution (given in Table 2.1) was combined to make a 15 mL mixture stock solution of the desired TIPS-Pn:PMMA mass ratio. This was then rapidly injected in 75 mL of vigorously stirred water and left stirring for ∼5 minutes. THF was removed under reduced pressure and the remaining NP suspension concentrated down to a TIPS-Pn concentration of ∼100 ppm. Lastly, the samples were filtered through a 0.2 µm hydrophilic syringe filter (Sartorius Minisart NML). The approximate final concentration of each component in the NPs is given in Table 2.1.

Various properties of these NPs are presented in Appendix 2.5, including a calculation of the "average intermolecular TIPS-Pn separation" within the NPs. The average intermolecular TIPS-Pn separation increases with increasing proportion of PMMA (refer to Table 2.8). This separation ranges from 0.99 nm for the 1:0 TIPS-Pn:PMMA NP sample, to 2.15 nm for the 1:10 sample.

Table 2.1: Quantities used to prepare different TIPS-Pn:PMMA mass ratio NPs.

Sample (TIPS-Pn:PMMA mass ratio)	**Component**	**Volume used (mL)**	**Concentration in mixed stock (ppm)**	**Concentration of NPs (ppm)**
1:0	TIPS-Pn	0.75	20	100
	PMMA	-	-	-
	CO-520	0.40	20	100
	THF	13.85	-	-
1:1	TIPS-Pn	0.75	20	100
	PMMA	0.75	20	100
	CO-520	0.80	40	200
	THF	12.70	-	-
1:3	TIPS-Pn	0.75	20	100
	PMMA	2.25	60	300
	CO-520	1.60	80	400
	THF	10.40	-	-
1:5	TIPS-Pn	0.75	20	100
	PMMA	3.75	100	500
	CO-520	2.40	120	600
	THF	8.10	-	-
1:7	TIPS-Pn	0.75	20	100
	PMMA	5.25	140	700
	CO-520	3.20	160	800
	THF	5.80	-	-
1:10	TIPS-Pn	0.75	20	100
	PMMA	7.50	200	1000
	CO-520	4.40	220	1100
	THF	2.35	-	-
1:100	150 ppm TIPS-Pn	0.60	6	30
	1500 ppm PMMA	6.00	600	3000
	1500 ppm CO-520	6.00	600	3000
	THF	2.40	-	-

2.2 Steady-state Optical Measurements

Steady-state absorption spectra of our samples in a 2 mm path length quartz cuvette (Starna Cells 21-Q) were obtained using a Cary Varian 1E ultraviolet-visible (UV-Vis) spectrometer. Steady-state fluorescence spectra of our samples (with absorbances of less than 0.1) in a 1 cm path length cuvette (Starna Cells 3-Q) were obtained after excitation of 590 nm by a Perkin Elmer LS 55 fluorescence spectrophotometer, with excitation and emission bandwidths of 5 nm and 15 nm, respectively. Due to the low fluorescence signal, an emission bandwidth of 15 nm was chosen and no cut-off filter was used.

2.3 Spectroscopy

This section outlines the ultrafast spectroscopic techniques used to monitor the excited states of the TIPS-Pn/PMMA NPs. The methods described in Sections 2.3.1,

2.3.2 and 2.3.3 all use laser pulses sourced from the output of a regenerative amplifier. 800 nm pulses with a repetition rate of 80 MHz were produced from a mode-locked Ti:Sapphire oscillator (Spectra-Physics, Tsunami) pumped by a 8 W 532 nm continuous-wave Nd:YVO_4 laser (Spectra-Physics, Millenia Prime). These pulses are used as seed pulses by the regenerative amplifier (Spectra-Physics, Spitfire Pro XP 100F) to generate 100 fs pulses centred at 800 nm with a 1 kHz repetition rate.

2.3.1 Fluorescence Upconversion

Fluorescence upconversion (UC) is a method used to obtain time-resolved fluorescence data, offering a high time resolution at the expense of some sensitivity. We use fluorescence UC to obtain femtosecond time-resolved fluorescence measurements of our TIPS-Pn/PMMA NPs. This method has been described previously,[34,55,69] and is illustrated in Figure 2.2. There are two laser pulses, labelled "pump" and "gate". The pump beam is directed onto the sample to generate the photoexcited state. The sample's fluorescence is focused onto a 0.4 mm β-barium borate (BBO) crystal. The gate beam is instead directly focused onto the same BBO crystal. The BBO crystal's non-linear properties converts the photons of these two beams into photons of a higher energy through sum frequency generation (SFG). In this way, the fluorescence is "upconverted" to a higher frequency ($f_{\text{upconverted}} = f_{\text{fluorescence}} + f_{\text{gate}}$), and it is this upconverted frequency that is measured by the detector. The upconverted fluorescence wavelength to be detected is selected by rotation of the BBO crystal to obtain the required phase matching condition. The frequency is only upconverted when the sample's fluorescence and the gate pulse overlap in time. Time resolution is built up by changing the delay time of the gate with respect to the initial excitation of the sample. This ensures that the time resolution is limited by the duration of the laser pulses, rather than the much slower speed of the detector.

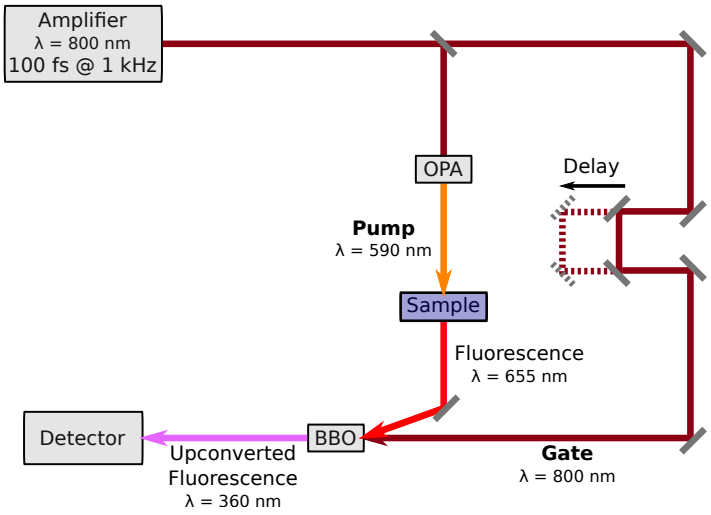

Figure 2.2: A schematic of the fluorescence UC spectrometer used to collect time-resolved fluorescence data of TIPS-Pn.

A fluorescence spectrometer (Ultrafast Systems, Halcyone) was used to collect time-resolved fluorescence. This set-up has been described previously,[57,98] and is schematically illustrated in Figure 2.2. An optical parametric amplifier (OPA) (Light Conversion, TOPAS-C), using the second harmonic of the signal at 1180 nm, generated

the 590 nm pump pulses (∼0.10 µJ per pulse) to excite the samples. The polarisation of the pump was rotated to magic angle (54.7°) relative to the gate beam to negate anisotropic effects. This beam was focused onto the samples with a full width half maximum (FWHM) spot size of ∼0.17 mm, and the fluorescence was focused onto the 0.4 mm BBO crystal. The gate beam was generated by splitting off a small fraction of the raw 800 nm amplifier output and was focused onto the same BBO crystal. A computer controlled delay line was used to delay the arrival of the gate relative to the pump. To detect the fluorescence at 655 nm, the resulting intensity of the upconverted fluorescence (360 nm) was detected using a photomultiplier tube attached to a monochromator.

The samples, of ∼100 ppm TIPS-Pn concentration, were contained in a 0.2 cm quartz cuvette (Starna Cells 21-Q) and stirred continuously throughout the experiment. Samples were found to degrade by less than 2% over the entire experiment, which consisted of an average of 10 scans. All experiments were performed at 21°C.

2.3.2 Time-correlated Single Photon Counting

Time-correlated single photon counting (TCSPC) is a method with a high sensitivity due to the detection of the raw fluorescence. Although the time resolution is limited to ∼500 ps by the speed of the detector, it allows monitoring of the fluorescence over longer timescales. We use TCSPC here to obtain time-resolved fluorescence data of our samples up to 80 ns after initial excitation of the sample. The TCSPC set-up is equivalent to that of the fluorescence UC (refer to Section 2.3.1 and Figure 2.2), but without the gate beam and with the detector instead set to detect the raw fluorescence at 655 nm.

2.3.3 Transient Absorption Spectroscopy

Transient absorption (TA) spectroscopy is a technique used to study photo-physical processes and their kinetics. The pump–probe TA method allows monitoring the change in absorbance (ΔA) over time, and gives insight into the formation, interaction and decay of various excited-state species. This method has been described and used previously,[33,34,42,43,45,50,52–55,58,60,62–64,67,69,70,73,76,79–82,85,99–103] and is illustrated in Figure 2.3. This technique involves two laser pulses. The first "pump" pulse is used to excite the sample and then a "probe" pulse measures the absorption of the excited sample some time after excitation. When the probe is a broadband "white light" supercontinuum, the absorption can be measured across a wide spectral range with a single laser shot. Time-dependent data can be obtained by delaying the probe pulse by some time t relative to the pump pulse. The time resolution is limited only by the pulse duration, typically between 30 fs to 1 ps. The change in absorbance relative to the steady-state absorbance is therefore obtained as a function of wavelength, λ, and time, t,

$$\Delta A(\lambda, t) = A(\lambda, t)_{\text{pump}} - A(\lambda, t)_{\text{no pump}}. \tag{2.1}$$

In the absence of a pump pulse, the probe just detects the steady-state absorption spectrum. The change in absorbance is therefore a reflection of the difference between the absorbance of excited-state species and the steady-state,

$$\Delta A(\lambda, t) = A(\lambda, t)_{\text{excited state}} - A(\lambda, t)_{\text{steady-state}}. \tag{2.2}$$

The pump pulse is normally chosen to match the S_0 to S_1 absorption to produce a sample population in the S_1 state. A chopper is used to block every second pump pulse, so the absorption can be detected with the pump, $A(\lambda)_{\text{pump}}$, and without the pump, $A(\lambda)_{\text{no pump}}$. Continuous collection of pump-on and pump-off measurements reduces noise due to laser power fluctuations.

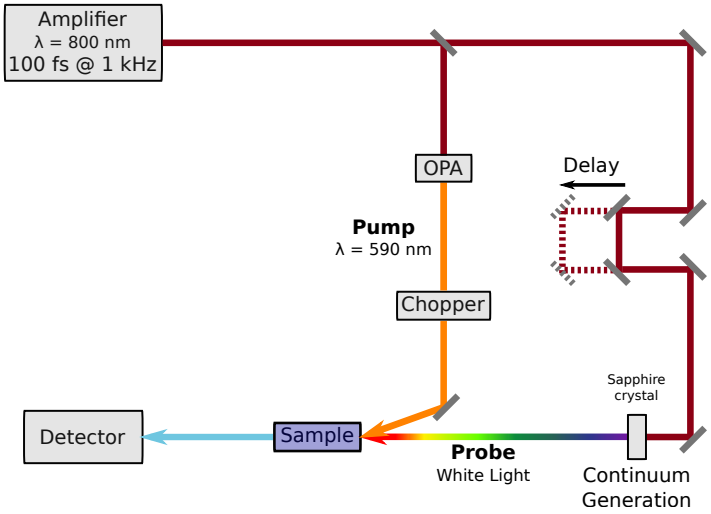

Figure 2.3: A schematic of the TA spectrometer used to collect TA data of TIPS-Pn.

The probe can measure various optical processes occurring in a chromophore (refer to Figure 2.4). As the pump excitation causes a reduction of the ground state, S_0, the normal ground-state absorption is reduced. This manifests as a negative ΔA, over similar wavelengths as the steady-state absorption spectrum, termed ground-state bleach (GSB). A negative ΔA signal can also occur when the sample emits light, for

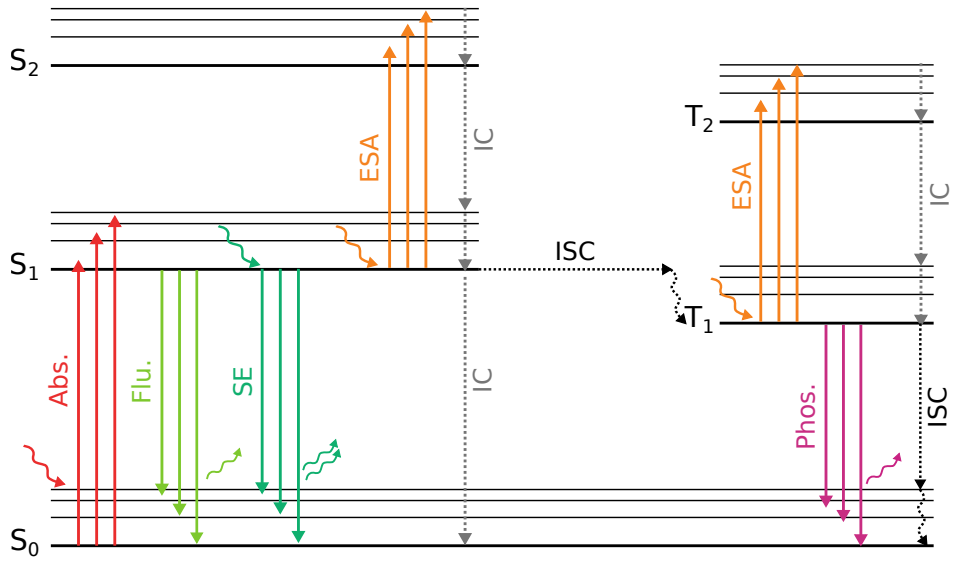

Figure 2.4: Some optical processes a chromophore can undergo. These include absorption (Abs.) from the ground state, radiative decay via fluorescence (Flu.) from the singlet state, stimulated emission (SE) from the singlet state, excited-state absorption (ESA) from both the singlet and triplet states, and radiative decay via phosphorescence (Phos.) from the triplet state. Inter-system crossing (ISC) can occur from the singlet to triplet manifold and various non-radiative internal conversion (IC) decay process can also occur.

example from stimulated emission (SE) caused by a photon from the probe which has an energy equal to the S_1 to S_0 transition. This negative SE emission signal occurs across similar wavelengths as the steady-state fluorescence spectrum. Positive ΔA signals imply absorption of an additional probe photon by excited-state species and is called excited-state absorption (ESA). This absorption results in excited-state species in higher-lying energy state (e.g. $S_1 \rightarrow S_n$ or $T_1 \rightarrow T_n$).

A TA spectrometer (Ultrafast Systems, Helios) was used to collect TA data. This set-up has been described previously,[57,98,104] and is schematically illustrated in Figure 2.3. An OPA (Light Conversion, TOPAS-C), using the second harmonic of the signal at 1180 nm, generated the 590 nm pump pulses (∼0.50 µJ per pulse) to excite the samples. An optical chopper mechanically modulated the pump pulses at a frequency of 500 Hz, thus producing a pump pulse only every two probe pulses, to obtain ΔA as per Equation 2.1. The polarisation of the pump was rotated to magic angle (54.7°) relative to the gate beam to negate anisotropic effects. This pump beam was focused onto the samples with a FWHM spot size of ∼0.83 mm and ∼0.82 mm for the visible and near-infrared (NIR) experiments, respectively. The probe was a white light continuum obtained by focusing a small portion of the 800 nm amplifier output onto a 3.2 and 12.7 mm sapphire crystal for the visible and NIR range, respectively. A computer controlled delay line was used to delay the arrival of the probe relative to the pump. The probe was split into signal and reference beams, with the signal beam focused onto the samples with a FWHM spot size of ∼0.28 mm and ∼0.22 mm for the visible and NIR experiments, respectively. The linear detectors used were CMOS based in the visible region (Ultrafast Systems, CAM-VIS-2) and INGaAs for the NIR region.

The samples, of ∼100 ppm TIPS-Pn concentration, were contained in a 0.2 cm quartz cuvette (Starna Cells 21-Q) and stirred continuously throughout the experiment. Samples were found to degrade by less than 2% over the entire experiment, which consisted of an average of 10 scans. All experiments were performed at 21°C. All spectra were corrected for the probe's dispersion by adjusting the time-zero for the correct arrival time of the probe at each wavelength, as determined by the pump–probe coherent artefact response from the solvent (water).

2.3.4 Magic-angle Conditions

For intensity decay measurements, magic-angle conditions are important. The intensity should be measured such that all of the arbitrarily orientated chromophores have equal probability of contributing to the total intensity, regardless of their orientation. The intensity should therefore be measured proportional to the total intensity which, for z-axis symmetry emission, is given by $I_T = I_\parallel + 2I_\perp$. This is achieved by orientating the probe to vertical and the pump to 54.7°, termed "magic angle", from the vertical by use of polarisers and half-wave plates. This angle is equal to $\arctan(\sqrt{2})$ and represents the angle between the diagonal of a cube and any of the adjacent sides. As $\cos^2(54.7°) = 0.333$ and $\sin^2(54.7°) = 0.667$, $I_\perp$ is selected twofold over $I_\parallel$, forming the correct sum for I_T. Measuring the intensity proportional to I_T, means anisotropic effects (i.e. degree of polarisation of the sample) are negligible. Nevertheless, sometimes the anisotropic behaviour of a system may be of interest, for example, when investigating the migration rate of excited-state species.

2.3.5 Polarisation Anisotropy Measurements

A detailed explanation of polarisation anisotropy, and the processes contributing to its decrease, are discussed in Section 1.5. Time-resolved polarisation anisotropy measurements are a useful tool in measuring the depolarisation of a sample. A sample with randomly oriented chromophores is excited by vertically polarised light. When the emission polariser is orientated parallel (perpendicular) to the excitation, the measured intensity is called $I_{\parallel}$ ($I_{\perp}$). These intensities are then used to calculate the time-resolved fluorescence anisotropy, defined as[91,104,105]

$$r(t) = \frac{I_{\parallel}(t) - I_{\perp}(t)}{I_{\parallel}(t) + 2I_{\perp}(t)}. \tag{2.3}$$

TA anisotropy as a function of time, t, and wavelength, λ, is defined as[104,106–108]

$$r(t,\lambda) = \frac{\Delta A_{\parallel}(t,\lambda) - \Delta A_{\perp}(t,\lambda)}{\Delta A_{\parallel}(t,\lambda) + 2\Delta A_{\perp}(t,\lambda)}, \tag{2.4}$$

where $\Delta A_{\parallel}(t,\lambda)$ and $\Delta A_{\perp}(t,\lambda)$ are the change in absorbances parallel and perpendicular to the excitation polarisation, respectively.

We note that the anisotropy is also often defined with the inclusion of a "G factor". The G factor is defined as the ratio of the sensitivities of the detection system from vertically, S_V, and horizontally, S_H, polarised light: $G = \frac{S_V}{S_H}$,[91] and is needed for the anisotropy calculation in order to correct for any bias in measuring the two different polarisation intensities. In our measurements, the excitation polarisation is rotated from vertical to horizontal relative to the gate/probe beam and so the detector is set to always detect vertically polarised light. Therefore, the detector itself does not cause a change in sensitivity between the two polarisation measurements. However, the rotation of the excitation polarisation from vertical to horizontal caused slight changes in power incident on the sample. As such, the system had a greater sensitivity to detecting the horizontally polarised light. The power difference incident on the sample was measured and the perpendicular intensity scans were multiplied by 0.954 and 0.975 for fluorescence UC and TA, respectively, before the anisotropy was calculated using Equations 2.3 and 2.4, respectively.

The anisotropy values for a sample with a random distribution of chromophores range from -0.2 to 0.4. These limiting anisotropy values are discussed in Section 1.5.3.

The apparatus used for fluorescence and TA anisotropy experiments are those described in Sections 2.3.1 and 2.3.3, respectively. A minimum of 10 consecutive parallel and perpendicular intensity measurements were obtained by rotation of the pump polarisation using a half-wave plate. Time-resolved anisotropy was obtained at 655 nm for fluorescence and for all wavelengths in the visible range (400–800 nm) and NIR range (900–1400 nm) for TA.

2.4 Computational Methods

The Monte Carlo (MC) simulation presented in this thesis was based on a previous simulation of exciton migration in the polymer poly(3-hexylthiophene) (P3HT) by Tapping et al.[105] The simulation was then modified by Jessica M. de la Perrelle, a Summer Research Student under Assoc. Prof. Tak W. Kee, for the TIPS-Pn/PMMA system studied here.

2.4.1 Simulation Box

The NP systems consisted of a number of TIPS-Pn molecules, corresponding to the required TIPS-Pn:PMMA mass ratio, in a cubic simulation box with periodic boundary conditions (PBCs) enforced. The average number of TIPS-Pn molecules within a certain volume, V_{box}, is determined by

$$N_{\text{TIPS-Pn}} = \frac{V_{\text{box}}}{V_{V_{\text{TIPS-Pn}}}}, \tag{2.5}$$

where $V_{V_{\text{TIPS-Pn}}}$ is the average Voronoi volume of a TIPS-Pn molecule (defined and derived in Appendix 2.5.1), and was dependent on the mass ratio of TIPS-Pn:PMMA=1:α

$$V_{V_{\text{TIPS-Pn}}} = \frac{(\rho_{\text{PMMA}} + \alpha\rho_{\text{TIPS-Pn}})MW_{\text{TIPS-Pn}}}{\rho_{\text{TIPS-Pn}}\rho_{\text{PMMA}}N_A}. \tag{2.6}$$

A 20 nm length cubic box was used for this molecular dynamics (MD) simulation. The number of TIPS-Pn molecules to be placed into the MD simulation box for each of the TIPS-Pn:PMMA mass ratio NPs was calculated using Equations 2.5 and 2.6, and given in Table 2.2.

Table 2.2: Average Voronoi volume of TIPS-Pn and number of TIPS-Pn molecules in the MD simulation box for each of the TIPS-Pn:PMMA mass ratio NPs.

Sample (TIPS-Pn:PMMA mass ratio (1 : α))	**Average Voronoi volume of TIPS-Pn (nm^3), $V_{V_{\text{TIPS-Pn}}}$**	**Number of TIPS-Pn in the 20 nm MD simulation box, $N_{\text{TIPS-Pn}}$**
1:0	0.96	8322
1:1	1.85	4314
1:3	3.64	2197
1:5	5.43	1474
1:7	7.21	1109
1:10	9.89	809

The MC simulation was run with randomly distributed TIPS-Pn molecules and systems representing different amounts of clustered TIPS-Pn molecules. A MD simulation was run to obtain a representation of these different types of clustered systems.

2.4.1.1 Molecular Dynamics

MD is a computational method to study the physical movements of particles (generally atoms or molecules) in a system. Newton's equations of motion are used to simulate the classical interactions between particles, over timescales up to 1 µs.

Newton's equations of motion state that the force on a particle is equal to its mass times its acceleration, where the acceleration is given by the second derivative of the particle's position. Mathematically, for N particles this is represented as

$$\mathbf{F}_i(\mathbf{r}^N) = m_i\frac{\mathrm{d}^2\mathbf{r}_i}{\mathrm{d}t^2} = -\nabla_i\mathbf{U}(\mathbf{r}^N), \tag{2.7}$$

where $\mathbf{F}_i$ is the force vector on particle i, $\mathbf{r}^N$ is the position of the particles, m_i is the mass of particle located at $\mathbf{r}_i$, and $\mathbf{U}$ is the function called the force field.

The force field describes the potential energy surface for all interacting particles, and is generally a sum of bonded and non-bonded particle interactions

$$U = U_{\text{VDW}} + U_{\text{ES}} + U_{\text{bond}} + U_{\text{angle}} + U_{\text{dihedral}}, \tag{2.8}$$

where U_{VDW} and U_{ES} are the non-bonded van der Waals (VDW) and electrostatic (ES) interactions. U_{bond}, U_{angle} and U_{dihedral} are the bond stretch, bond angle and dihedral angle potentials, respectively.

The positions of particles can be found by numerical integration of Equation 2.7, with the period of integration (termed "timestep") chosen to be faster than the fastest phenomena within the system.

2.4.1.2 Coarse-grained Method

Often, MD uses fully atomistic models in which each atom in a molecule is mapped to a particle. A coarse grained model is one which simplifies the system by reducing the number of particles while retaining large-scale physical properties and behaviour. Coarse-graining also eliminates the most rapid degrees of freedom, such as C–H bonds, allowing a longer integration timestep. Fewer particles results in less particle interactions needing to be calculated, and thus the efficiency of the MD simulation can be enhanced because larger systems or longer simulation times can be achieved for the same computing resources. An example of an atomistic to coarse-grained mapping is shown in Figure 2.5.

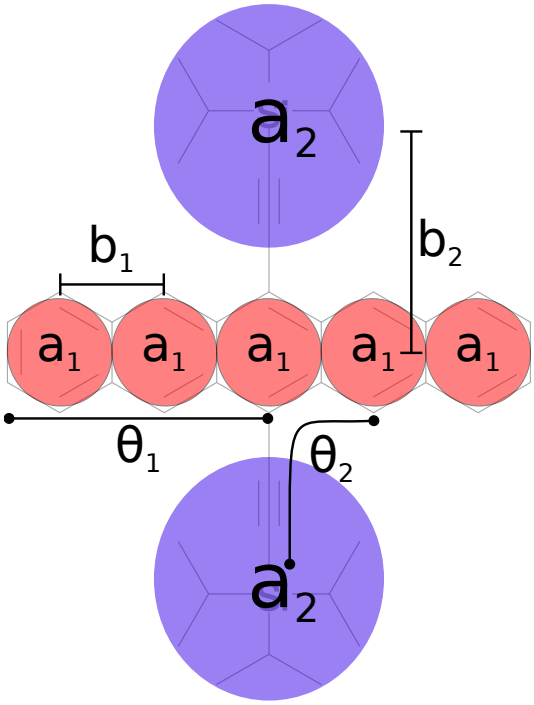

Figure 2.5: The atomistic to coarse-grained mapping of TIPS-Pn for the MD simulation. Parameters for the non-bonded, the harmonic bond length and the bond angle potentials are given in Tables 2.3, 2.4 and 2.5, respectively.

2.4.1.3 Obtaining TIPS-Pn Input Geometries from Molecular Dynamics Simulations

We require input positions and transition dipole moments of TIPS-Pn molecules for our MC simulation. TIPS-Pn molecules were assumed to be randomly distributed in the NP systems by Stuart et al.[57] However, it is possible that during the NP formation TIPS-Pn-TIPS-Pn or PMMA-PMMA interactions are favoured, driving some degree of phase separation and so TIPS-Pn molecules could form a more "clustered" distribution within the NPs.

We use MD to crudely simulate clustering of TIPS-Pn molecules during the formation of the NPs. These simulations were performed with the MD simulation package LAMMPS. Rather than a fully atomistic model of TIPS-Pn molecules, we use a coarse-grained model in which a TIPS-Pn molecule is represented by five spherical beads corresponding to the centre of mass of the benzene rings of pentacene (Pn) and two spheres for the triisopropylsilylethnyl (TIPS) groups. The transition dipole moments are defined as the unit vector between the centre benzene ring to one of the TIPS groups. This atomistic to coarse-grained mapping is illustrated in Figure 2.5.

The bond lengths and angles are represented by a harmonic potential, with the equilibrium bond length/angle and corresponding force constant for the bonded/angle potentials given in Tables 2.4 and 2.5. Intramolecular interactions were turned off so Lennard-Jones (LJ) interactions were only calculated between molecules.

The coarse-grained system representing a pure TIPS-Pn NP was run under constant temperature and pressure conditions (the canonical NPT ensemble). The homonuclear LJ diameter, σ_{ii}, and homonuclear LJ interaction strength, ε_{ii}, were optimised to achieve a constant volume corresponding to the density of pure TIPS-Pn. The resulting parameters are given in Table 2.3

Molecules are initially placed at random inside a 20 nm cubic box. The system was simulated at 298 K and 1 atm with PBC enforced to simulate the larger NP system. Langevin dynamics were used in the MD simulation to model an implicit solvent, with the dampening factor set to 1 fs. It roughly represents the PMMA matrix in the NP system.

Overlapping atoms from the randomly input TIPS-Pn molecules were removed by performing an energy minimisation, and thus used as a more realistic representation of "randomly distributed" TIPS-Pn molecules for the MC simulation.

A series of soft potentials were used to equilibrate the system. A LJ force field (parameters given in Table 2.3) was then applied to the TIPS-Pn molecules to simulate their clustering during NP formation. The MD simulation does not aim to be a true representation of the dynamics of TIPS-Pn molecules during NP formation. Instead, the aim was to obtain representations of different amounts of "clustered" TIPS-Pn molecules in the final NP systems. Consequently, the positions and transition dipole moments were extracted from the MD simulation at various timesteps (corresponding to different degrees of clustering) and used as input for the MC simulation.

Table 2.3: Parameters used in the non-bonded potential, $U_{\text{non-bonded}}(r_{ij}) = 4\varepsilon_{ij}[(\sigma_{ij}/r_{ij})^{12} - (\sigma_{ij}/r_{ij})^{6}]$, where σ_{ii} is the homonuclear LJ diameter and ε_{ii} is the homonuclear LJ interaction strength.

	m ($\mathbf{g\,mol^{-1}}$)	$\boldsymbol{\sigma_{ii}}$ (**Å**)	$\boldsymbol{\varepsilon_{ii}}$ ($\mathbf{kcal\,mol^{-1}}$)
$\mathbf{a_1}$	55.27	1.5	3.3
$\mathbf{a_2}$	181.37	1.5	3.9

Table 2.4: Parameters used in the harmonic bond length potential, $U_{\text{bond}}(l) = k_l \frac{(l-l_0)^2}{2}$, where l_0 is the equilibrium bond distance and k_l is the force constant for the bonded potential.

	$\boldsymbol{l_0}$ (**Å**)	$\boldsymbol{k_l}$ ($\mathbf{kcal\,mol^{-1}\,Å^{-2}}$)
$\mathbf{b_1}$	2.41	1000
$\mathbf{b_2}$	4.8	100

Table 2.5: Parameters used in the harmonic bond angle potential, $U_{\text{angle}}(\theta) = k_\theta \frac{(\theta-\theta_0)^2}{2}$, where θ_0 is the equilibrium bond angle and k_θ is the force constant for the angle potential.

	$\boldsymbol{\theta_0}$ (°)	$\boldsymbol{k_\theta}$ ($\mathbf{kcal\,mol^{-1}\,rad^{-2}}$)
θ_1	180	1000
θ_2	90	1000

2.4.2 Rate Constants for Singlet Migration, Singlet Fission and Singlet Decay

Singlet migration occurs through a Förster resonance energy transfer (FRET) process in our model. The singlet migration rate constant used in this MC simulation, k_{DA}, is given in Section 1.4.

The hopping rate, k_{DA}, is dependent on the transition dipole coupling term, J_{DA}, given in Equation 1.4. This is dependent on the relative permittivity, ε_{r}, of the 1:α TIPS-Pn:PMMA NP (α ranges from 0 to 10), which is approximated by the weighted average of the permittivities of TIPS-Pn and PMMA,

$$\varepsilon_{\text{r}} = \varepsilon_{\text{TIPS-Pn}}\left(\frac{1}{1+\alpha}\right) + \varepsilon_{\text{PMMA}}\left(\frac{\alpha}{1+\alpha}\right), \tag{2.9}$$

where $\varepsilon_{\text{TIPS-Pn}}$ and $\varepsilon_{\text{PMMA}}$ are the relative permittivity of TIPS-Pn and PMMA, respectively. Approximate values for these parameters were taken from literature,[109–111] and are given in Table 2.6.

A simple model for singlet fission (SF) is employed in our MC simulation, as the microscopic details of SF are not yet fully understood.[112] We assume SF occurs with a rate k_{SF} if a singlet molecule has a ground-state molecule within a distance of r_{SF}. Mathematically, we describe the rate of SF by

$$k_{\text{SF}}^{D,A} = k_{\text{SF}}\Theta(r_{\text{SF}} - r^{D,A}), \tag{2.10}$$

where D and A denote the "donor" singlet molecule and "acceptor" ground-state molecule, respectively. $r^{D,A}$ is the distance between those two molecules and Θ is the Heaviside step function. The "SF radius", r_{SF}, is defined as the maximum distance

Table 2.6: MC simulation parameters.

Parameter	Symbol	Value
Density of TIPS-Pn	$\rho_{\text{TIPS-Pn}}$	$1.104\,\text{g}\,\text{cm}^{-3}$
Density of PMMA	ρ_{PMMA}	$1.188\,\text{g}\,\text{cm}^{-3}$
Relativity permittivity of TIPS-Pn	$\varepsilon_{\text{TIPS-Pn}}$	3.0
Relativity permittivity of PMMA	$\varepsilon_{\text{PMMA}}$	2.25

between a donor and acceptor in order for SF to occur. In this model, $k_{\text{SF}}^{D,A} = k_{\text{SF}}$ if $r^{D,A} \leq r_{\text{SF}}$ and $k_{\text{SF}}^{D,A} = 0$ if $r^{D,A} > r_{\text{SF}}$.

The singlet decay rate constant, k_{d}, is taken from the intrinsic lifetime of singlets from TCSPC data of dilute TIPS-Pn in THF.[57] Therefore,

$$k_{\text{d}} = \frac{1}{12}\ \text{ns}^{-1}. \tag{2.11}$$

The event which occurs in the MC simulation (hopping, SF or decay), is chosen by considering the probability of each event happening in a random time interval, Δt. If k is the probability of a transition occurring per unit time, the probability of the transition *not* happening in a time interval, Δt, is given from Poisson statistics as $P(t) = \exp(-k\Delta t)$. We can therefore define a (random) time interval, Δt, for a transition to occur via $\exp(-k\Delta t) = x$ where x is a uniform deviate, $0 \leq x \leq 1$.[113]

Therefore,

$$\Delta t = -\frac{\ln(x)}{k}. \tag{2.12}$$

A set of time intervals for hopping, SF or decay is determined by Equation 2.12 where $k = \{k_{\text{DA}}, k_{\text{SF}}, k_{\text{d}}\}$ is the set of all rate constants for the donor, and x is a random variate over [0,1] chosen for each k.

2.4.3 Generation and Parameterisation of Steady-state Absorption and Emission Spectra

The singlet migration rate, k_{DA} is dependent on the spectral overlap, X_{DA} between the donor and acceptor. This spectral overlap is calculated by integrating over the product of the emission spectrum of the donor and absorption spectrum of the acceptor.

In the MC simulation, the steady-state absorption and emission spectra of the chromophores were simulated by a Franck-Condon progression, with an intensity given by

$$I(E) = \sum_{\upsilon=0}^{\upsilon=N-1} \frac{E^{-s} s^{\upsilon}}{\upsilon!} \frac{\gamma}{\pi(\upsilon\hbar\omega - E_0)^2 + \gamma^2)}, \tag{2.13}$$

where e is the energy of the chromophore, and the other parameters are defined in Table 2.7. Chromophores are generated with energies from a normal distribution with a mean E_0 and standard deviation E_α.

The simulated steady-state absorption spectrum was generated by summing over the absorption spectra of all chromophores. The simulated steady-state fluorescence spectrum was generated by summing over only those chromophores which decay during the MC simulation. Both spectra are also scaled by an oscillator strength factor, μ_0^2.

The Stokes shift in the fluorescence spectra is replicated since a higher proportion of lower energy chromophores fluoresce, and so the Stokes shift is dependent on E_α.

Literature values and optimisation routines were used to select the parameters in Equation 2.13, such that the simulated 1:10 TIPS-Pn:PMMA NP spectrum matched the experimental 1:10 spectrum.

μ_0 was obtained from literature,[114] E_0 was set to match the 0–0 transition, E_α was set to produce the most accurate Stokes shift, $\hbar\omega$ was chosen to obtain the best spacing between the peaks, s was chosen to match the peak heights of the vibronic transitions. γ was then optimised so the simulated spectra matched the experimental spectra. The best fit parameters are summarised in Table 2.7, and the corresponding steady-state simulated absorption and emission spectra are given along with the experimental spectra in Section 6.2.

Table 2.7: MC simulation parameters for the steady-state absorption and fluorescence spectra.

Parameter	**Symbol**	**Value**
Number of vibronic levels (abs)	N_{abs}	4
Number of vibronic levels (flu)	N_{flu}	2
Magnitude of transition dipole moment	μ_0	1.171×10^{-29} Cm
0–0 Transition energy	E_0	1.928 eV
Standard deviation of energy	E_α	0.015 eV
Energy of harmonic vibrational frequency	$\hbar\omega$	0.168 eV
Vibronic linewidth	γ	0.06 eV
Huang-Rhys parameter (abs)	s_{abs}	0.45
Huang-Rhys parameter (flu)	s_{flu}	0.1

2.4.4 Monte Carlo Simulation Structure

The coordinates and transition dipole moments of the TIPS-Pn molecules for a given mass ratio were extracted from the MD simulation (as described in Section 2.4.1.3) and used as the input for the MC simulation. The chromophores were given a normal distribution of energies about the 0–0 vibronic transition energy, E_0, with a standard deviation of E_α.

For each relevant donor/acceptor pair, Equation 1.3, is calculated. This requires calculation of Equation 1.4 and the spectral overlap X_{DA}. k_{DA} is only calculated when the donor energy was greater than the acceptor energy, and the distance between the pair was less than 10 nm. The SF rate, $k_{\text{SF}}^{D,A}$, is also determined for each donor/acceptor pair (i.e. either 0 if $r^{D,A} > r_{\text{SF}}$ or k_{SF} if $r^{D,A} < r_{\text{SF}}$). The singlet decay rate is kept constant at $k_{\text{d}} = \frac{1}{12}$ ns^{-1}. Once these relevant rate constants for each donor/acceptor pair are determined, Δt for each can be calculated using Equation 2.12.

A MC process is then used to simulate the system, which occurs through repetition of a series of steps:

1. A chromophore is chosen at random to be excited to its singlet state.

2. The singlet can then hop to a new chromophore, undergo SF or decay to the ground state. The process chosen is the one with the smallest Δt.

3. If a hop is chosen, the total time is incremented by that Δt. The acceptor is then excited and step 2) is repeated for the new chromophore.

4. If singlet decay or SF is chosen, energy and time fluorescence and anisotropy histograms are populated and a new chromophore is excited. Steps 1) – 4) are repeated from 1×10^5 excitations.

The SF rate constant, k_{SF}, and the SF radius, r_{SF}, are input parameters of the MC simulation. To find the best fit to the experimental fluorescence magic-angle and anisotropy data, the MC simulation was run for numerous values of k_{SF} and r_{SF} for systems with randomly and clustered TIPS-Pn distributions.

2.4.5 Histogram Binning

A fluorescence event may only be observed upon singlet decay. Consequently, the fluorescence histogram should be populated by accordingly binning the emission spectrum of the chromophores on which singlet decay occurred on. The anisotropy histogram should also be binned upon a singlet decay. The numerator of the anisotropy is given by $\frac{1}{2}I_0(3\cos(\theta)^2 - 1)$, where θ is the angle between the transition dipole moments of the initially excited chromophore and the chromophore decaying, and I_0 is the fluorescence intensity of the decaying chromophore. The denominator of the anisotropy is the total fluorescence intensity.

However, the singlet decay rate is $\frac{1}{12}$ ns^{-1}, meaning decay events are infrequent. Consequently, binning only at decay events would require an enormous amount of excitations to obtain statistically valid results. To reduce the amount of necessary excitations, and hence computational time, we also populate all previous histogram bins before singlet decay or SF events, because the singlet could fluoresce any time up until this event. Building up the histogram in this way over a large number of excitations will eventually produce the exponential shape of the fluorescence decay. The previous fluorescence histograms bins are populated using the emission spectrum of the chromophore the singlet was on at the time. The anisotropy histogram is binned in a similar way, with θ being the transition dipole moments of the initially excited chromophore and the chromophore the singlet was on at the time, and I_0 is the fluorescence intensity of that chromophore. The histogram bin corresponding to a decay or SF event is only populated with a fraction of the corresponding fluorescence or anisotropy.

The anisotropy is scaled by 0.4 to account for the photoselection phenomenon observed in the experimental results. By selection of a wavelength from the two-dimensional (2D) simulated fluorescence and anisotropy histograms, fluorescence and anisotropy kinetics can be generated to compare to the experimental data.

2.5 Appendices: Calculations

The mass ratio of TIPS-Pn and PMMA and their respective densities can be used to calculate various properties of our NPs.

We define:
$m_{\text{TIPS-Pn}}$ and m_{PMMA} as the average mass of TIPS-Pn and PMMA, respectively, in a NP.
$m_{\text{NP}} = m_{\text{TIPS-Pn}} + m_{\text{PMMA}}$ as the average total mass of a NP.
$V_{\text{TIPS-Pn}}$ and V_{PMMA} as the average volume of TIPS-Pn and PMMA, respectively, in a NP.
$V_{\text{NP}} = V_{\text{TIPS-Pn}} + V_{\text{PMMA}}$ as the average total volume of a NP.
$\rho_{\text{TIPS-Pn}}$ and ρ_{PMMA} as the density of TIPS-Pn and PMMA, respectively.
ρ_{NP} as the average total density of a NP.
$N_{\text{TIPS-Pn}}$ as the average number of TIPS-Pn molecules in a NP.
$c_{\text{TIPS-Pn}}$ as the average concentration of TIPS-Pn in a NP.
$n_{\text{TIPS-Pn}}$ as the average number of moles of TIPS-Pn in a NP.
$MW_{\text{TIPS-Pn}}$ as the molecular weight of TIPS-Pn.
N_A as Avogadro's number.

For a NP sample with a TIPS-Pn:PMMA mass ratio of 1:α,

$$m_{\text{PMMA}} = \alpha m_{\text{TIPS-Pn}}. \tag{2.14}$$

2.5.1 Average Voronoi Volume of TIPS-Pn in a NP

To define some average distance between TIPS-Pn molecules, we first define a volume around each TIPS-Pn such that no other particles are in this volume. This is illustrated as a Voronoi diagram in Figure 2.6. We envision TIPS-Pn as points, and define regions of volume around each TIPS-Pn for which any point within this volume is closest to that specific TIPS-Pn molecule.

The average Voronoi volume for a TIPS-Pn, $V_{V_{\text{TIPS-Pn}}}$, is equal to the sum of all Voronoi volumes (i.e. the total volume of the NP, V_{NP}) divided by the number of TIPS-Pn molecules in the NP, $N_{\text{TIPS-Pn}}$.

$$\begin{aligned} V_{V_{\text{TIPS-Pn}}} &= \frac{V_{\text{NP}}}{N_{\text{TIPS-Pn}}} \\ &= \frac{\frac{m_{\text{NP}}}{\rho_{\text{NP}}}}{\frac{m_{\text{TIPS-Pn}}}{MW_{\text{TIPS-Pn}}} N_A} \\ &= \frac{m_{\text{NP}} MW_{\text{TIPS-Pn}}}{\rho_{\text{NP}} m_{\text{TIPS-Pn}} N_A} \end{aligned} \tag{2.15}$$

Making use of Equation 2.14,

$$\begin{aligned} V_{V_{\text{TIPS-Pn}}} &= \frac{(1+\alpha) m_{\text{TIPS-Pn}} MW_{\text{TIPS-Pn}}}{\rho_{\text{NP}} m_{\text{TIPS-Pn}} N_A} \\ &= \frac{(1+\alpha) MW_{\text{TIPS-Pn}}}{\rho_{\text{NP}} N_A}. \end{aligned} \tag{2.16}$$

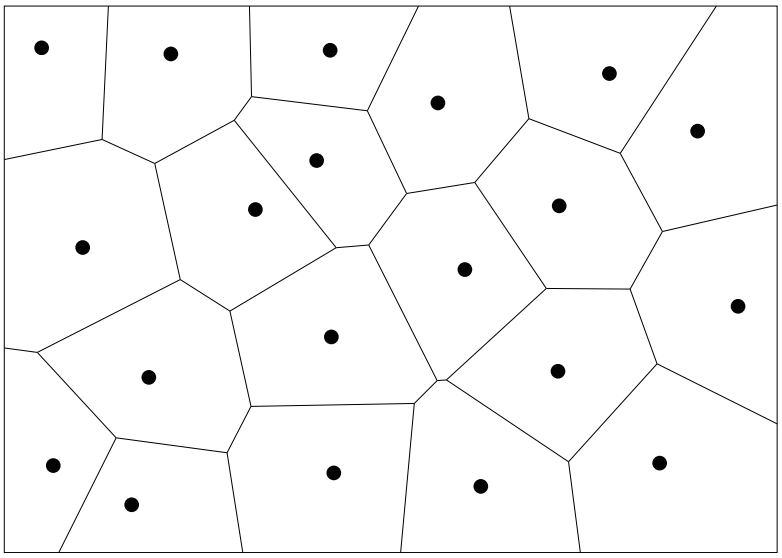

Figure 2.6: Voronoi diagram for a system with randomly distributed TIPS-Pn molecules represented by points. Note that this diagram is a 2D representation of the three-dimensional (3D) NP system.

We must now find the total density of the NP, ρ_{NP}, which is given by

$$\begin{aligned}
\rho_{\text{NP}} &= \frac{m_{\text{NP}}}{V_{\text{NP}}} \\
&= \frac{m_{\text{TIPS-Pn}} + m_{\text{PMMA}}}{V_{\text{TIPS-Pn}} + V_{\text{PMMA}}} \\
&= \frac{m_{\text{TIPS-Pn}} + m_{\text{PMMA}}}{\frac{m_{\text{TIPS-Pn}}}{\rho_{\text{TIPS-Pn}}} + \frac{m_{\text{PMMA}}}{\rho_{\text{PMMA}}}} \\
&= \frac{m_{\text{TIPS-Pn}} + m_{\text{PMMA}}}{\frac{m_{\text{TIPS-Pn}}\rho_{\text{PMMA}} + m_{\text{PMMA}}\rho_{\text{TIPS-Pn}}}{\rho_{\text{TIPS-Pn}}\rho_{\text{PMMA}}}}.
\end{aligned}$$

Again, using Equation 2.14,

$$\begin{aligned}
\rho_{\text{NP}} &= \frac{(1+\alpha)m_{\text{TIPS-Pn}}}{\frac{m_{\text{TIPS-Pn}}\rho_{\text{PMMA}} + \alpha m_{\text{TIPS-Pn}}\rho_{\text{TIPS-Pn}}}{\rho_{\text{TIPS-Pn}}\rho_{\text{PMMA}}}} \\
\therefore \rho_{\text{NP}} &= \frac{(1+\alpha)\rho_{\text{TIPS-Pn}}\rho_{\text{PMMA}}}{\rho_{\text{PMMA}} + \alpha\rho_{\text{TIPS-Pn}}}. \qquad (2.17)
\end{aligned}$$

Substituting Equation 2.17 into 2.16 gives

$$\begin{aligned}
V_{V_{\text{TIPS-Pn}}} &= \frac{(1+\alpha)MW_{\text{TIPS-Pn}}}{\left(\frac{(1+\alpha)\rho_{\text{TIPS-Pn}}\rho_{\text{PMMA}}}{\rho_{\text{PMMA}} + \alpha\rho_{\text{TIPS-Pn}}}\right)N_A} \\
\therefore V_{V_{\text{TIPS-Pn}}} &= \frac{(\rho_{\text{PMMA}} + \alpha\rho_{\text{TIPS-Pn}})MW_{\text{TIPS-Pn}}}{\rho_{\text{TIPS-Pn}}\rho_{\text{PMMA}}N_A}. \qquad (2.18)
\end{aligned}$$

2.5.2 Average Intermolecular TIPS-Pn Separation in a NP

As working in average volumes is confusing, we aim to convert this volume into an average distance. For simplicity, we consider all TIPS-Pn molecules to be placed in a 3D cubic lattice structure, with each TIPS-Pn contained in a simple cubic unit cell (refer to Figure 2.7). Then the length of the side of each cell, d, is what we define as the "average intermolecular TIPS-Pn separation". Therefore,

$$\begin{aligned} d^3 &= V_{V_{\text{TIPS-Pn}}} \\ d &= \sqrt[3]{V_{V_{\text{TIPS-Pn}}}}. \end{aligned} \tag{2.19}$$

The average Voronoi volume can be used to calculate a different definition of average intermolecular TIPS-Pn separation, by assuming a different positional distribution of TIPS-Pn molecules within a NP.

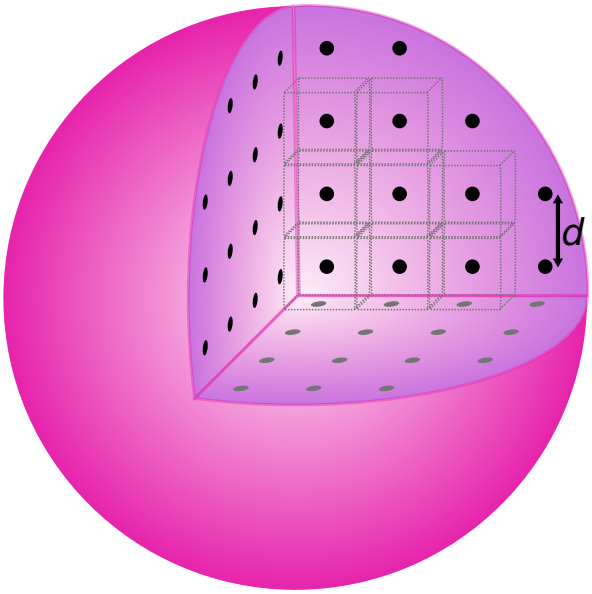

Figure 2.7: Evenly spaced TIPS-Pn molecules (represented by points) inside a NP. Each molecule can be surrounded by a cube of width d (where d is termed the "average intermolecular TIPS-Pn separation"). This means the TIPS-Pn molecules are surrounded by a volume of d^3, which we call the "average Voronoi volume" of TIPS-Pn within a NP.

2.5.3 Average Concentration of TIPS-Pn in a NP

Although the TIPS-Pn concentration in all samples was ∼100 ppm (refer to Table 2.1), we want a measure of an average concentration of TIPS-Pn within a NP, $c_{\text{TIPS-Pn}}$, which is given by

$$\begin{aligned} c_{\text{TIPS-Pn}} &= \frac{n_{\text{TIPS-Pn}}}{V_{\text{NP}}} \\ &= \frac{N_{\text{TIPS-Pn}}}{N_A V_{\text{NP}}}. \end{aligned}$$

Now substituting for V_{NP} using Equation 2.15,

$$c_{\text{TIPS-Pn}} = \frac{N_{\text{TIPS-Pn}}}{N_A N_{\text{TIPS-Pn}} V_{V_{\text{TIPS-Pn}}}} = \frac{1}{N_A V_{V_{\text{TIPS-Pn}}}}. \tag{2.20}$$

Or alternatively, if we use our definition of the average intermolecular TIPS-Pn separation, d,

$$c_{\text{TIPS-Pn}} = \frac{1}{N_A d^3}. \tag{2.21}$$

2.5.4 Summary of Equations

We summarise all useful equations here:

The average Voronoi volume of a TIPS-Pn molecule in a NP

$$V_{V_{\text{TIPS-Pn}}} = \frac{(\rho_{\text{PMMA}} + \alpha\rho_{\text{TIPS-Pn}})}{\rho_{\text{TIPS-Pn}}\rho_{\text{PMMA}}} \frac{MW_{\text{TIPS-Pn}}}{N_A} \tag{2.22}$$

The "average intermolecular TIPS-Pn separation"

$$d = \sqrt[3]{V_{V_{\text{TIPS-Pn}}}} \tag{2.23}$$

The average concentration of TIPS-Pn within a NP

$$c_{\text{TIPS-Pn}} = \frac{1}{V_{V_{\text{TIPS-Pn}}}} \frac{1}{N_A} \tag{2.24}$$

where
α is the given by the $1 : \alpha$ TIPS-Pn:PMMA mass ratio
$\rho_{\text{TIPS-Pn}} = 1104\,\mathrm{g\,L^{-1}}$
$\rho_{\text{PMMA}} = 1188\,\mathrm{g\,L^{-1}}$
$MW_{\text{TIPS-Pn}} = 639.07\,\mathrm{g\,mol^{-1}}$
$N_A = 6.022 \times 10^{23}\,\mathrm{mol^{-1}}$

We now have all relevant information to determine the average Voronoi volume of TIPS-Pn molecules in our NPs, the average intermolecular TIPS-Pn separation and the average concentration of TIPS-Pn within a NP (refer to Table 2.8).

Table 2.8: Average Voronoi volume of TIPS-Pn, average intermolecular TIPS-Pn separation and average concentration of TIPS-Pn in a NP, determined for each TIPS-Pn:PMMA NP sample (calculated using Equations 2.22 and 2.23, 2.24).

Sample (TIPS-Pn:PMMA mass ratio ($1:\alpha$))	**Average Voronoi volume of TIPS-Pn, (nm^3)**	**Average intermolecular TIPS-Pn separation, d, (nm)**	**Average concentration of TIPS-Pn in a NP ($mol\,L^{-1}$)**
1:0	0.96	0.99	1.73
1:1	1.85	1.23	0.90
1:3	3.64	1.54	0.46
1:5	5.43	1.76	0.31
1:7	7.21	1.93	0.23
1:10	9.89	2.15	0.17
1:100	90.29	4.49	0.02

CHAPTER 3
Characterisation of Aqueous TIPS-Pn/PMMA Nanoparticles

Aqueous suspensions of mixed 6,13-bis(triisopropylsilylethynyl) pentacene (TIPS-Pn) and poly(methyl methacrylate) (PMMA) nanoparticles (NPs) were prepared by the reprecipitation method, as outlined in Section 2.1.2. The resulting NPs have been shown to be a mixture of TIPS-Pn and PMMA with proportions equal to the mass ratio they were prepared with.[115] We present evidence that TIPS-Pn does not form crystalline domains within the NPs. Assuming a random arrangement of TIPS-Pn and PMMA within the NPs, the average intermolecular TIPS-Pn separation can easily be controlled by varying the TIPS-Pn:PMMA mass ratio, with larger separations resulting from higher proportions of PMMA. From this chapter onward, each NP sample will be referred to by its TIPS-Pn:PMMA mass ratio. In this chapter, we outline characteristic properties of the TIPS-Pn/PMMA NPs, presenting steady-state absorption and fluorescence spectra, and discuss degradation and colloidal stability.

3.1 Nanoparticle Formation

Aqueous suspensions of mixed TIPS-Pn and PMMA NPs with various different mass ratios were prepared by the reprecipitation method, as outlined in Section 2.1.2. These NPs have previously been prepared by our group,[115] but for completeness of this thesis, the important characteristics of this system are summarised in this chapter.

The resulting NP suspensions, as shown in Figure 3.1, are of clear blue colour with no visible aggregation when compared to TIPS-Pn in tetrahydrofuran (THF). No change in absorption was observed when comparing ultraviolet (UV)-visible absorption spectra taken before and after filtration through a filter (250 nm pores), as shown in Figure 3.4. This result confirms that the NPs are less than 250 nm in size. The colloidal NP suspensions were stable for several months, likely due to the NPs being encapsulated by the surfactant, which increases the NP stability in water. However, slight oxidation and photodegradation was observed after a few days. Section 3.3 addresses details of NP stability and degradation.

Figure 3.1: $\sim 10^{-4}$ M TIPS-Pn in THF (left) and 1:1 TIPS-Pn:PMMA NPs in water (right). Both have a concentration of ~100 ppm.

3.2 Steady-state Absorption

The UV-visible absorption spectra of the different TIPS-Pn/PMMA NPs, along with pure TIPS-Pn in THF, are shown in Figure 3.2. The absorption spectrum of TIPS-Pn in THF has vibronic peaks at 650, 590 and 550 nm representing the $S_0 \rightarrow S_1$ 0–0, 0–1, and 0–2 vibronic transitions. The smaller series from 440 nm represent the $S_0 \rightarrow S_2$ transitions. These peaks are slightly red-shifted in the TIPS-Pn/PMMA NPs, with the red-shift decreasing as the amount of PMMA is increased. This trend suggests that the TIPS-Pn molecules become more "solution-like" as the amount of PMMA increases (i.e. the average intermolecular TIPS-Pn separation decreases). Additionally, the amplitude of the vibronic transitions tend towards that of the isolated chromophores in solution, similarly observed in a previous study of pentacene NPs.[64]

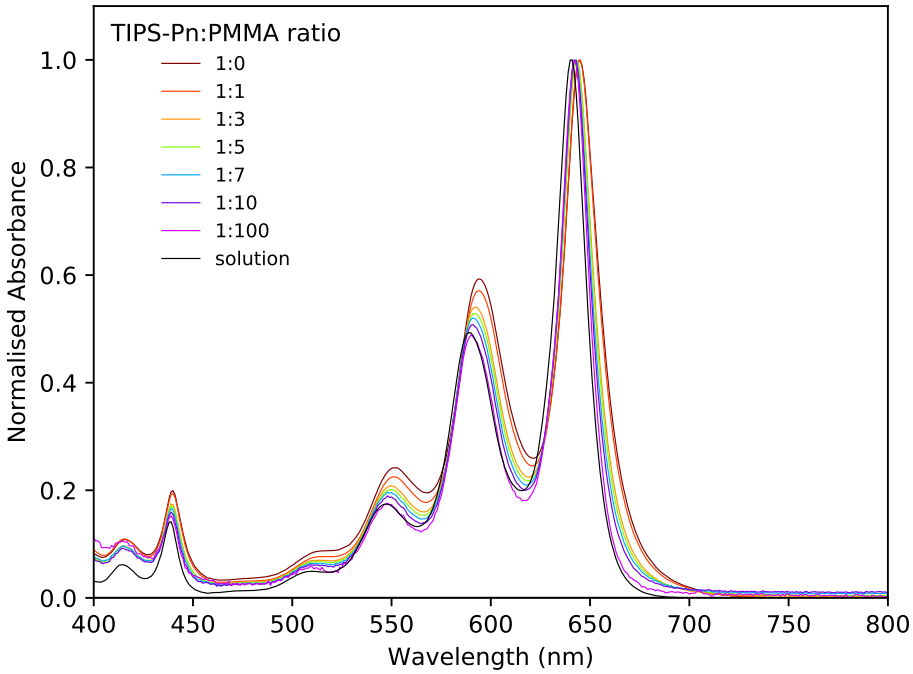

Figure 3.2: Steady-state UV-visible absorption spectra of the NPs with different TIPS-Pn:PMMA mass ratios and pure TIPS-Pn in THF. All spectra have been corrected for PMMA scattering.

Previous studies on TIPS-Pn have shown that the type of molecular packing and strength of coupling between molecules affect the steady-state spectra.[52,62] The absorption spectrum of crystalline TIPS-Pn appears significantly different to that of amorphous TIPS-Pn.[62] Pensack et al. prepared TIPS-Pn NPs with two different morphologies which displayed the same absorption spectra as amorphous and crystalline films.[60]

The similarity of the TIPS-Pn/PMMA NPs absorption spectra to that of TIPS-Pn in THF suggests relatively weak electronic coupling between TIPS-Pn molecules, implying they are arranged amorphously throughout the NPs. Furthermore, no additional peaks at 700 nm, which are representative of aggregation features, were observed. This result confirms that our NPs do not form significant amounts of strongly coupled chromophores and that a negligible amount of TIPS-Pn molecules are arranged in a slip-stacked brickstone packing motif as found in crystalline TIPS-Pn films.[33,116,117] Therefore, we first propose that TIPS-Pn molecules are randomly dispersed throughout the NP, as illustrated in Figure 3.3.

The reader is referred to Appendix 2.5.2, in which the mass ratio and densities of TIPS-Pn and PMMA are used to calculate an "average intermolecular TIPS-Pn separation", d, in each NP. These values are given in Table 3.1 and are representative values which can be used to compare the average separation of TIPS-Pn molecules across the NP samples of different TIPS-Pn:PMMA mass ratios.

However, the idea that the NPs consist of amorphous TIPS-Pn clusters cannot be excluded, as this may not necessarily be reflected in the absorption spectra. In Chapter 6, we consider our NPs to consist of amorphous clusters of TIPS-Pn and show that only with such a view of our system can we accurately reproduce our experimental data with a Monte Carlo (MC) simulation. Nevertheless, for simplicity, up until that

chapter we will consider TIPS-Pn molecules to be randomly distributed within the NP. We therefore continue with our convention of the "average intermolecular TIPS-Pn separation", d, in a NP, emphasising that this view will not undervalue our discussions for the next few chapters. The overall trend with proportion of PMMA still remains the same, because although clustering may change the median d, the average d will remain the same no matter what the distribution of TIPS-Pn molecules is.

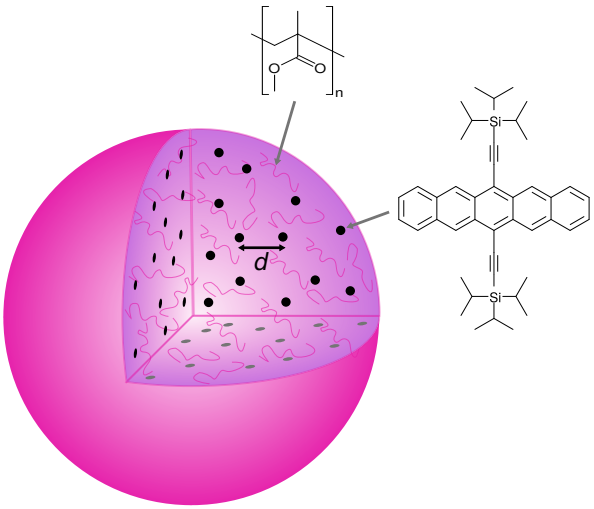

Figure 3.3: Randomly distributed TIPS-Pn molecules (represented by points) inside a PMMA NP. The TIPS-Pn molecules have an average Voronoi volume of d^3, where we refer to d as the average intermolecular TIPS-Pn separation, given in Table 3.1.

Table 3.1: Range of different TIPS-Pn:PMMA mass ratios used to prepare NPs and the corresponding average intermolecular TIPS-Pn separation, d.

Sample (TIPS-Pn:PMMA)	**Average intermolecular TIPS-Pn separation, d (nm)**
1:0	0.99
1:1	1.23
1:3	1.54
1:5	1.76
1:7	1.93
1:10	2.15

3.3 Degradation and Colloidal Stability

To determine whether our NPs aggregate or degrade, absorption spectra of the NP samples were collected over nine weeks. The steady-state absorption spectra of 1:0 and 1:10 TIPS-Pn:PMMA NPs are presented in Figure 3.4, with the other NP samples given in Appendix 3.6.

To check for aggregation, the NP samples were refiltered through 250 nm pores both one and nine weeks after preparation. Filtering the NP samples caused negligible

changes in the absorption spectra, indicating that the NPs are stable as a colloidal suspension for at least nine weeks. This is likely attributed to the surfactant increasing the NP stability in water.

However, the 1:0 TIPS-Pn:PMMA NP sample degraded by about 70% over the course of nine weeks. The 1:10 sample only degraded by 25% over the same time period. The increased chemical stability of the 1:10 sample could be due to the increased amount of PMMA limiting the contact of TIPS-Pn with the dissolved oxygen in solution.

The reduction in intensity of the 650 nm band is accompanied by an increase in absorption between 400 and 450 nm, implying the formation of a new species. TIPS-Pn has been shown to degrade to form endoperoxides upon reaction with oxygen.[118] Although the main product of the reaction, the 6,13-endoperoxide of TIPS-Pn, has no visible absorption, small quantities of 5,14-endoperoxide also form, showing visible absorption below 450 nm.[118] As this spectral feature is distinct from that observed in crystalline TIPS-Pn, we conclude that no morphological evolution of TIPS-Pn occurs.

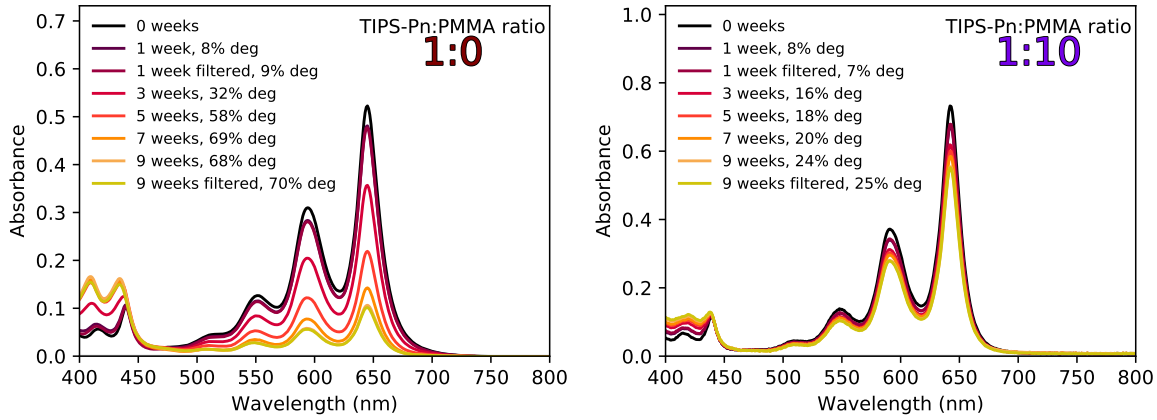

Figure 3.4: Degradation and colloidal stability of 1:0 and 1:10 TIPS-Pn:PMMA NPs over nine weeks.

To avoid degradation significantly affecting our spectroscopic measurements, the NP samples were used within 24 hours of preparation. Steady-state absorption spectra were taken before and after the spectroscopic measurements (∼5 hours of laser exposure), with samples degrading by less than 2%.

3.4 Steady-state Fluorescence

Steady-state fluorescence spectra of the different TIPS-Pn/PMMA NPs are shown in Figure 3.5. Upon excitation at 590 nm, fluorescence was detected with a peak at ∼650 nm and a slight shoulder ∼710 nm, reflecting the 0–0 and 0–1 vibronic transitions, respectively. To correct for varying concentrations of the NP samples, the fluorescence intensity was corrected for the fraction of light absorbed by dividing the fluorescence intensity by the absorption at 590 nm. It can therefore be seen that decreasing the average intermolecular TIPS-Pn separation decreases the steady-state fluorescence intensity, with negligible change in spectral shape.

The steady-state fluorescence spectra were collected from NP samples with a less than 0.1 absorbance. Therefore, self-absorption in these NP samples is minimal and

cannot account for the trend we observe in the steady-state fluorescence intensity. The quenching of the steady-state fluorescence intensity as the average intermolecular TIPS-Pn separation is decreased must therefore be due to an increase of a non-radiative decay pathway competing with fluorescence. In the following chapter, we provide evidence for an increase of a non-radiative decay, namely singlet fission (SF), for NP samples with a shorter average intermolecular TIPS-Pn separation.

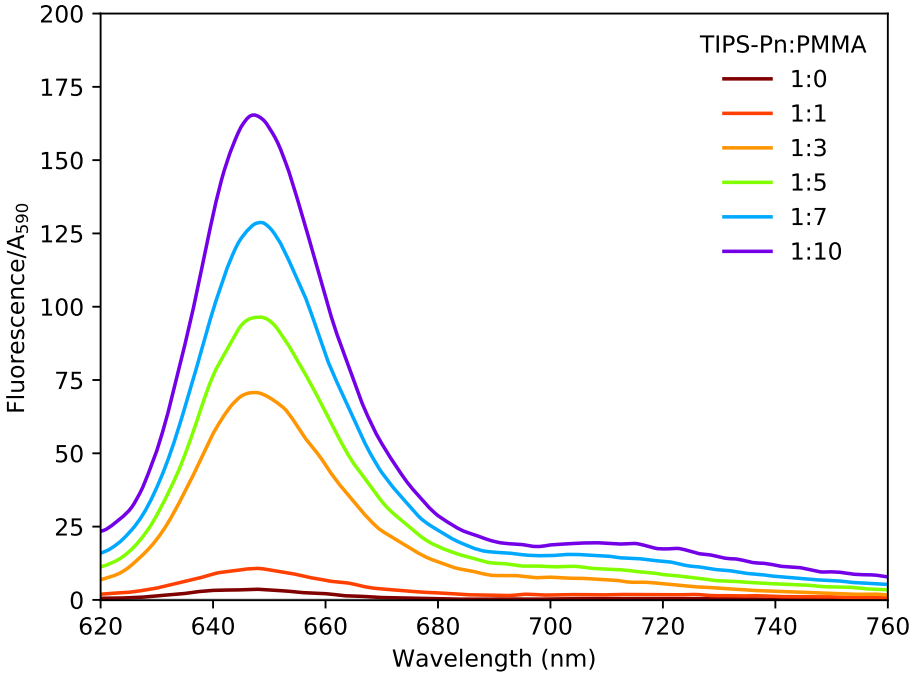

Figure 3.5: Steady-state fluorescence of the TIPS-Pn/PMMA NPs. To account for varying concentrations, the fluorescence was divided by the 590 nm absorption peak.

3.5 Conclusions

TIPS-Pn/PMMA NPs with various mass ratios have been synthesised as colloidal suspensions in water, as previously reported.[115] The visible steady-state absorption spectra of the NPs show an identical spectral shape to TIPS-Pn in THF, indicating negligible crystalline domains of TIPS-Pn are formed within the NPs. Thus, we consider TIPS-Pn molecules to be amorphously distributed within the NPs, and calculated an average intermolecular TIPS-Pn separation for all NP samples. The NPs also show colloidal stability for several weeks, with some degradation evident, but a negligible amount on the timescale of our experiments. Finally, the quenching of the steady-state fluorescence intensity for NP samples with a shorter average intermolecular TIPS-Pn separation can be attributed to an increase in a non-radiative pathway, such as SF, which will be the subject of the next chapter. Aqueous NP suspensions are an ideal system to conduct spectroscopic experiments on, as they allow for continuous sampling of new material and avoid problems like photodegradation and inhomogeneity of the sample, which are often difficulties encountered when studying films.

3.6 Appendix: Nanoparticle Stability

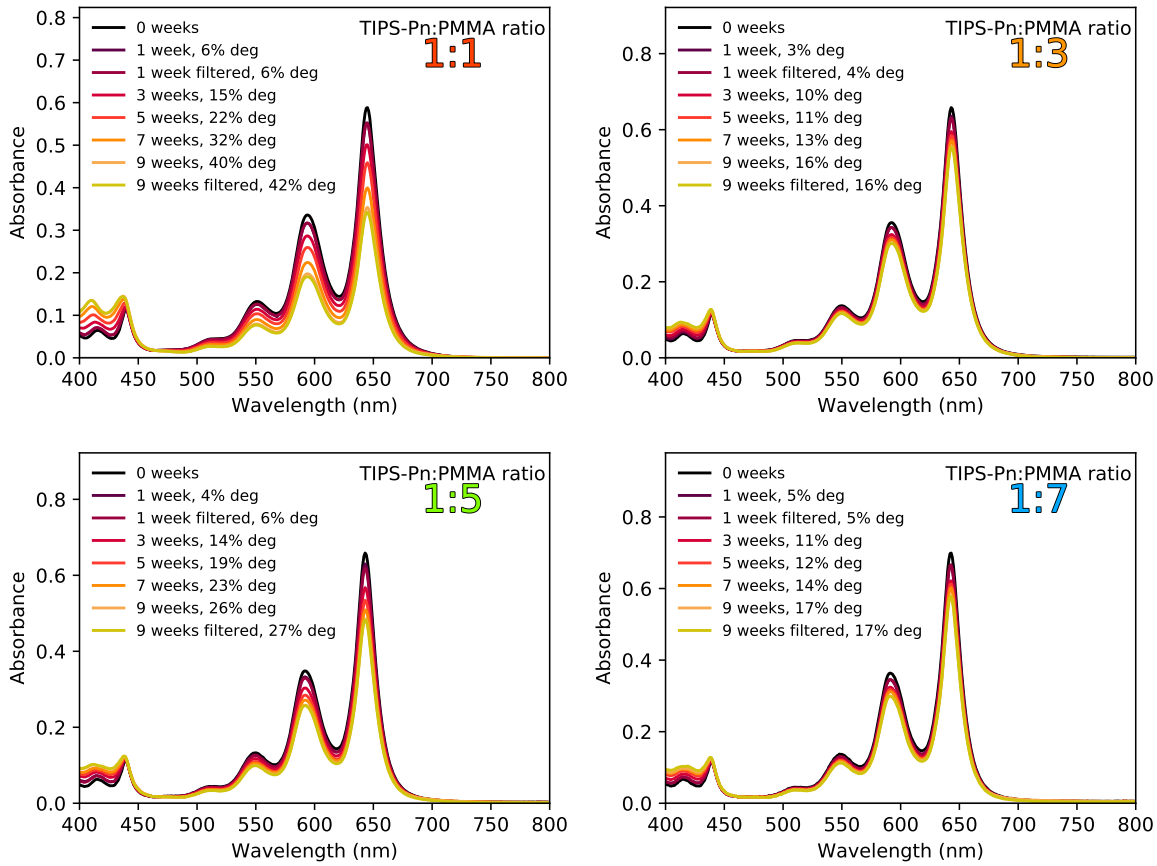

Figure 3.6: Degradation and colloidal stability of the 1:1, 1:3, 1:5 and 1:7 TIPS-Pn:PMMA NPs over nine weeks.

CHAPTER 4
Spectroscopic Analysis of Singlet Fission in TIPS-Pn/PMMA Nanoparticles

The 6,13-bis(triisopropylsilylethynyl) pentacene (TIPS-Pn)/poly(methyl methacrylate) (PMMA) nanoparticles (NPs) described in Chapter 3 provide a unique way of controlling the average intermolecular TIPS-Pn separation and thus allow us to investigate the effect of interchromophore separation on singlet fission (SF) dynamics and related processes. In this chapter, the evolution of the excited states in the various TIPS-Pn/PMMA NPs are studied using ultrafast time-resolved spectroscopic techniques. Time-resolved fluorescence gives insight into the singlet lifetime of each NP sample, while transient absorption (TA) measurements additionally provide evidence for the presence of triplets. Together, they confirm SF occurs in our NPs. We quantitatively show that the amount of SF occurring increases with decreasing average intermolecular TIPS-Pn separation.

4.1 Time-resolved Fluorescence

As described in Section 3.4, the steady-state fluorescence of the TIPS-Pn/PMMA NPs was found to be quenched for samples with decreasing average intermolecular TIPS-Pn separation. This behaviour was investigated through decay kinetics of the 655 nm fluorescence peak, using time-resolved fluorescence measurements.

We explore fluorescence decay on two different timescales. Time-correlated single photon counting (TCSPC) allows fluorescence decay dynamics to be studied on the nanosecond timescale, while fluorescence upconversion (UC) allows exploration of the decay on the picosecond timescale. These two processes are described in detail in Sections 2.3.2 and 2.3.1. Fluorescence pump power dependence studies are given in Appendix 4.4.1, and we note that negligible singlet-singlet annihilation occurs for the chosen pump power of the following experiments.

4.1.1 Time-correlated Single Photon Counting

Previously, Stuart et al. obtained TCSPC measurements of all the TIPS-Pn/PMMA NP samples studied here.[57] In addition, TCSPC measurements of $\sim 10^{-4}$ M TIPS-Pn in tetrahydrofuran (THF) were obtained.[57] This sample was considered to be sufficiently dilute to assume negligible intermolecular interactions between TIPS-Pn molecules over the timescale of the experiment and thus no additional singlet decay pathways (such as SF) existed.[52,57] Accordingly, the data could be fit to a single-exponential with a time constant of 12 ns, which was assigned to the intrinsic singlet lifetime and found to agree well with literature.[51,52]

As to not repeat the experiments by Stuart et al., we only present the 1:10 and 1:100 TIPS-Pn:PMMA NP samples in Figure 4.1. The corresponding fits are given in Table 4.1, which show agreement with previous results.[57] The 1:100 NP sample, having an average intermolecular TIPS-Pn separation of $\sim$5 nm, is expected not be able to undergo SF. The TCSPC of the 1:100 NP sample fits with a single 12 ns exponential decay reflecting the natural singlet lifetime, confirming that negligible SF occurs in this sample.

Stuart et al. further fit all of the TIPS-Pn/PMMA NP samples to a sum of exponentials, $I(t) = \sum_n A_n e^{-\frac{t}{\tau_n}}$, and convoluted with a Gaussian instrument response function (IRF) of 0.6 ns, to find that each NP sample could be fit using 2 exponentials with the long time constant fixed to 12 ns.[57] The amplitude of this long 12 ns time component decreased with decreasing average intermolecular TIPS-Pn separation. Owing to the slow IRF of the TCSPC data, these data could not be used to draw significant conclusions from the short time constants.[57] Instead, we turn to the fluorescence UC data to analyse faster decays in the fluorescence of our NP samples.

Table 4.1: Fitting parameters for TCSPC data of the 1:10 and 1:100 TIPS-Pn:PMMA NPs.[a]

Sample	A_1[b]	τ_1 (ns)	A_2	τ_2[†] (ns)
1:10	0.89±0.01	1.50±0.03	0.112±0.004	12
1:100	-	-	1.00±0.04	12

[a] Data fitted with an IRF of 0.6 ns. [b] Normalised amplitudes. [†] Fixed to the intrinsic singlet lifetime. Unconstrained parameters are shown with a 90% confidence interval.

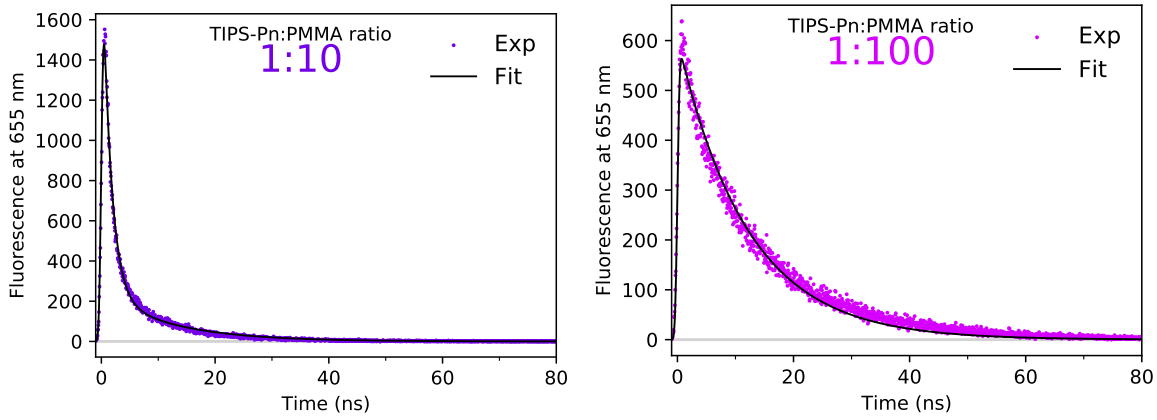

Figure 4.1: TCSPC data for the 1:10 and 1:100 TIPS-Pn:PMMA NPs. The 1:100 sample fits to a single-exponential decay of 12 ns, representing the intrinsic lifetime of singlets, and the 1:10 sample fits to a sum of 2 exponentials, with the longer time constant being 12 ns.

4.1.2 Fluorescence Upconversion

Stuart et al. also analysed the fluorescence UC of the TIPS-Pn/PMMA NPs, upon exciting the $S_0 \rightarrow S_2$ transition of TIPS-Pn with 400 nm.[57] The fluorescence UC data presented in this thesis are for NPs which have been excited with 590 nm (i.e. $S_0 \rightarrow S_1$ transition in TIPS-Pn), for consistency with later time-resolved polarisation anisotropy measurements. As the $S_2 \rightarrow S_1$ relaxation occurs rapidly in TIPS-Pn, the excitation energy chosen by Stuart et al. should have negligible effect on fluorescence decay kinetics compared to those when the $S_0 \rightarrow S_1$ transition is excited. Therefore, the fluorescence UC decays of our NP samples and those of Stuart et al. should be indistinguishable. However, due to the sensitivity of the NP preparation, it is possible that the true TIPS-Pn:PMMA mass ratios are slightly different to what is reported. This would in turn be reflected in the spectroscopic measurements. It is therefore important that the magic-angle and anisotropy measurements from fluorescence UC and TA presented in this thesis are obtained using the exact same sample. Consequently, we present the fluorescence UC of the TIPS-Pn/PMMA NPs for completeness of this thesis.

Figure 4.2 shows the fluorescence UC decay kinetics over 2.5 ns and 300 ps for all samples. Figure 4.3 shows individual traces for each sample fitted to a sum of exponentials, $I(t) = \sum_n A_n e^{-\frac{t}{\tau_n}}$, and convoluted with a Gaussian instrument response function of 0.45 ps. The fit parameters are given in Table 4.2. Each fluorescence UC decay can be fit with 3 or less exponentials ($n \leq 3$) with time constants τ_1, τ_2, and τ_3 representing fast, intermediate and slow decay time constants, respectively. As the time window of fluorescence UC is much shorter than the long time component, τ_3 was fixed to the natural singlet lifetime of 12 ns determined from TCSPC data.[57] τ_1 and τ_2, were fit without constraints.

As in TCSPC data, the amplitude of the long time component is found to decrease with decreasing TIPS-Pn separation. As the long time component represents the natural singlet lifetime, this trend suggests that as the average intermolecular TIPS-Pn separation decreases, non-radiative decay pathways become more dominant. For the 1:0 and 1:1 samples, in which the average intermolecular TIPS-Pn separations are small, the fluorescence decay can be fit without this long time component, suggesting that these samples contain a non-radiative decay pathway which is significantly faster

than the natural singlet decay ($S_1 \rightarrow S_0$).

The 1:0 sample fits to a single, fast exponential with $\tau_1 = (2.6 \pm 0.2)$ ps. As the proportion of PMMA increases, and consequently the average intermolecular TIPS-Pn separation increases, the amplitude of this τ_1 becomes smaller and hence the amplitude of the intermediate time component, τ_2 (∼30–450 ps), becomes more dominant. The need for a second intermediate time component suggests a second type of non-radiative decay pathway, or a second population of singlets.[55,92] This has been assigned to the diffusion of singlets,[57] a process which is not well represented by a single exponential, and therefore τ_2 has significant uncertainties. The time constants of both τ_1 and τ_2 also become slower with increased TIPS-Pn separation.

Figure 4.2 highlights the faster decrease in fluorescence intensity as the average intermolecular TIPS-Pn separation is decreased. We mentioned in Section 3.4 that the quenching of the steady-state fluorescence intensity with decreasing TIPS-Pn separations is likely due to an increase of a non-radiative decay pathway. We now turn to TA measurements to elucidate the non-radiative decay pathway present in our NPs.

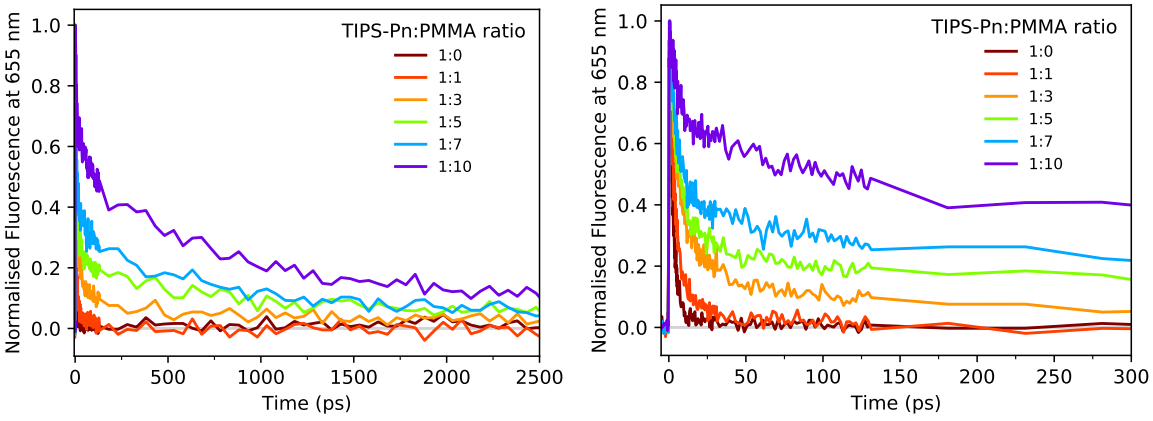

Figure 4.2: Time-resolved fluorescence UC data for the TIPS-Pn/PMMA NPs upon 590 nm excitation **(a)** over 2.5 ns and **(b)** over 300 ps.

Table 4.2: Fitting parameters for the fluorescence UC data of the TIPS-Pn/PMMA NPs.[a]

Sample	A_1 [b]	τ_1 (ps)	A_2	τ_2 (ps)	A_3	τ_3 [†] (ps)
1:0	1.00±0.05	2.6±0.2	-	-	-	-
1:1	0.87±0.05	3.3±0.4	0.13±0.05	32±17	-	-
1:3	0.73±0.03	5.3±0.5	0.22±0.03	67±19	0.04±0.01	12000
1:5	0.70±0.03	5.3±0.5	0.21±0.03	148±44	0.09±0.01	12000
1:7	0.61±0.02	5.2±0.5	0.29±0.02	296±75	0.09±0.02	12000
1:10	0.37±0.02	7±1	0.47±0.02	426±77	0.16±0.02	12000

[a] Data fitted to a multi-exponential function $I(t) = \sum_n A_n e^{-t/\tau_n}$ with an IRF of 0.45 ps. [b] Normalised amplitudes so $\sum_n |A_n| = 1$. [†] Fixed to the intrinsic singlet lifetime. Unconstrained parameters are shown with a 90% confidence interval.

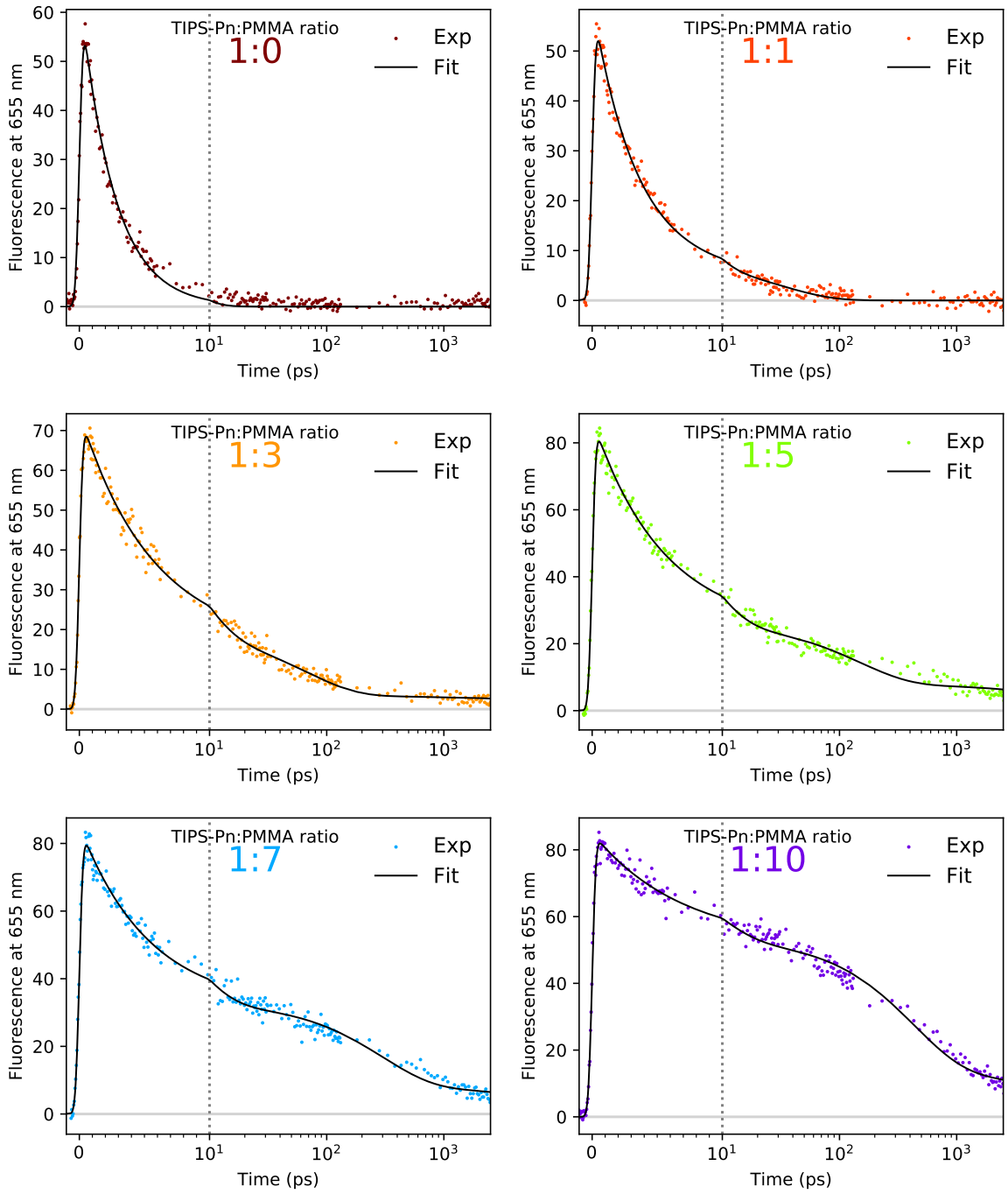

Figure 4.3: Fitted fluorescence UC data for the TIPS-Pn/PMMA NPs. All samples are fit to a sum of exponentials with a long time constant of 12 ns, with fit parameters given in Table 4.2. The dotted grey lines indicate a change from a linear to logarithmic scale.

4.2 Transient Absorption Spectroscopy

To elucidate the origin of the non-radiative decay pathway established from the time-resolved fluorescence, TA measurements were obtained as described in detail in Section 2.3.3. We excite the $S_0 \rightarrow S_1$ transition of TIPS-Pn with 590 nm and monitor the change in absorbance (ΔA) in the visible (450–800 nm) and near-infrared (NIR) (800–1400 nm) regions. TA pump power dependence studies are given in Appendix 4.4.2 and

4.4.4, and we note that negligible exciton-exciton annihilation occurs for the chosen pump power of the following experiments.

4.2.1 Visible Transient Absorption

Stuart et al. presented TA data for the TIPS-Pn/PMMA NPs in the visible region, exciting the $S_0 \rightarrow S_2$ transition of TIPS-Pn with 400 nm. As the $S_2 \rightarrow S_1$ relaxation occurs rapidly in TIPS-Pn, the excitation energy has minor impact on the exciton dynamics and decay products.[57] However, the relaxation from $S_2 \rightarrow S_1$ changes the singlet dipole moment,[33,38,61] which is not ideal for the anisotropy measurements. For completeness of this thesis and consistency with the excitation wavelength for the anisotropy data presented in the next chapter, we present the TA data at magic angle for our NPs upon excitation of the $S_0 \rightarrow S_1$ transition.

Direct excitation of $S_0 \rightarrow S_1$ to the lowest S_1 vibrational state would be achieved by 650 nm. However, we do not want to obstruct our spectra at this wavelength as this corresponds to the ground-state bleach (GSB) of TIPS-Pn. We therefore excite the $S_0 \rightarrow S_1$ to a higher S_1 vibrational state with 590 nm. Thus, we cannot analyse our data between 580 and 600 nm because the excitation wavelength interferes with ΔA in this region. The 475 nm and 508 nm peak kinetics are observed upon excitation of the 1:0 and 1:10 samples with 590 nm and 650 nm, as shown in Appendix 4.4.3. With minimal difference, we conclude that the excitation wavelength has minor impact on the TA dynamics.

We first aim to present a singlet and triplet TA spectra so they can be used to distinguish singlet and triplet features in the TA spectra of the TIPS-Pn/PMMA NP samples. As discussed in Section 4.1.1, the concentration of the $\sim 10^{-4}$ M TIPS-Pn in THF sample is dilute enough not to undergo SF. Consequently, the TA spectrum can, over the timescale of our experiments, be considered to be due to singlets only. Although a singlet spectrum could be extracted from the dilute TIPS-Pn in THF sample, it is not a representative of a singlet spectrum in the NP environment. Hence, we turn to the 1:100 NP sample. Figure 4.4 displays ΔA of the TIPS-Pn in THF sample and the 1:100 NP sample. These spectra match closely, with subtle difference being attributed to differences in environment (PMMA versus THF). The dynamics of both samples are also nearly identical. We therefore use the 1:100 NP sample, at 10 ps, as a representative of a singlet spectrum in the NP environment. For a triplet spectrum, a sample which undergoes SF rapidly is required. For the 1:0 sample, fluorescence UC shows all singlets have decayed by $\sim$50 ps. As this sample is considered to have a small enough TIPS-Pn separation for SF to occur rapidly, the TA spectrum from this time forward should be largely due to triplets. It must be noted that the triplet-pair, ^{1}(TT), may also be present. However, both ^{1}(TT) and free triplets exhibit a similar spectrum,[50] so it is still valid to extract a triplet-like spectrum from this 1:0 sample at 3 ns.

To summarise, Figure 4.5 shows the characteristic shape of the singlet and triplet spectra. They are used to quantitatively show that SF occurs in our NP samples. For a more qualitative analysis, the reader is referred to the detailed study by Stuart et al.[57] Due to the limitations of the concentration of the 1:100 NP sample, we do not attempt to analyse its time-resolved spectra in detail.

We can now focus on the 1:0 to 1:10 samples. Two-dimensional (2D) TA heat maps, as well as spectra taken at various times, are presented in Figures 4.6 and 4.7. The TA

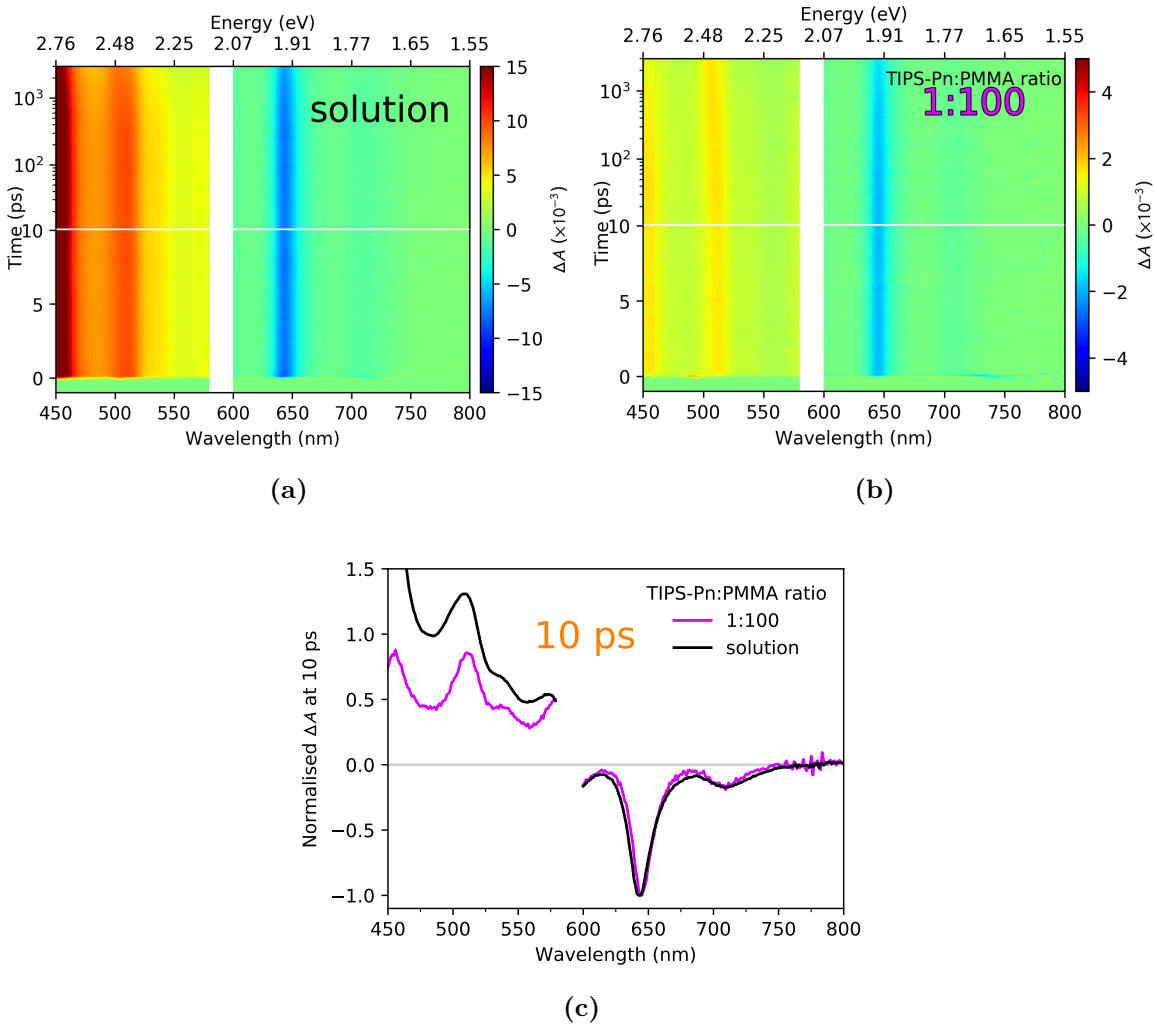

Figure 4.4: TA spectra for **(a)** $\sim 10^{-4}$ M TIPS-Pn in THF and **(b)** TIPS-Pn/PMMA NPs. Data are cut from the 580–600 nm region due to interference with the excitation wavelength. The horizontal white lines on these plots indicate a change from a linear to logarithmic scale. **(c)** ΔA at 10 ps for each sample, normalised to the 650 nm peak.

spectra show similar spectral features to previously studied TIPS-Pn NPs.[55,57,60] All samples show a negative GSB around 650 nm, corresponding to the $S_0 \rightarrow S_1$ 0–0 vibronic transition seen in the steady-state absorption (Figure 3.2, Section 3.2). The stimulated emission (SE) around 725 nm is most evident at early times for the NP samples with a higher proportion of PMMA, and corresponds to the weaker 0–1 shoulder in the steady-state fluorescence (Figure 3.5, Section 3.4). The stronger 0–0 SE component should be close to 650 nm, therefore overlapping with the GSB. Further overlap with the GSB region occurs from positive excited-state absorption (ESA) features due to several species, dominating over the 450–650 nm region. At early times and for the NP samples with a high proportion of PMMA, the most prominent of these peaks are around 450 nm and 508 nm. These peaks have been attributed to the $S_1 \rightarrow S_n$ transitions,[51] and are in accordance with the features present in the singlet spectrum (refer to Figure 4.4). For the 1:10 sample, the decay of the 450 nm peak reveals a peak around 475 nm and is accompanied with a rise in the ESA peak around 508 nm (refer to Figure 4.7). The peak around 508 nm has also been attributed to the $T_1 \rightarrow T_3$ transition,[20,119] and is in accordance with the features present in the triplet spectrum

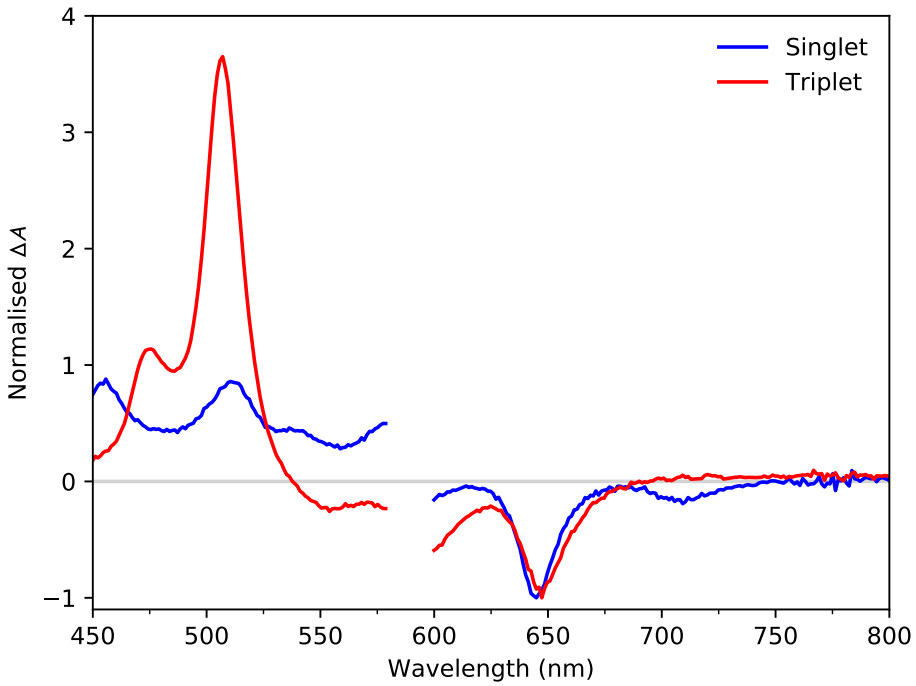

Figure 4.5: The singlet and triplet spectra extracted at 10 ps from the 1:100 sample and 3000 ps from the 1:0 sample, respectively. For simplicity, the GSB is incorporated into these spectra.

(refer to Figure 4.5). Therefore, the rise of the ∼508 nm peak indicates the production of triplets.[51,54,55] The rise of this triplet peak occurs within 10 ps, which is too fast to be attributed to intersystem crossing (ISC).[52,54] Furthermore, due to the concurrent decrease in the singlet GSB and SE features, we attribute the increase in the triplet ESA to the production of triplets by SF.

Focusing on the 1:10 sample, the SE around 710 nm and singlet ESA feature around 450 nm can clearly be seen at early times (refer to Figure 4.7). These features decay with concurrent rise of the triplet ESA, with the ∼508 nm peak reaching a maximum at ∼1000 ps. As the proportion of PMMA is decreased, the singlet features decay much faster, accompanied by a much faster rise in the triplet ESA features. For the 1:0 sample, minimal singlet ESA features are present, and the triplet peak around 508 nm reaches a maximum within ∼100 ps (refer to Figure 4.6). In summary, the faster decay of the singlet features as the average intermolecular TIPS-Pn separation decreases is consistent with the decrease in fluorescence lifetimes with decreasing proportion of PMMA, as discussed in Section 4.1. Furthermore, the faster rise of the triplet features demonstrates the increased rate of SF as the average intermolecular TIPS-Pn separation is decreased.

We refrain from analysing the 650 nm peak in detail as it contains overlapping contributions from the GSB, SE and ESA. SF results in splitting a singlet into two triplets, resulting in an additional bleached molecule (refer to Figure 1.3). This would suggest a growth in the magnitude of the GSB signal. However, SF reduces the presence of singlets, thereby reducing the amount of SE present, and consequently the magnitude of the 650 nm signal would decrease. The two competing contributions (GSB and SE) result in an overall decrease in the 650 nm peak over time, for all mass ratios.

Also worth noting is the broad ESA feature at 750 nm. This feature grows as

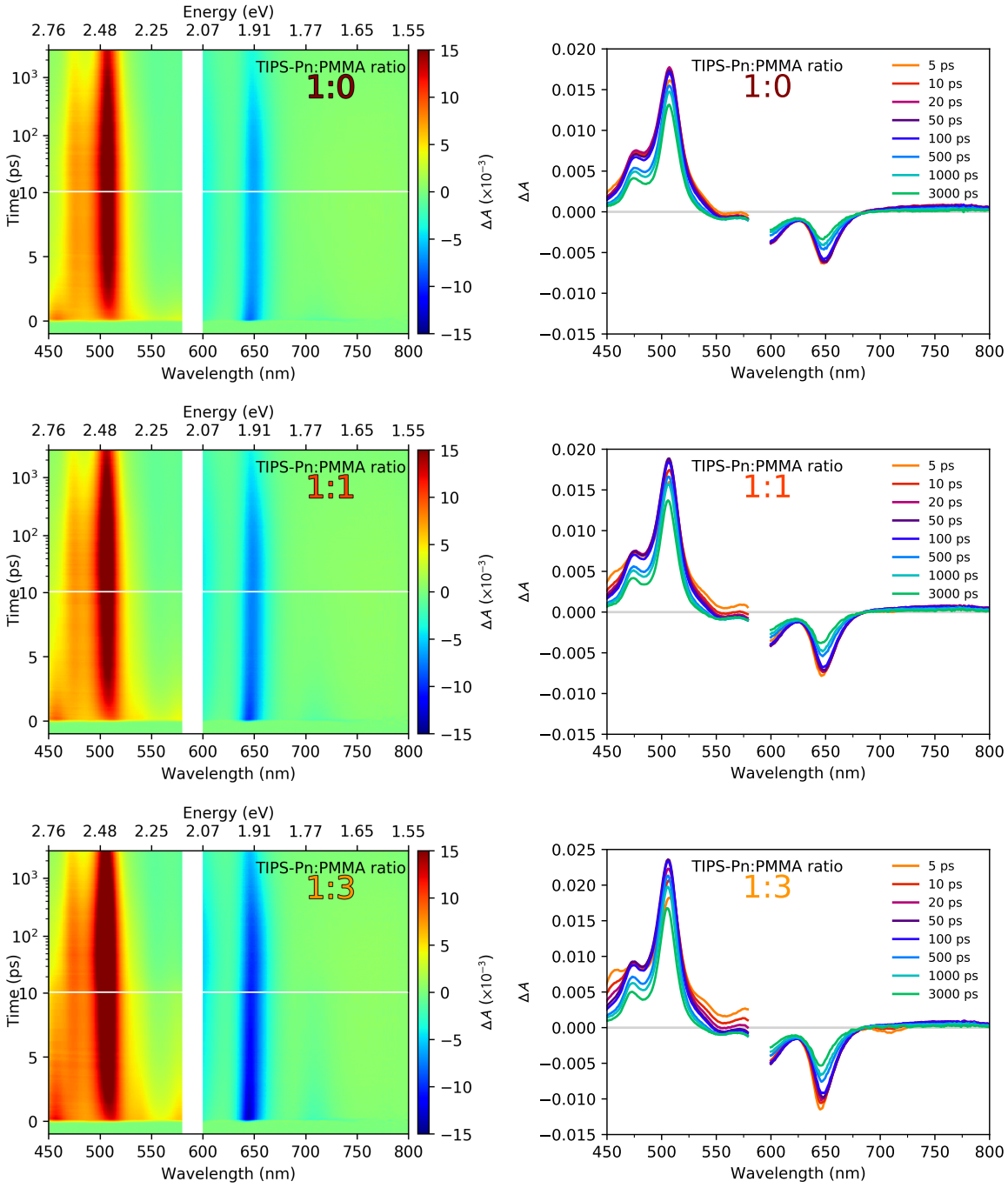

Figure 4.6: TA spectra for the 1:0 to 1:3 TIPS-Pn:PMMA NPs. 2D heat maps are shown on the left, with spectra taken at various times on the right. Data are cut from the 580–600 nm region due to interference with the excitation wavelength. The horizontal white lines on the left plots indicate a change from a linear to logarithmic scale.

singlets are depleted. Although slight overlap with the SE around 710 nm, Stuart et al. observed that this ESA neither directly corresponds to the singlet decay nor the rise of the triplet. This result suggests the presence of another component, which Stuart et al. discussed in detail, and was ultimately assigned to the triplet-pair, ^{1}(TT).[57]

Figure 4.8 shows the spectra at 5 ps of all the TIPS-Pn/PMMA NP samples studied. It is a clear way of showing that the 1:10 sample still contains strong singlet features at this time while the 1:0 sample has already adopted a mainly triplet spectrum. It

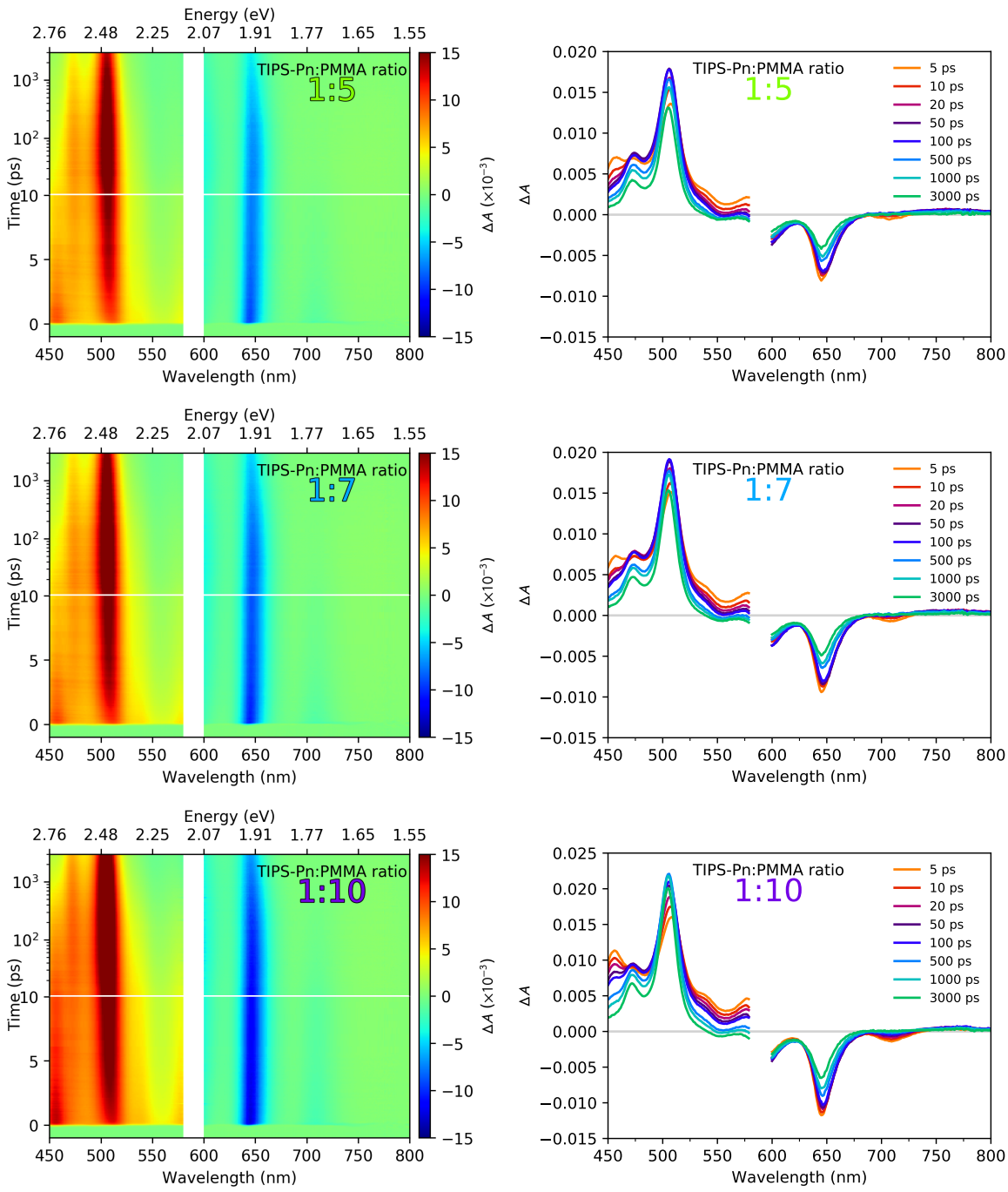

Figure 4.7: TA spectra for the 1:5 to 1:10 TIPS-Pn:PMMA NPs. 2D heat maps are shown on the left, with spectra taken at various times on the right. Data are cut from the 580–600 nm region due to interference with the excitation wavelength. The horizontal white lines on the left plots indicate a change from a linear to logarithmic scale.

also highlights the faster singlet to triplet conversion as the average intermolecular TIPS-Pn separation of the NPs decreases. The apparent isosbestic points at ∼530 and ∼670 nm are indicative of a conversion of one species to another,[55] further supporting the conversion of singlet to triplets. As each wavelength has contributions from at least two different components, it is not valid to use a single wavelength as a representative kinetic trace for a single species. It is thus necessary to deconvolute the spectra into a linear combination of basis spectra of all species contributing to the TA spectra. Stuart

et al. present a detailed deconvolution of spectra to calculate SF rates and quantum yields. A comprehensive kinetic model is also presented to explain trends in SF rates and efficiency losses of our system.[57]

The aim of this chapter is to present time-resolved fluorescence and TA data to demonstrate that SF occurs in our NPs and that it occurs faster for decreasing TIPS-Pn separation. The reader is referred to the study by Stuart et al. for quantitative SF rates and yields of the TIPS-Pn/PMMA NPs studied here.[57]

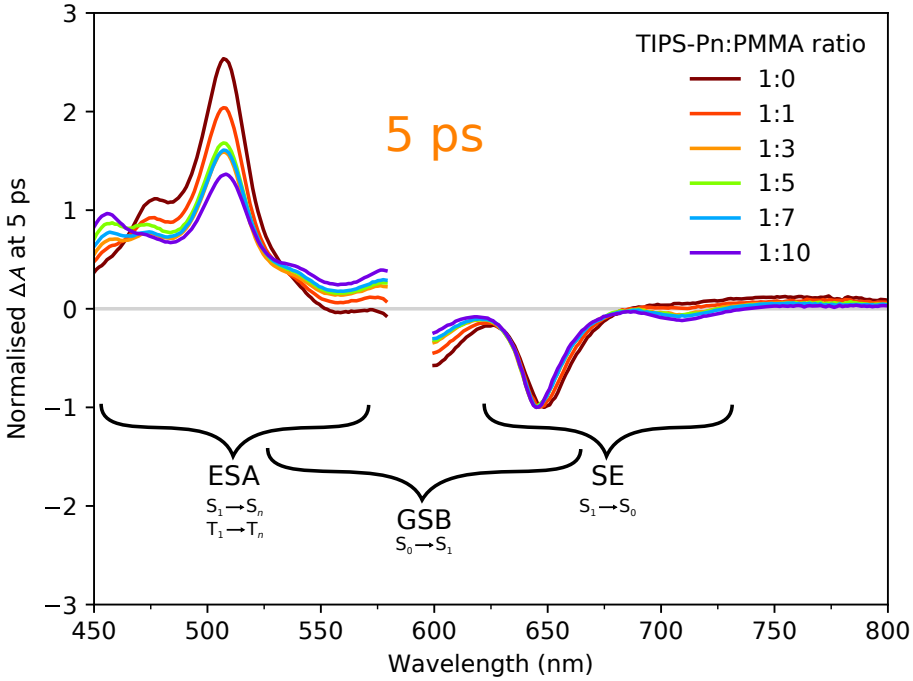

Figure 4.8: TA spectra at 5 ps for different TIPS-Pn/PMMA NPs. The shape of the spectra at early times is significantly different for the various average intermolecular TIPS-Pn separations. The overlapping contributions from the GSB, SE and ESA are shown.

4.2.2 NIR Transient Absorption

In Figure 4.9 we present TA in the NIR region, where the singlet and triplet features are more clearly separated.[60] As mentioned earlier, the dilute TIPS-Pn in THF sample can be a representative of a singlet spectrum. This matches the singlet spectrum for neat TIPS-Pn amorphous NPs presented by Pensack et al.[60] In contrast to the singlet spectrum, the triplet spectrum has a distinct peak at ∼990 nm.[60]

We only present the TIPS-Pn/PMMA NP samples which represent the shortest and longest average intermolecular TIPS-Pn separation, respectively, of the NPs studied. Both samples show a concurrent rise of the triplet peak at ∼990 nm and decay of the broad singlet feature at ∼1350 nm. Again, the triplet feature appears within 10 ps, too fast to be attributed to ISC. As concluded from TA data in the visible region, this is strong proof that SF is occurring in our NPs.

For the 1:0 sample, the broad singlet spectral feature at ∼1350 nm is evident immediately after the pump pulse and decays rapidly, to about half its signal, within 10 ps. The triplet feature at ∼990 nm rises instantly, reaching a peak within 10 ps and then decays slightly over the 3 ns time window. The 1:10 sample displays a strong

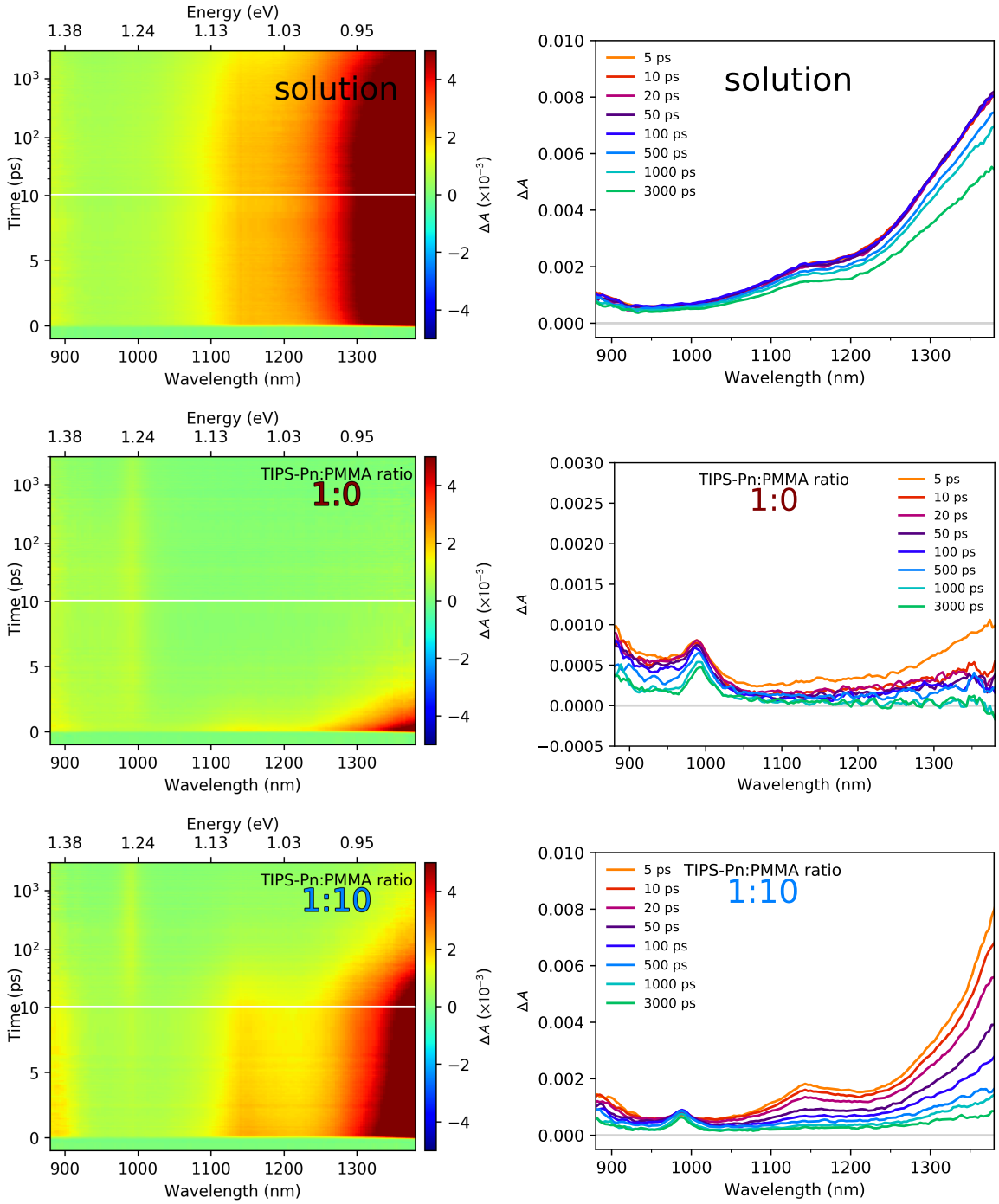

Figure 4.9: NIR TA spectra for $\sim 10^{-4}$ M TIPS-Pn in THF, and 1:0 and 1:10 TIPS-Pn:PMMA NPs. 2D heat maps are shown on the left, with spectra taken at various times on the right. The horizontal white lines on the left plots indicate a change from a linear to logarithmic scale.

singlet feature which lasts much longer. The triplet feature also takes longer to rise, reaching its peak only after ~100 ps. In contrast to the 1:0 sample which has no singlet contributions after 1 ns, the 1:10 sample still shows some singlet presence at 3 ns. This suggests not all singlets have undergone SF by this time, presumably because of the larger TIPS-Pn separation, or the presence of singlet trap sites.

The NIR TA data presented here confirms the presence of SF in our TIPS-Pn/PMMA

NPs, and as found from the visible TA data, SF occurs faster for NP samples with a shorter average intermolecular TIPS-Pn separation.

4.3 Conclusions

In this chapter we presented time-resolved fluorescence and TA data for our TIPS-Pn/PMMA NPs. The fluorescence lifetime is significantly shorter for NP samples with a shorter average intermolecular TIPS-Pn separation, indicating a faster depletion of the S_1 population. A 1:100 TIPS-Pn:PMMA NP sample has been shown to undergo negligible SF, and was thus used as a representative of a singlet TA spectrum in the NP environment. The 1:0 sample, which undergoes SF rapidly and shows no singlet contributions after ∼50 ps, was used to extract a triplet spectrum. These spectra were then used to show that the NP samples displayed a concurrent rise of triplet ESA features with the decay of singlets. These triplet features form within 10 ps, which is too fast to be attributed to ISC in TIPS-Pn. Therefore, we could conclude that triplets are formed by SF. This is further confirmed by TA data in the NIR region, which has singlet and triplet features more clearly separated than in the visible region. Both from the visible and NIR TA, a faster triplet formation was observed in NP samples with a shorter average intermolecular TIPS-Pn separation.

4.4 Appendices

4.4.1 Fluorescence Pump Power Dependence

For the 1:0 sample, no dependence on the pump power was observed (over 0.05–2.00 mW). This indicates that negligible singlet-singlet annihilation is occurring for these pump powers. For the 1:10 sample, a very slight dependence on pump power can be observed. A pump power of 0.10 mW was chosen for subsequent time-resolved fluorescence experiments to minimise singlet-singlet annihilation contributions to fluorescence dynamics.

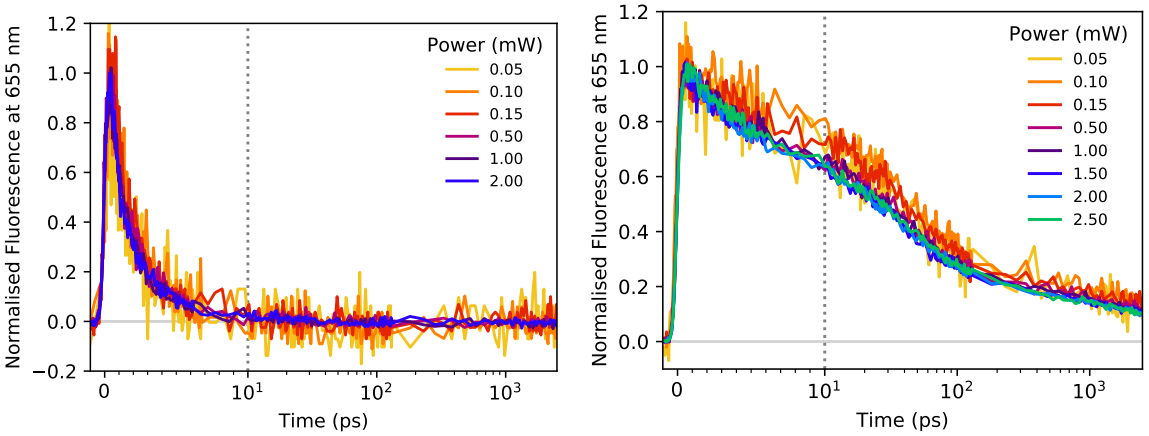

(a) **(b)**

Figure 4.10: Pump power dependence of the fluorescence for **(a)** 1:0 and **(b)** 1:10 TIPS-Pn:PMMA NPs.

4.4.2 Visible Transient Absorption Pump Power Dependence

For the 1:0 sample, a slight dependence on pump power can be observed for the GSB at 650 nm and ESA at 508 nm. The 1:10 sample however shows negligible dependence on pump power (over 0.15–2.00 mW).

A pump power dependence (i.e. an increase in exciton decay with increasing exciton concentration, or equivalently, an increasing pump power), suggests exciton-exciton annihilation is present. The 1:0 sample has the shortest average intermolecular TIPS-Pn separation, so this sample would be the most likely of all samples to show pump power dependence due to exciton-exciton annihilation. As no pump power dependence is evident for the 1:0 sample at 0.50 mW, we choose this pump power for our visible TA experiments to minimise exciton-exciton annihilation contributions to excited-state dynamics.

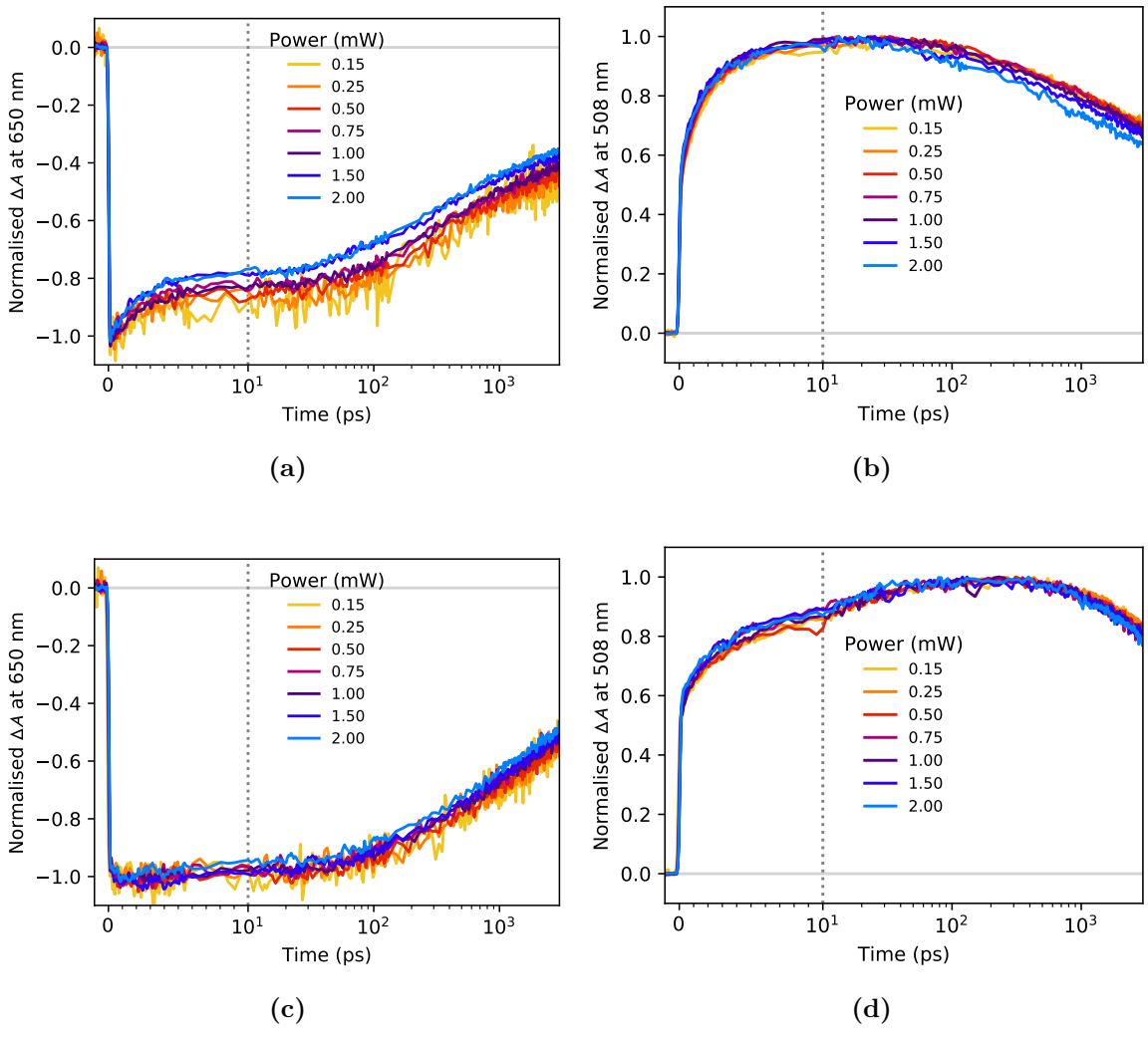

Figure 4.11: Pump power dependence of **(a)** the GSB at 650 nm for the 1:0 NPs, **(b)** the ESA at 508 nm for the 1:0 NPs, **(c)** the GSB at 650 nm for the 1:10 NPs, and **(d)** the ESA at 508 nm for the 1:10 NPs.

4.4.3 Visible Transient Absorption Wavelength Dependence

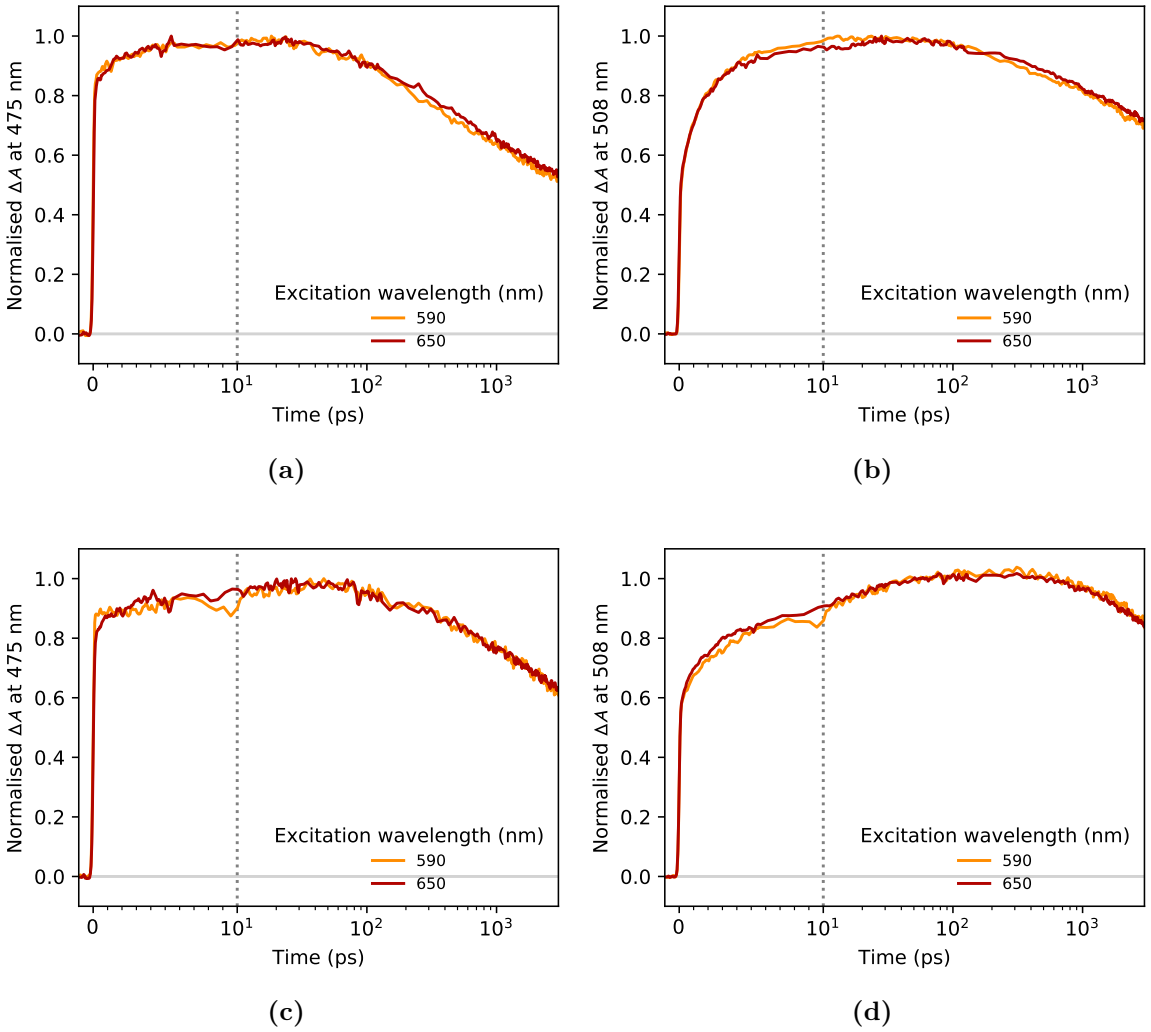

Figure 4.12: Pump wavelength dependence of the ESA features **(a)** at 475 nm for the 1:0 NPs, **(b)** at 508 nm for the 1:0 NPs, **(c)** at 475 nm for the 1:10 NPs, and **(d)** at 508 nm for the 1:10 NPs. Exciting the sample at 590 nm has the same effect as exciting at 650 nm.

4.4.4 NIR Transient Absorption Pump Power Dependence

Neither the 1:0 nor 1:10 samples show pump power dependence at 1350 nm over 0.50–2.50 mW. As this ESA is due to the singlets, this confirms that negligible singlet-singlet annihilation occurs for these pump powers.

The 1:10 sample does not show pump power dependence at 990 nm (which is a peak mostly due to triplet ESA). This result suggests that the average intermolecular TIPS-Pn separation in these NPs is large enough for there to be negligible triplet-triplet annihilation. The 1:0 sample however shows pump power dependence at 990 nm, suggesting that the average intermolecular TIPS-Pn separation in these NPs is small enough for triplet-triplet annihilation to exist at higher pump powers.

A pump power of 0.75 mW was chosen for subsequent NIR TA experiments to minimise triplet-triplet annihilation contributions to excited-state dynamics.

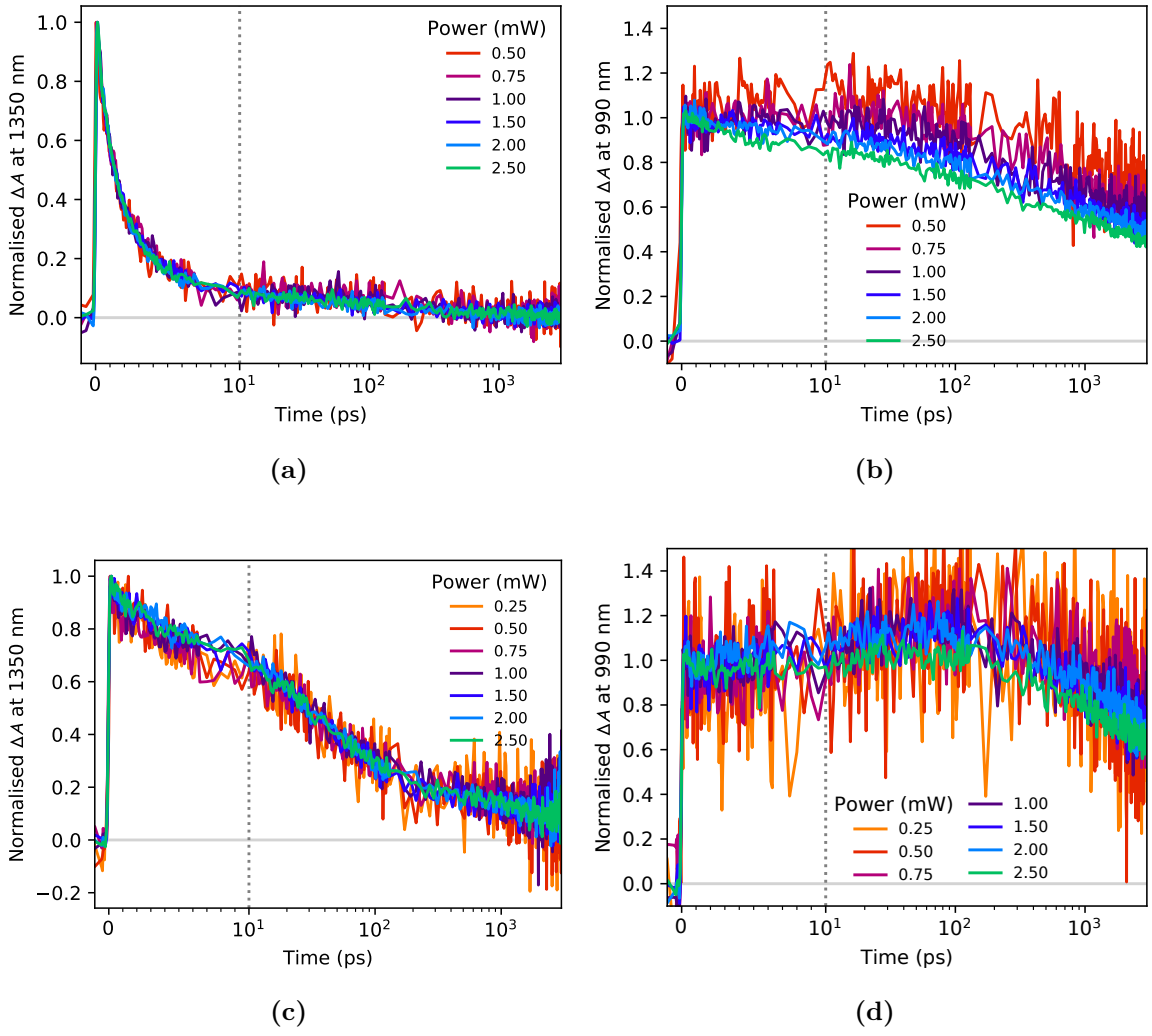

Figure 4.13: Pump power dependence of the TA **(a)** at 1350 nm for the 1:0 NPs, **(b)** at 1350 nm for the 1:0 NPs, **(c)** at 990 nm for the 1:10 NPs, and **(d)** at 990 nm for the 1:10 NPs.

4.4.5 NIR Transient Absorption Wavelength Dependence

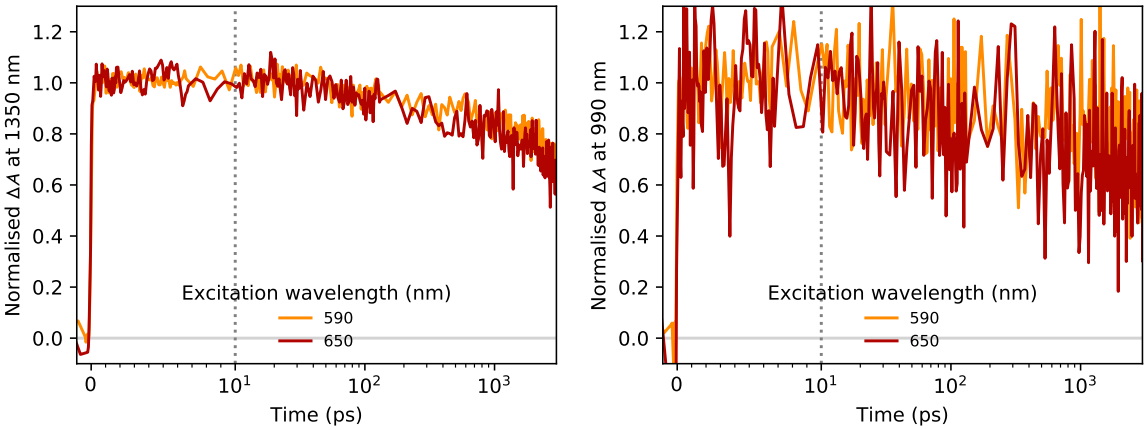

(a) **(b)**

Figure 4.14: Pump wavelength dependence for $\sim 10^{-4}$ M TIPS-Pn in THF of the TA **(a)** at 1350 nm and **(b)** at 990 nm. Exciting the sample at 590 nm has the same effect as exciting at 650 nm.

CHAPTER 5
Time-resolved Polarisation Anisotropy of TIPS-Pn/PMMA Nanoparticles

This chapter presents time-resolved fluorescence and transient absorption (TA) polarisation anisotropy measurements of the 6,13-bis(triisopropylsilylethynyl) pentacene (TIPS-Pn)/poly(methyl methacrylate) (PMMA) nanoparticles (NPs) described in Chapters 3 and 4. Time-resolved polarisation anisotropy has the potential to give insight into exciton migration within the systems. We conclude from the results presented here that the polarisation anisotropy decreases more rapidly with decreasing average intermolecular TIPS-Pn separation.

5.1 Time-resolved Fluorescence Anisotropy

Polarisation anisotropy is described in detail in Section 1.5. In short, time-resolved polarisation anisotropy measures the correlation of the excitons with the polarisation of the initial excitation over time.

The TIPS-Pn/PMMA NP samples were excited with polarised 590 nm light to promote TIPS-Pn from the S_0 to S_1 state. As mentioned in Section 4.2.1, direct excitation to the lowest vibrational level of the S_1 state would be achieved with 650 nm. However, to be able to analyse the TA kinetics and anisotropy at 650 nm (the ground-state bleach (GSB)), 590 nm was chosen as the excitation wavelength. This results in excitation to a higher vibrational level of the S_1 state, but fast relaxation to the lowest state occurs before fluorescence.

Detailed experimental methods are described in Section 2.3.5. Basically, the fluorescence intensity is detected parallel, $I_{\parallel}$, and perpendicular, $I_{\perp}$, to the excitation polarisation. The correlation of the fluorescence emission at some time, t, after the initial excitation is described by anisotropy, $r(t)$, given by

$$r(t) = \frac{I_{\parallel}(t) - I_{\perp}(t)}{I_{\parallel}(t) + 2I_{\perp}(t)}. \tag{5.1}$$

We note that the rotation of the excitation polarisation from vertical to horizontal caused slight changes in power incident on the sample. This power difference was measured and the perpendicular intensity scans were multiplied by 0.954 before the fluorescence anisotropy was calculated using Equation 5.1.

Due to the photoselection phenomena in a sample with randomly oriented chromophores (discussed in Section 1.5.2), the maximum anisotropy value is 0.4 and corresponds to a fully correlated emission. An anisotropy value of -0.2 corresponds to an emission rotated by 90°. When the anisotropy is zero, the emission has lost all correlation with the initial excitation polarisation.

There are several factors that can result in loss of correlation with the initial excitation polarisation, including rotational diffusion, exciton migration and selective elimination of excitons, as explained in Section 1.5.4.

5.1.1 Trends in the Fluorescence Anisotropy

The experimental time-resolved fluorescence anisotropy of all samples is presented in Figure 5.1. These data were fit to a sum of exponentials, $I(t) = \sum_n A_n e^{-\frac{t}{\tau_n}}$, with parameters given in Table 5.1. Appendix 5.6.1 shows the individual parallel and perpendicular scans for each sample. As fluorescence is a representation of the S_1 state, monitoring the fluorescence anisotropy over time gives insight into the depolarisation of the singlet population.

We first focus on the dilute solution of $\sim 10^{-4}$ M TIPS-Pn in THF. As discussed in Section 4.1.1, this sample does not undergo singlet fission (SF). Additionally, this sample does not undergo a significant amount of singlet migration. Thus, the main loss of polarisation occurs through rotation of TIPS-Pn molecules. The fluorescence anisotropy of this solution sample can be fit to a single time constant of $\tau_1 = (135 \pm 5)$ ps, and thus represents the rotation of TIPS-Pn molecules. This value agrees with the predicted value for the rotation of TIPS-Pn molecules in THF (refer to Appendix 5.6.3).

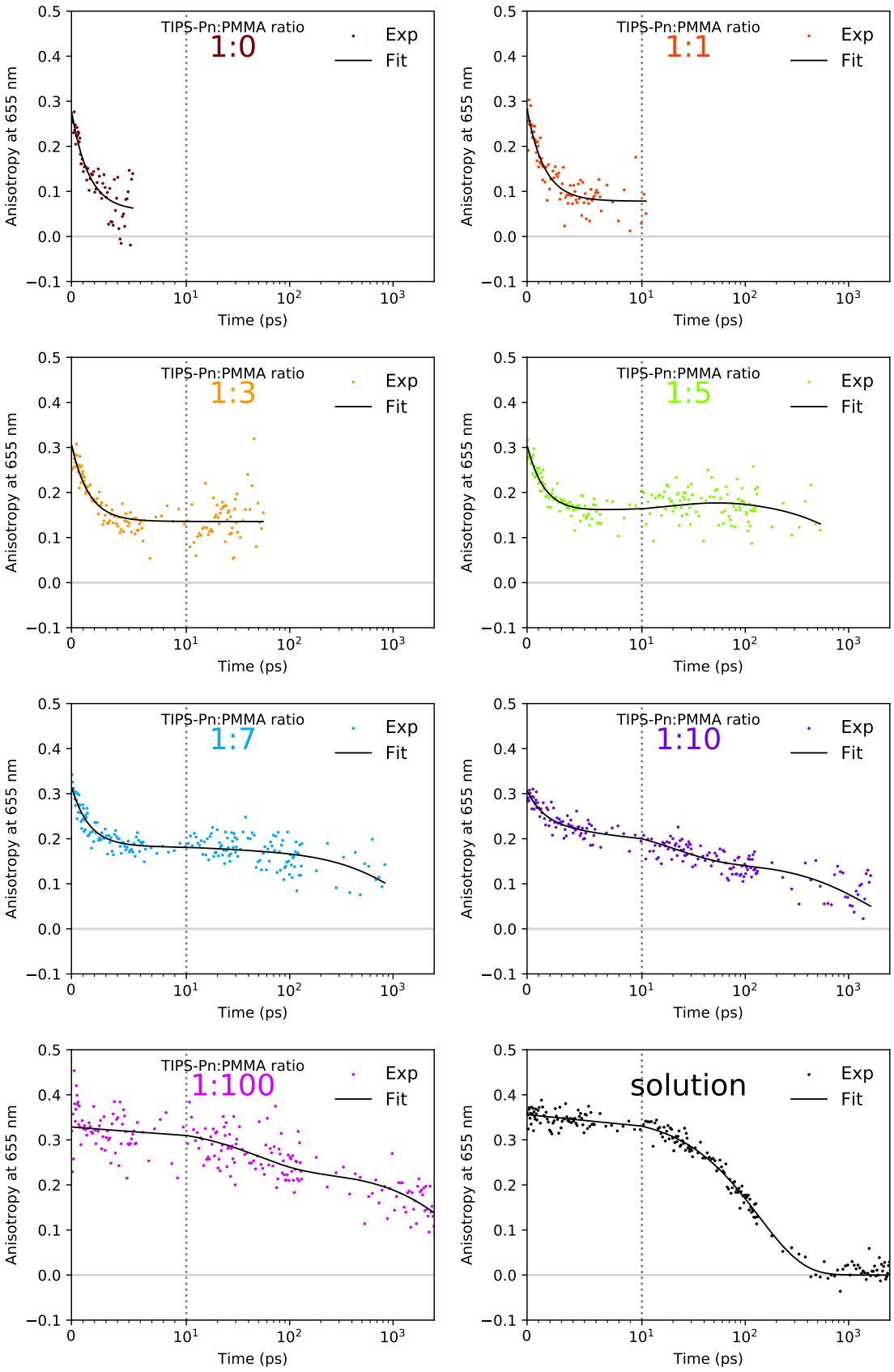

Figure 5.1: Experimental time-resolved fluorescence anisotropy for all TIPS-Pn/PMMA NPs and TIPS-Pn in tetrahydrofuran (THF). All data were fit to a sum of exponentials with parameters given in Table 5.1. The dotted grey lines indicate a change from a linear to logarithmic scale.

Table 5.1: Fitting parameters for the fluorescence anisotropy data of TIPS-Pn/PMMA NPs and TIPS-Pn in THF.[a]

Sample	A_1 [b]	τ_1 (ps)	A_2	τ_3 (ps)	A_3	τ_3 (ps)
1:0	0.80±0.09	1.5[†]	-	-	0.20±0.04	∞ [‡]
1:1	0.72±0.06	1.5[†]	-	-	0.28±0.03	∞ [‡]
1:3	0.56±0.06	1.5[†]	-	-	0.44±0.02	∞ [‡]
1:5	0.41±0.05	1.5[†]	-0.09±0.03	20[†]	0.50±0.02	1500[†]
1:7	0.41±0.05	1.5[†]	0.02±0.04	20[†]	0.56±0.02	1500[†]
1:10	0.24±0.05	1.5[†]	0.28±0.03	20[†]	0.49±0.02	1500[†]
1:100	0.29±0.08	47±48	-	-	0.71±0.07	4800±3900
solution	1.00±0.01	134±5	-	-	-	-

[a] Unconstrained parameters are shown with a 90% confidence interval. [b] Normalised amplitudes. [†] Fixed time constants. [‡] $\tau_3 \rightarrow \infty$ indicates a constant offset in the time-resolved curve.

The initial anisotropy value, also known as the fundamental anisotropy and denoted as r_0, is slightly lower than the expected maximum value of 0.4 for randomly oriented chromophores. There are several factors which can decrease the initial measured anisotropy. Firstly, any depolarisation occurring on a timescale faster than the time resolution of the detectors can result in a lower r_0. Furthermore, the measured anisotropy requires polarisers to be precisely in the vertical/horizontal orientations. Any misalignment would result in a decrease of the measured anisotropy. A slightly lower initial anisotropy than expected does not affect the anisotropy decay dynamics, which is what will be discussed in this chapter.

We have established that the main cause of anisotropy decay in the dilute TIPS-Pn in THF sample is due to the rotation of TIPS-Pn. However, for our NP samples, we assume TIPS-Pn molecules to be rigid in a NP. Thus, we expect rotation of the TIPS-Pn molecules to occur only via rotation of the NPs themselves. Using an estimate for the volume of the NP, we calculate an estimate for the rotational correlation time of a NP (refer to Appendix 5.6.3). The rotation of a NP is significantly slower than the timescale of our anisotropy measurement and so the rotation of TIPS-Pn molecules can be assumed to have negligible affect on the anisotropy of the NP samples.

We now consider the 1:100 NP sample, which also does not undergo SF (refer to Figure 5.1 and Table 5.1). The fluorescence anisotropy of this sample fits to a sum of two exponentials. One time constant is on the order of ∼50 ps while the long time constant is on the order of a few nanoseconds. We attribute these time constants to singlet migration, with the short time constant representing the fast migration of singlets due to a great selection of low energy chromophores to hop to at early times, and the long time constant to slow singlet migration to/from trap sites at late times.

We now focus on the fluorescence anisotropy of the 1:0 to 1:10 samples (refer to Figure 5.1). As the fluorescence anisotropy is calculated from detecting the fluorescence emission parallel and perpendicular to the exciton polarisation, when these emissions tend towards zero, the fluorescence anisotropy is lost in noise. Consequently, the fluorescence anisotropy is cut when the parallel scan reaches 10 % of its initial maximum peak intensity. However, the fluorescence anisotropy is still fairly noisy. As such, in

order to obtain a trend in the fluorescence anisotropy, the time constants were fixed to a short time constant, τ_1, intermediate time constant, τ_2, and a long time constant, τ_3. The fluorescence anisotropy of the 1:0, 1:1 and 1:3 samples was found to fit a single exponential ($\tau_1 = 1.5\,\text{ps}$) with a constant offset. Hence, this value of τ_1 was fixed for the remaining samples. For the 1:5, 1:7 and 1:10 samples, the fluorescence anisotropy is fairly constant between 5 and 100 ps. Therefore, these mass ratios required an additional intermediate time constant of $\sim$20 ps, to fit the fluorescence anisotropy data. Rather than a constant offset, the fluorescence anisotropy of these samples also showed a slight decay at longer times. Therefore, a τ_3 of 1500 ps was found to fit the 1:5, 1:7 and 1:10 samples. These results are summarised in Table 5.1. The amplitude of τ_1 decreases with increasing proportion of PMMA, while that of τ_3 increases.

Relative to the dilute TIPS-Pn in THF sample (and also the 1:100 NP sample), the initial anisotropy is lower for the NP samples. This is particularly evident for the NP samples with a low proportion of PMMA, corresponding to a shorter average intermolecular TIPS-Pn separation, and suggests that some migration happens extremely fast at early times (on the same order of magnitude as the instrument response time).

Tayebjee et al. studied TIPS-Pn NPs with two different morphologies.[55] Type I samples comprised of weakly coupled chromophores and were assigned to an amorphous distribution of TIPS-Pn molecules. Type II samples were comprised of strongly coupled chromophores and were assigned to a brickwork packing motif found in TIPS-Pn crystals. They expected the fluorescence anisotropy to decay when singlets migrate within amorphous regions or across grain boundaries and expected the anisotropy to be sustained when excitons migrate within the brickwork crystal structure. Rapid (<1 ps) initial fluorescence anisotropy decay in both NPs was observed and attributed to the depolarisation due to migration of singlets through amorphous region or over crystal grain boundaries in their NPs. The anisotropy decay was found to fit to two time constants, one sub-picosecond and one long-lived component, consistent with our neat 1:0 NP sample. Tayebjee et al. proposed that slow morphological evolution from a poorly coupled to highly coupled chromophore system results in formation of exciton traps.[55] These trap sites were suggested to be responsible for the long-lived component of the anisotropy. Similarly, we also attribute the long time constant to some amount of exciton trapping, due to the possible existence of isolated chromophores in our amorphous TIPS-Pn/PMMA NPs.

The amplitudes of the fits suggest faster depolarisation for shorter average intermolecular TIPS-Pn separations. Figure 5.2 displays this general trend. If singlet migration were to be the only cause of decay in the fluorescence anisotropy, these results would be consistent with faster singlet migration for shorter average interchromophore separations (refer to Equations 1.3 and 1.4 in Section 1.4.1). However, for the 1:5, 1:7 and 1:10 samples, the fluorescence anisotropy between 5 and 100 ps is fairly constant (and for the 1:5 sample increases slightly). Therefore, it can be concluded that singlet migration itself is insufficient to explain the fluorescence anisotropy data. Although rotational diffusion of the TIPS-Pn molecules has negligible effect on the fluorescence anisotropy decay, we have yet to consider the effect SF has on the fluorescence anisotropy.

To get a valid representative of the depolarisation of the singlet population, each singlet must fluoresce so it can be measured in the fluorescence anisotropy. Non-radiative decay, intersystem crossing (ISC) and SF are processes in which singlets are eliminated, and could therefore affect the anisotropy. We first note that ISC in TIPS-Pn

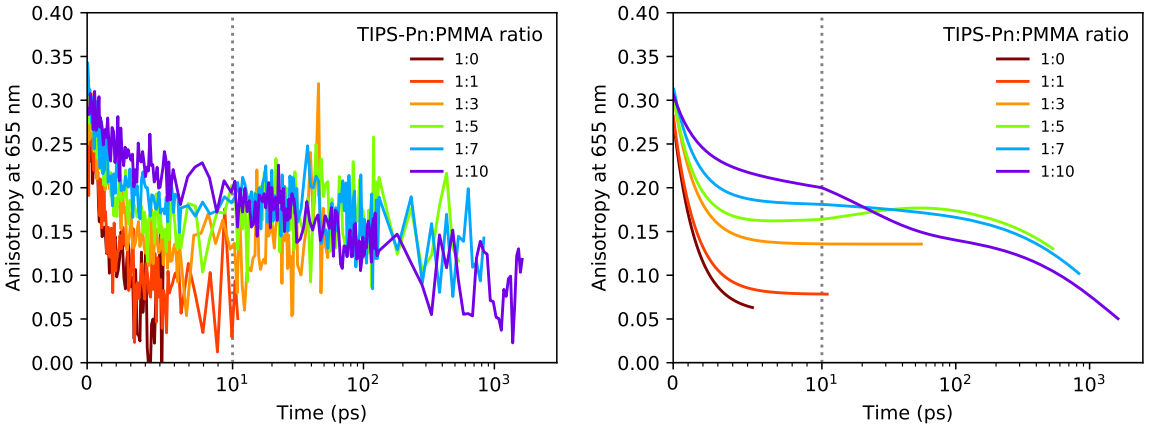

Figure 5.2: Experimental (left) and fitted (right) time-resolved fluorescence anisotropy for the TIPS-Pn/PMMA NPs. The dotted grey lines indicate a change from a linear to logarithmic scale.

occurs on a much longer timescale than our anisotropy experiments[52] and therefore ISC is expected to have minimal effect on the anisotropy decay kinetics presented in this thesis.

Now consider singlets being eliminated and this elimination being random (i.e. no preference of eliminating more/less correlated singlets). Then the $I_{\parallel}$ and $I_{\perp}$ signals would, on average, decrease by the same amount. The total intensity $I_{\mathrm{T}} = I_{\parallel} + 2I_{\perp}$ therefore also decreases, but the overall measured fluorescence anisotropy remains constant. Singlets decaying non-radiatively to the ground state results in random elimination of singlets and thus do not change the overall measured fluorescence anisotropy.

However, if there is a preference of eliminating singlets that are more (or less) correlated with the initial exciton polarisation, then this leaves a population of singlets with less (or more) correlation. This acts to decrease (or increase) the overall anisotropy. As SF eliminates singlets, we must consider if this elimination occurs randomly or selectively.

Let us first consider SF in a hypothetical system where chromophores are excited to their singlet state and can undergo SF to form two triplets, but cannot hop to another chromophore. Each singlet has the same probability of being excited to a SF site and thus the probability of SF is equal for any dipole moment orientated singlet. As such, SF eliminates singlets with a random polarisation. Therefore, if SF were to occur without any migration, SF would not influence the overall measured anisotropy.

We now consider diffusion-limited SF. This is the process in which a singlet first has to migrate to a specific site where it can undergo SF, termed "SF site". Every chromophore is equally likely to be part of a SF site. Therefore, given a specific time period, if a singlet has sampled more chromophores (achieved through faster migration), it has a higher probability of reaching a SF site. SF would thereby eliminate singlets which have undergone faster migration, giving a bias towards detecting the remaining singlets which have undergone slower migration. Furthermore, faster migration results in faster loss of correlation with the initial excitation polarisation. Consequently, diffusion-limited SF would selectively eliminate less correlated singlets, leaving behind a population of singlets with a higher correlation to the initial excitation polarisation and could act to increase the anisotropy.

We emphasise that the increase in anisotropy does not equate to a constant singlet

population becoming more correlated to the initial excitation polarisation. Instead, it is because the singlet population (i.e. I_T) is decreasing. This means $I_\parallel$ and $I_\perp$ are both still decreasing. However, the rate of decrease of $I_\perp$ is faster than the rate of decrease of $I_\parallel$ because the less correlated singlets are being eliminated by diffusion-limited SF. Therefore $I_\parallel - I_\perp$ increases, resulting in an increase in the overall anisotropy.

We propose that SF acts to effectively increase the fluorescence anisotropy, especially at intermediate times, between 5 and 100 ps (refer to Figure 5.1). Although this could also be interpreted as singlet migration having stopped at these times, it is more likely that the fluorescence anisotropy decay due to singlet migration is offset by the effective increase in anisotropy due to SF. Hence, we refrain from assigning the fluorescence emission depolarisation purely to singlet migration. We only note in this chapter that the general trend in the fluorescence anisotropy is faster depolarisation for shorter average intermolecular TIPS-Pn separations. The different contributions (singlet migration and SF) affecting the fluorescence anisotropy need to be separated and this will be the subject of the next chapter.

5.2 Visible Transient Absorption Anisotropy

Time-dependent TA anisotropy is defined as

$$r(t,\lambda) = \frac{\Delta A_\parallel(t,\lambda) - \Delta A_\perp(t,\lambda)}{\Delta A_\parallel(t,\lambda) + 2\Delta A_\perp(t,\lambda)}, \tag{5.2}$$

where $\Delta A_\parallel(t,\lambda)$ and $\Delta A_\perp(t,\lambda)$ are the change in absorbances measured when the probe and pump are polarised parallel and perpendicular to each other, respectively.[104,106–108]

We note that the rotation of the excitation polarisation from vertical to horizontal caused slight changes in power incident on the sample. This power difference was measured and the perpendicular intensity scans were multiplied by 0.975 before the TA anisotropy was calculated using Equation 5.2.

Time-resolved fluorescence anisotropy gives a measure of depolarisation of singlets by monitoring the fluorescence emission at one specific wavelength. However, TA anisotropy monitors the polarisation of the change in absorbance (ΔA) for a range of wavelengths, λ, over time. The absorption spectra of excited-state species are distinct, and if ΔA at a specific λ can be assigned to just one excited-state species, then the TA anisotropy at that λ is a representation of the depolarisation of that species. As such, the TA anisotropy offers the opportunity to monitor the migration of different excited-state species (e.g. triplets).

However, in reality and in the case of our TIPS-Pn/PMMA NPs, ΔA at most wavelengths has contributions from the GSB, stimulated emission (SE) and excited-state absorption (ESA), and there is typically a lack of correspondence between λ and any one excited-state species. The TA anisotropy at a given wavelength, λ, can be described as a sum of the different contributions,

$$r(t) = f_{\mathrm{GSB}}(t)r_{\mathrm{GSB}}(t) + f_{\mathrm{SE}}(t)r_{\mathrm{SE}}(t) + f_{\mathrm{ESA}}(t)r_{\mathrm{ESA}}(t), \tag{5.3}$$

where r_{GSB}, r_{SE} and r_{ESA} are the weighted average anisotropy of the GSB, SE and ESA components in the TA signal, respectively, and f_{GSB}, f_{SE} and f_{ESA} are the fraction of the GSB, SE and ESA contributions to the TA signal at a certain λ, respectively.[120,121]

The TA anisotropy becomes more complicated to analyse if time-dependent spectral shifts of absorption/emission bands are involved. These can arise from vibronic relaxation and/or intra- and intermolecular reorganisation processes (e.g. solvation). For example, Min et al. noticed that a red-shift in the excited state SE spectrum decreases the contribution of the excited state SE component in the overall TA signal and thus a rise in the anisotropy was observed.[120]

In the case of our TIPS-Pn/PMMA NPs, only an insignificant amount of spectral shift was observed. Additionally, the TA anisotropy kinetics presented at a single wavelength were almost identical to those when averaged over a wavelength range (5 nm either side of the reported wavelength), confirming negligible effect of any spectral shifts that may be present.

The TIPS-Pn/PMMA NP samples were excited with polarised 590 nm light to promote TIPS-Pn from the S_0 to S_1 state, as mentioned in Section 5.1. ΔA from the TIPS-Pn/PMMA NPs was detected parallel and perpendicular to the excitation polarisation, as explained in Section 2.3.5. The TA anisotropy was then calculated as a function of time, t, and wavelength, λ. The anisotropy ranges from -0.2 to 0.4 as explained previously. The factors causing depolarisation include those discussed for fluorescence anisotropy.

We now present the anisotropy data of the TIPS-Pn/PMMA NP samples at two different wavelengths, 650 nm and 508 nm. We note that at ∼710 nm there is a large contribution from SE and therefore this would be an interesting region to explore the SE anisotropy decay. However, the signal strength at this wavelength was too weak to obtain meaningful anisotropy results.

Again, we note that ISC in TIPS-Pn occurs on a much longer timescale than our anisotropy experiments[52] and therefore ISC is expected to have minimal effect on the anisotropy decay kinetics presented in this thesis.

5.2.1 Trends in the Transient Absorption Anisotropy at 650 nm

The TA anisotropy of the TIPS-Pn/PMMA NP samples at 650 nm is presented in Figure 5.3. At 650 nm ΔA has contributions from GSB, SE and ESA. The experimental data are fit to a sum of exponentials, with parameters given in Table 5.2. Appendix 5.6.2 shows the individual parallel and perpendicular scans for each sample.

We first focus on the TIPS-Pn in THF sample. As discussed earlier, this sample neither undergoes SF nor a significant amount of singlet migration. Accordingly, only singlets should be present and the depolarisation should be only due to the rotation of TIPS-Pn molecules in solution. The TA anisotropy of the this sample at 650 nm can be fit to a single exponential of (118 ± 2) ps, consistent with the fluorescence anisotropy. Our results are also consistent with those of Pensack et al., who measured an anisotropy decay time constant of ∼150 ps for the GSB feature of 6,13-bis(triisobutylsilylethynyl) pentacene (TIBS-Pn) in THF, with observations consistent with re-orientational dynamics of chromophores in a dilute solution.[54] As was the case for the fluorescence anisotropy, the initial anisotropy value is below the maximum of 0.4 for reasons discussed previously.

We now focus on the 1:100 NP sample, in which SF is largely absent. The TA anisotropy of this sample fits to a sum of two exponentials. The short time constant is on the order of ∼60 ps while the long time constant is on the order of a few nanoseconds. This result is consistent with what was observed from the fluorescence anisotropy, where

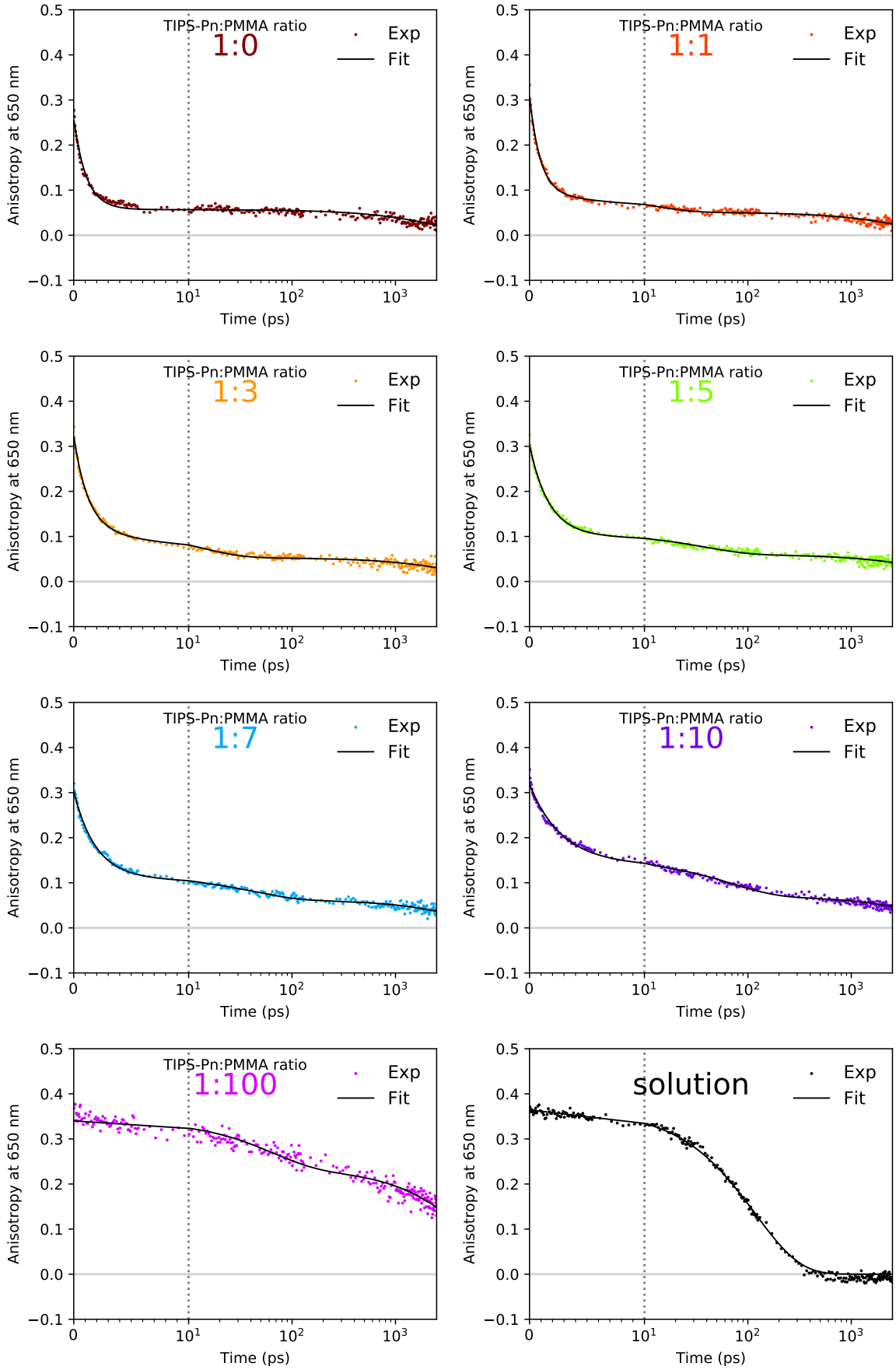

Figure 5.3: Experimental TA anisotropy at 650 nm for all TIPS-Pn/PMMA NPs and TIPS-Pn in THF. All data were fit to a sum of exponentials with parameters given in Table 5.2. The dotted grey lines indicate a change from a linear to logarithmic scale.

Table 5.2: Fitting parameters for the TA anisotropy data at 650 nm of TIPS-Pn/PMMA NPs and TIPS-Pn in THF.[a]

Sample	A_1 [b]	τ_1 (ps)	A_2	τ_2 (ps)	A_3	τ_3 (ps)
1:0	0.78±0.02	1.1±0.07	-	-	0.220±0.004	2700±200
1:1	0.69±0.03	0.93±0.08	0.14±0.03	11±3	0.165±0.005	3500±300
1:3	0.64±0.03	1.3±0.1	0.20±0.03	12±3	0.163±0.005	4600±500
1:5	0.65±0.02	1.7±0.1	0.15±0.02	38±13	0.198±0.008	7200±1500
1:7	0.62±0.02	1.9±0.1	0.18±0.02	41±10	0.206±0.008	4800±600
1:10	0.53±0.01	2.7±0.2	0.25±0.01	69±9	0.219±0.008	6500±1000
1:100	0.31±0.02	63±12	-	-	0.69±0.02	5400±500
solution	1.000±0.004	118±2	-	-	-	-

[a] Unconstrained parameters are shown with a 90% confidence interval. [b] Normalised amplitudes.

we attributed the time constants to singlet migration.

The anisotropy decay of the 1:0 sample can be fit to two exponentials, while those of the 1:1 to 1:10 samples were fit to three time components. These results are summarised in Table 5.2. The short time constant, τ_1, is ∼1 ps and it increases as the proportion of PMMA is increased, while the corresponding amplitude decreases. The intermediate time constant, τ_2, also increases slightly as the proportion of PMMA is increased. The results show that the TA anisotropy at 650 nm decays faster for NP samples with a shorter average intermolecular TIPS-Pn separation, as highlighted in Figure 5.4. The

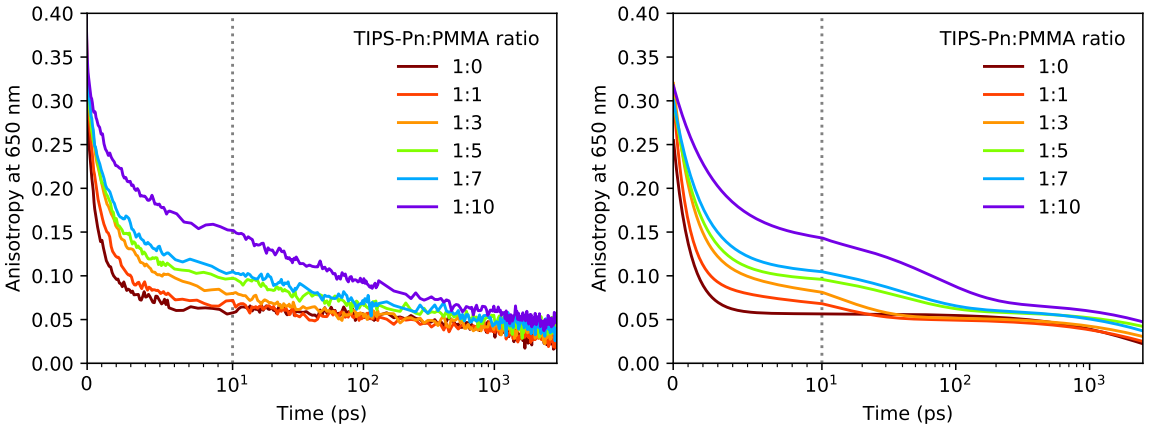

Figure 5.4: Experimental (left) and fitted (right) TA anisotropy at 650 nm for TIPS-Pn/PMMA NPs. The dotted grey lines indicate a change from a linear to logarithmic scale.

long time constant, τ_3, is on the order of nanoseconds. Because this time constant is significantly longer than the timescale of these experiments, no concrete conclusions can be made. It is possible that this time constant represents slow singlet or triplet migration.

Pensack et al. measured the TA anisotropy decay of the GSB feature of TIPS-Pn NPs and other NPs of pentacene derivatives. The GSB anisotropy decay of their TIPS-Pn NPs seeming to be consistent with our neat 1:0 NP sample. The aim of their

anisotropy measurements was purely to differentiate between the morphology of their NPs. NPs displaying a rapid anisotropy decay were explained to have little long-range order. NPs with a slower anisotropy decay, however, have extensive long-range solid-state order, as energy migration in an ordered system is expected to involve transition dipole moments that are aligned.[54]

Although significant evidence suggests our NPs to be amorphous, we cannot conclude that the TIPS-Pn molecules are evenly dispersed within our NPs. The idea that NPs consist of amorphous clusters of TIPS-Pn, was mentioned in Section 3.2. As singlet migration occurs through a Förster resonance energy transfer (FRET) mechanism, the singlet migration rate depends on the distance between chromophores (refer to Equations 1.3 and 1.4 in Section 1.4.1). As clustering results in a larger proportion of neighbours with a shorter distance from the initially excited chromophore, an increased singlet migration rate, and thus a faster initial anisotropy decay, would be expected compared to a random distribution of TIPS-Pn molecules. To test whether TIPS-Pn molecules are clustered in our NPs, the fluorescence anisotropy dynamics of random and clustered distributions need to be compared. This will be the subject of Chapter 6.

5.2.2 Trends in the Transient Absorption Anisotropy at 508 nm

The TA anisotropy of the TIPS-Pn/PMMA NP samples at 508 nm is presented in Figure 5.5. These data were also fit to a sum of exponentials, with parameters given in Table 5.3. At 508 nm ΔA is mainly due to ESA, namely from singlet and triplet absorptions.

Table 5.3: Fitting parameters for the TA anisotropy data at 508 nm of TIPS-Pn/PMMA NPs and TIPS-Pn in THF.[a]

Sample	A_1 [b]	τ_1 (ps)	A_2	τ_2 (ps)
1:0	-1.00±0.09	0.51±0.08	-	-
1:1	-1.00±0.05	0.94±0.09	-	-
1:3	-0.90±0.05	1.6±0.2	-0.10±0.05	31±28
1:5	-0.8±0.1	1.0±0.2	-0.2±0.1	6±3
1:7	-0.77±0.05	1.4±0.3	-0.23±0.05	49±28
1:10	-0.72±0.02	1.7±0.1	-0.28±0.01	74±8
1:100	-0.33±0.04	5±2	-0.67±0.02	2900±200
solution	-1.000±0.005	143±3	-	-

[a] Unconstrained parameters are shown with a 90% confidence interval. [b] Normalised amplitudes.

First, we note the TA anisotropy at 508 nm has a negative amplitude. The negative anisotropy is due to ΔA at 508 nm consisting of excited-state contributions from both singlet and triplet excitons (refer to Section 4.2.1). The transition dipole moments of the singlet and triplet ESA ($S_1 \rightarrow S_n$ and $T_1 \rightarrow T_n$) are both perpendicular to the $S_0 \rightarrow S_1$ transition,[33,38,61] as illustrated in Figure 5.6. This means that singlet and triplet ESA result in a 90° rotation in the detected polarisation relative to the initial excitation polarisation. Therefore, the initial anisotropy value would be -0.2 (refer to Section 5.1),

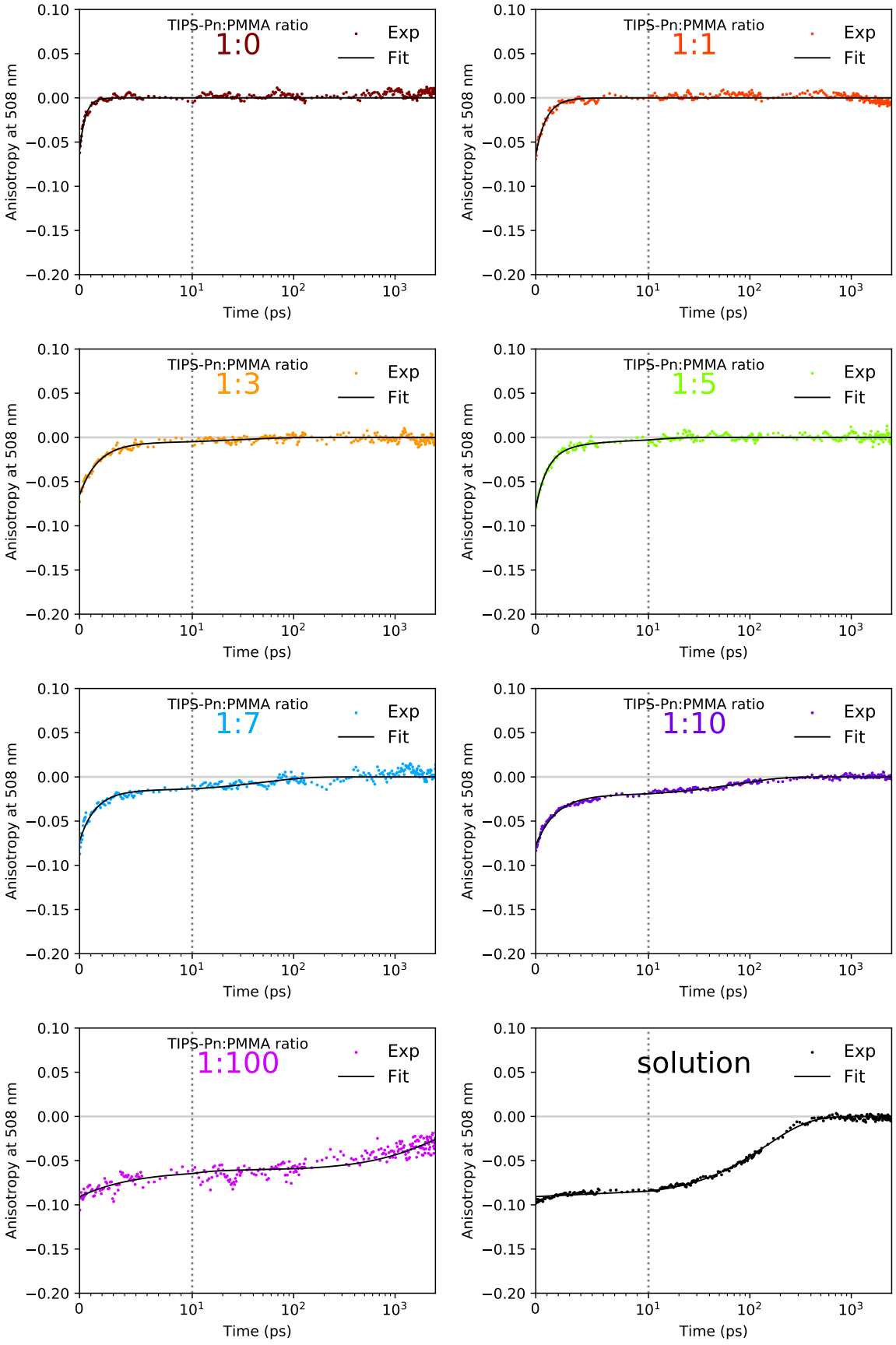

Figure 5.5: Experimental TA anisotropy at 508 nm for all TIPS-Pn/PMMA NPs and TIPS-Pn in THF. All data were fit to a sum of exponentials with parameters given in Table 5.3. The dotted grey lines indicate a change from a linear to logarithmic scale.

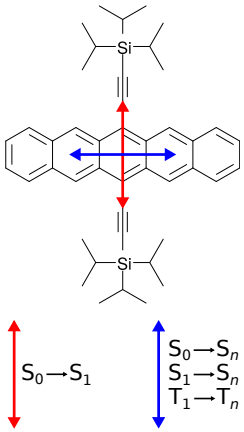

Figure 5.6: The various transition dipole moment directions of TIPS-Pn.[33,38,61]

if there was no loss in polarisation during the initial excitation and the detection of the TA anisotropy at this wavelength. However, the direction of the transition dipole moment of the ESA may change due to vibronic coupling to higher states that changes as vibrational and spin relaxation occurs.[121] This would then result in excited-state transition dipole moments not being exactly perpendicular to the $S_0 \rightarrow S_1$ transition, and thus result in a lower (in magnitude) initial anisotropy than expected. However, as stated previously, this should not affect the anisotropy decay dynamics.

The negative TA anisotropy observed in our NPs at 508 nm is consistent with a previous study on pentacene. McDonough et al. performed the first TA measurements on pentacene,[47] observing a negative anisotropy at 507 nm and 545 nm. McDonough et al. argued that a negative anisotropy is consistent with pumping the $S_0 \rightarrow S_1$ state and probing the triplet $T_1 \rightarrow T_3$ transition, as these dipole moments are perpendicular.[47] They therefore use these anisotropy results to assign the 507 nm and 545 nm absorptions to the triplet transition. However, since the $S_1 \rightarrow S_n$ transition is also perpendicular to the $S_0 \rightarrow S_1$ transition,[33,38,61] a negative anisotropy alone is not a valid basis on which to assign a transition to be purely due to triplets. Furthermore, the poor quality anisotropy data did not allow for any other analysis apart from the magnitude of the anisotropy.[47]

We now comment on the trends of the TA anisotropy at 508 nm. The 1:0 and 1:1 samples can be fit with a single exponential, while the rest are fit with two exponentials. These results are summarised in Table 5.3. The short time constant, τ_1, is $\sim$1 ps and it increases as the proportion of PMMA is increased, while the corresponding amplitude decreases. Correspondingly, the amplitude of the longer time constant, τ_2, increases. The results show that the TA anisotropy at 508 nm decays faster for NP samples with a shorter average intermolecular TIPS-Pn separation, as highlighted in Figure 5.7.

Unlike the fluorescence anisotropy and the TA anisotropy at 650 nm, the TA anisotropy at 508 nm decays to zero within the timescale of the experiment. This is due to the lower initial anisotropy amplitude at 508 nm, corresponding to an already slightly depolarised system, and so the time taken to reach an anisotropy value of zero (corresponding to a completely depolarised system) is faster. An anisotropy value of zero means ΔA has lost all correlation with the initial excitation polarisation. Consequently, no long time component exists, and any further depolarisation (e.g. from slow singlet or triplet migration) would not be observed at this wavelength.

The τ_1 value is slightly lower than that at 650 nm for a given NP sample. It is

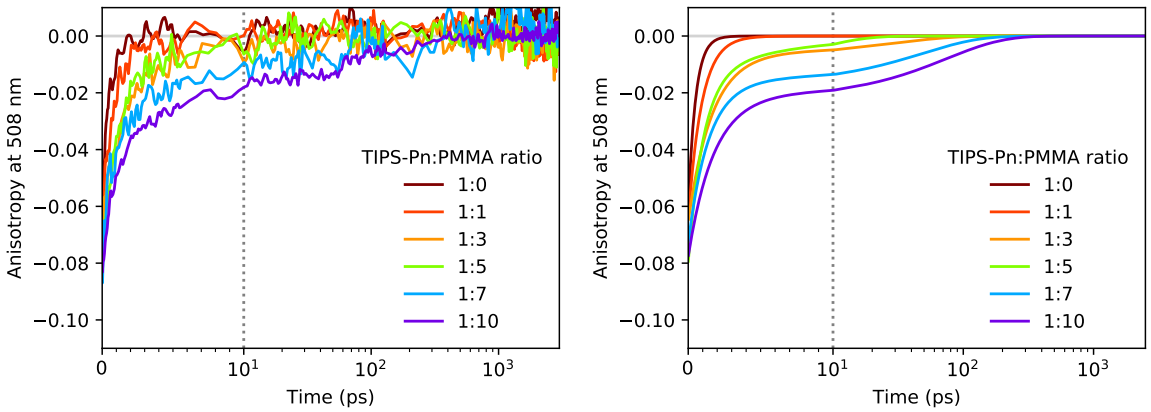

Figure 5.7: Experimental (left) and fitted (right) TA anisotropy at 508 nm for TIPS-Pn/PMMA NPs. The dotted grey lines indicate a change from a linear to logarithmic scale.

evident that the ΔA depolarisation rate is different at these two wavelengths (650 nm versus 508 nm). This is due to different components affecting these wavelengths, each causing a different contribution to the depolarisation. In an attempt to obtain TA anisotropy decays associated with a single species only, we turn towards measurements in the near-infrared (NIR) region, where the singlet and triplet features are more clearly separated.

5.3 NIR Transient Absorption Anisotropy

The overlapping contributions from the GSB, SE and ESA in the visible spectral region have been discussed. In the NIR region there are no influences from the GSB or SE. Therefore, analysis of the spectrum is relatively straightforward. From the magic-angle TA data presented in Section 4.2.2, we assigned the wavelength at 1350 nm to singlet absorption, and the wavelength at 990 nm to have mainly a triplet (but also some singlet) contribution. Obtaining NIR TA anisotropy data may therefore make analysis of exciton migration straightforward as the TA anisotropy at 1350 nm and 990 nm is a representation of the singlet and triplet depolarisation, respectively.

Figure 5.8 displays the anisotropy decay of the fluorescence (at 655 nm) and TA (at 990 nm and 1350 nm) for $\sim 10^{-4}$ M TIPS-Pn in THF. All data were fit to a single exponential, with parameters given in Table 5.4. The same information is displayed for the 1:10 sample in Figure 5.9 and Table 5.5, where the data are fit to a sum of two exponentials. The short time constant, τ_1, for the TA anisotropy at 1350 nm fits well when fixed to τ_1 of the fluorescence anisotropy data. The time constants and amplitudes of the fluorescence anisotropy and TA anisotropy at 1350 nm, are the same, within error, for each sample. This suggests that there are no major contributions from other species at 1350 nm, confirming that ΔA at 1350 nm is mainly due to singlets.

As mentioned previously, the ΔA at 990 nm is mostly due to triplets, but a small proportion of singlets also contribute to this wavelength. The TA anisotropy of the TIPS-Pn in THF sample at 990 nm showed similar kinetics to that at 1350 nm. As this sample does not undergo SF, the 990 nm TA anisotropy decay is also a representation of singlet depolarisation. However, the TA anisotropy at 990 nm is significantly lower

in quality than that at 1350 nm due to a lower ΔA signal amplitude. For the 1:10 sample, an attempt to analyse the TA anisotropy kinetics at 990 nm was made in order to obtain the anisotropy decay due to triplets. However, nearly all correlation is lost at this wavelength at early times, and so triplet migration cannot be analysed using this signal.

The loss of polarisation anisotropy at 990 nm can be explained as follows. Fast

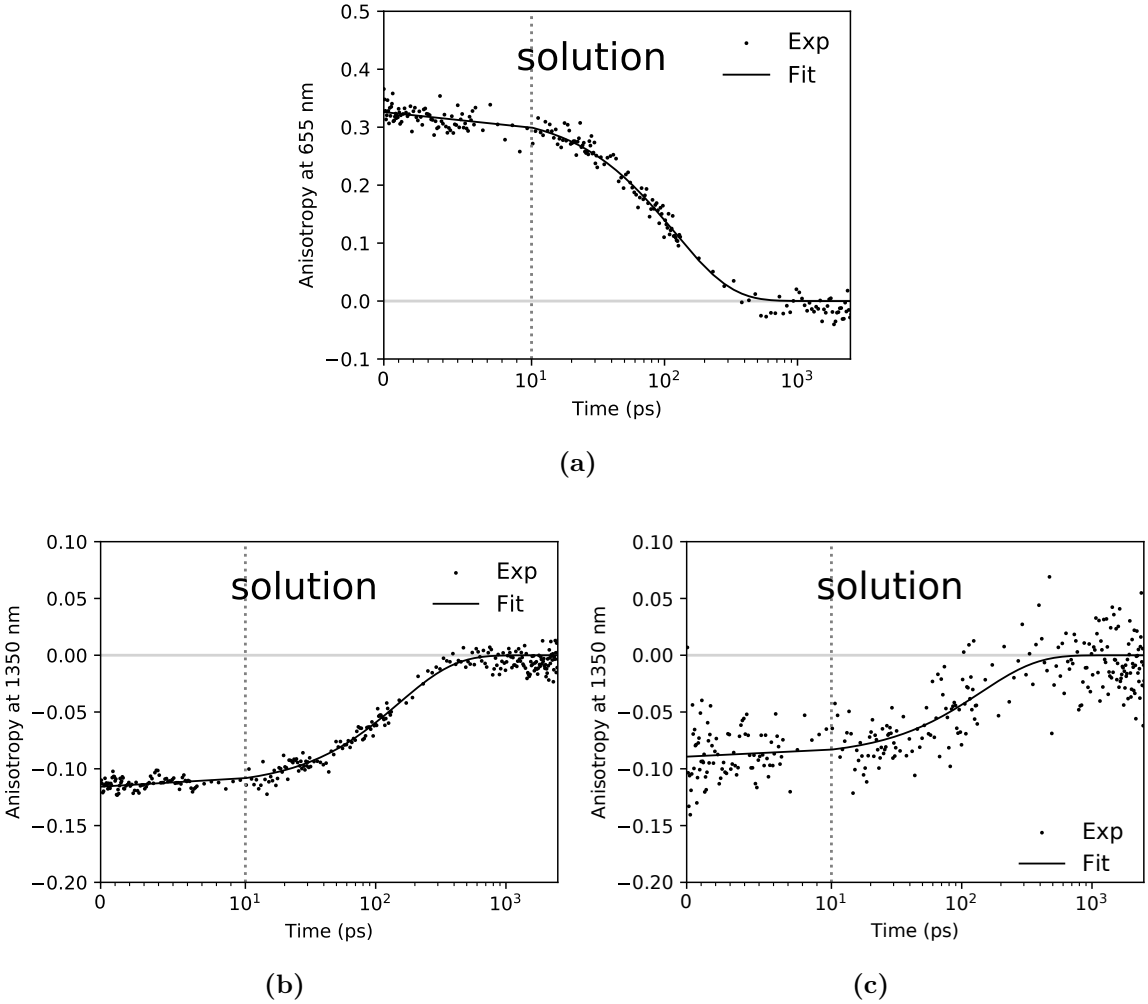

Figure 5.8: Experimental and fitted **(a)** fluorescence anisotropy, **(b)** TA anisotropy at 1350 nm and **(c)** TA anisotropy at 990 nm, for $\sim 10^{-4}$ M TIPS-Pn in THF. The dotted grey lines indicate a change from a linear to logarithmic scale.

Table 5.4: Fitting parameters for the fluorescence anisotropy and TA anisotropy data at 1350 nm of $\sim 10^{-4}$ M TIPS-Pn in THF.[a]

Sample	A_1 [b]	τ_1
Solution (Fluorescence)	1.000±0.008	118±4
Solution (TA at 1350 nm)	-1.00±0.01	150±7
Solution (TA at 990 nm)	-1.00±0.05	140±32

[a] Unconstrained parameters are shown with a 90% confidence interval. [b] Normalised amplitudes.

singlet migration to SF sites results in depolarisation, and then SF results in two triplets. Only one of these triplets (the one previously in the S_1 state) may possibly still display a slight correlation to the initial excitation, while the other (previously a ground-state molecule), would show no correlation assuming SF has no orientational dependence. The combination of triplets resulting from already depolarised singlets and one of the formed triplets showing no correlation, results in a close to zero anisotropy at early times.

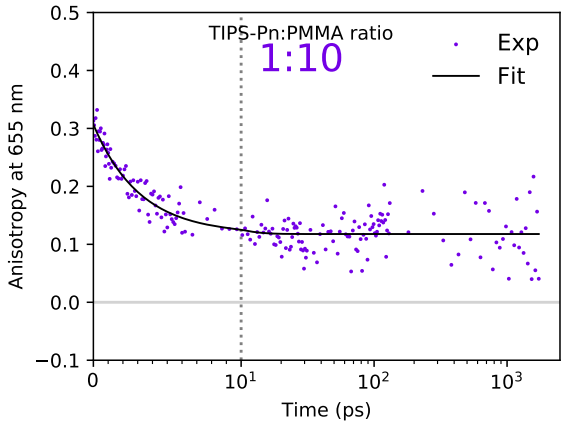

(a)

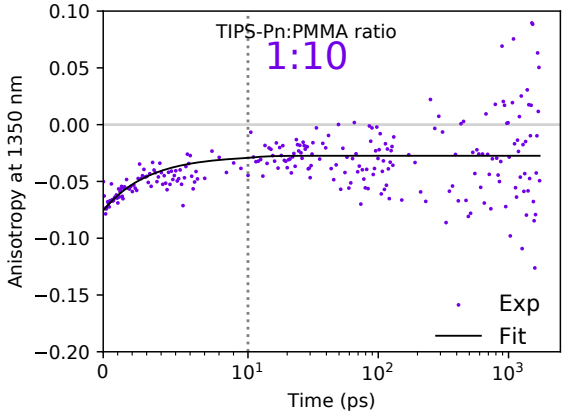

(b)

Figure 5.9: Experimental and fitted **(a)** fluorescence anisotropy and **(b)** TA anisotropy at 1350 nm, for the 1:10 TIPS-Pn:PMMA NPs. The dotted grey lines indicate a change from a linear to logarithmic scale.

Table 5.5: Fitting parameters for the fluorescence anisotropy and TA anisotropy data at 1350 nm of 1:10 TIPS-Pn:PMMA NPs.[a]

Sample	A_1 [b]	τ_1 (ps)	A_2	τ_2 [‡] (ps)
1:10 (Fluorescence)	0.62±0.05	3.1±0.5	0.39±0.01	∞
1:10 (TA at 1350 nm)	-0.6±0.2	3.1[†]	-0.36±05	∞

[a] Unconstrained parameters are shown with a 90% confidence interval. [b] Normalised amplitudes. [†] Fixed time constant. [‡] $\tau_2 \rightarrow \infty$ indicates a constant offset in the time-resolved curve.

5.4 Motivation for the Monte Carlo Simulation

The fluorescence and TA anisotropy both decay faster for NP samples with a shorter average intermolecular TIPS-Pn separation. The fluorescence anisotropy is a representation of the S_1 state and the anisotropy decay can result from rotational diffusion (by rotation of the NPs) and singlet migration. It has already been established that the rotational diffusion of the NPs has a minor effect on the decay of the fluorescence anisotropy. However, we hinted at the presence of a process that slows down (or effectively increases) the fluorescence anisotropy decay at intermediate times. We hypothesised that this may be due to selective elimination of singlets due to diffusion-limited SF. Therefore, these two processes (singlet migration and diffusion-limited SF) need to be separated.

To investigate migration of other species (e.g. triplets), we turned to TA anisotropy. The advantage of TA anisotropy is that the change in polarisation of ΔA is obtained for a range of wavelengths, λ. If a certain wavelength corresponds to the ESA of only one species, then TA anisotropy offers the opportunity to monitor the migration of that species. This is, however, not the case as the TA anisotropy decay at a certain wavelength has influences from the GSB, SE and ESA which need to be separated before analysis (refer to Equation 5.3). Even at 508 nm, which has minor contributions from the GSB or SE, the ESA is due to both singlets and triplets. In addition, although there is no strong evidence of SF affecting the TA anisotropy, we cannot be certain unless the effect of SF is separated from all other components contributing to the anisotropy.

For these reasons, it is necessary to provide a means in which to separate the different components contributing to the anisotropy decay, in order to obtain useful information on exciton migration and SF in these NPs. Therefore, a Monte Carlo (MC) simulation was developed to model the excitation, singlet migration and SF of TIPS-Pn in the different NP environments. The results of this MC simulation will be presented in the following chapter.

5.5 Conclusions

In this chapter, we presented time-resolved fluorescence and TA anisotropy of our TIPS-Pn/PMMA NPs. It has been established that the fluorescence anisotropy decays faster for NP samples with a shorter average intermolecular TIPS-Pn separation. We also hypothesise that SF may be affecting the fluorescence anisotropy, due to an effective halt in anisotropy decay between 5 and 100 ps. The TA anisotropy (at both at 650 nm and 508 nm) decays faster for the NP samples with a shorter average intermolecular TIPS-Pn separation. The TA anisotropy at 1350 nm decay kinetics reflect those of the fluorescence anisotropy, confirming that ΔA is mostly due to singlet ESA at 1350 nm. The TA anisotropy at 990 nm, a wavelength corresponding to mostly triplet ESA, cannot be analysed for the TIPS-Pn/PMMA NP samples, as the initial anisotropy at this wavelength is almost zero. To analyse exciton migration, the different components contributing to the anisotropy decay need to be separated. This work will be discussed in the next chapter.

5.6 Appendices

5.6.1 Parallel and Perpendicular Fluorescence Traces

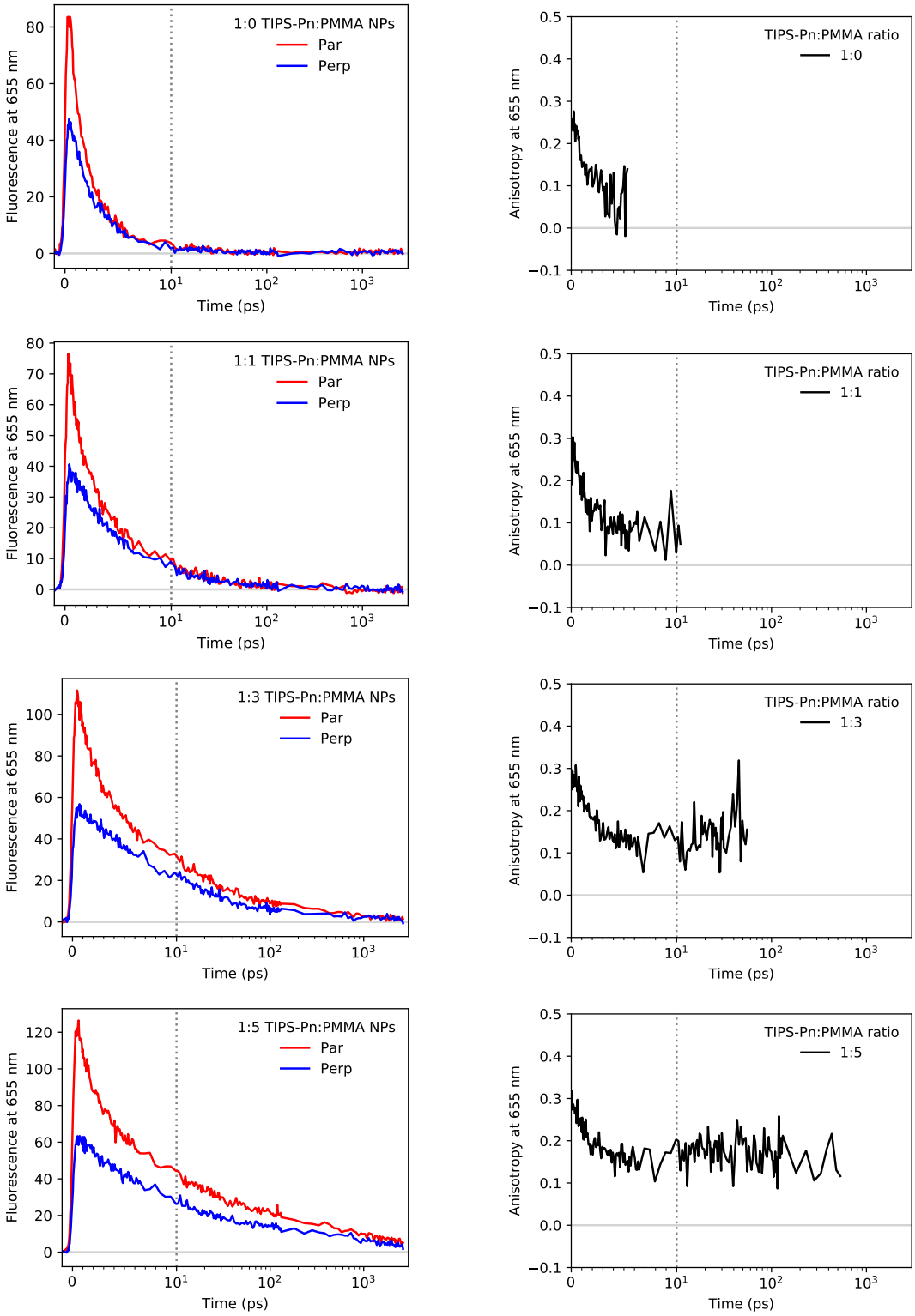

Figure 5.10: Fluorescence emission detected parallel and perpendicular to the excitation polarisation, and the corresponding anisotropy for the 1:0 to 1:5 TIPS-Pn:PMMA NPs.

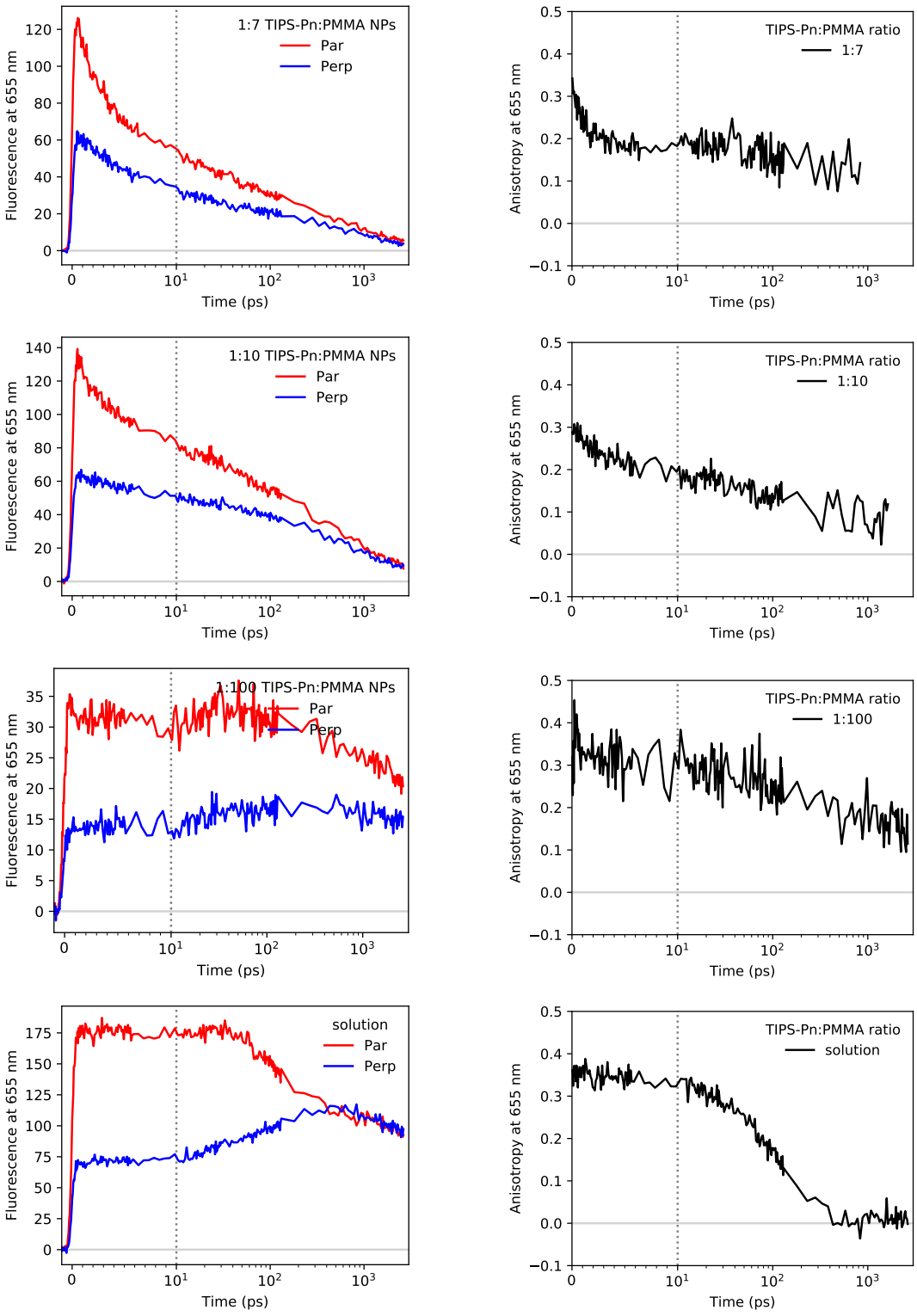

Figure 5.11: Fluorescence emission detected parallel and perpendicular to the excitation polarisation, and the corresponding anisotropy for the 1:7 to 1:100 TIPS-Pn:PMMA NPs as well as $\sim 10^{-4}$ M TIPS-Pn in THF.

5.6.2 Parallel and Perpendicular Transient Absorption Traces

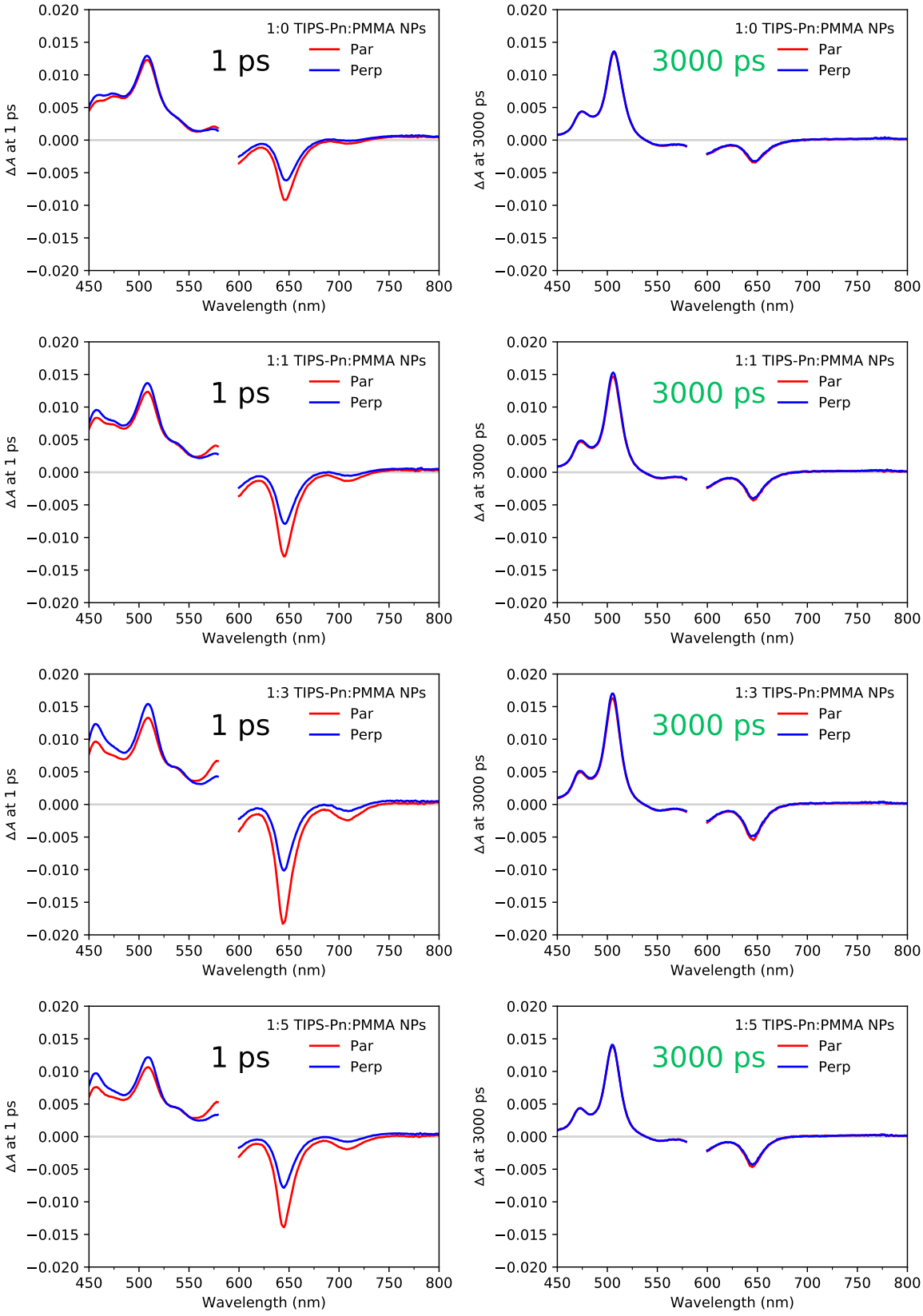

Figure 5.12: ΔA detected parallel and perpendicular to the excitation polarisation for the 1:0 to 1:5 TIPS-Pn:PMMA NPs.

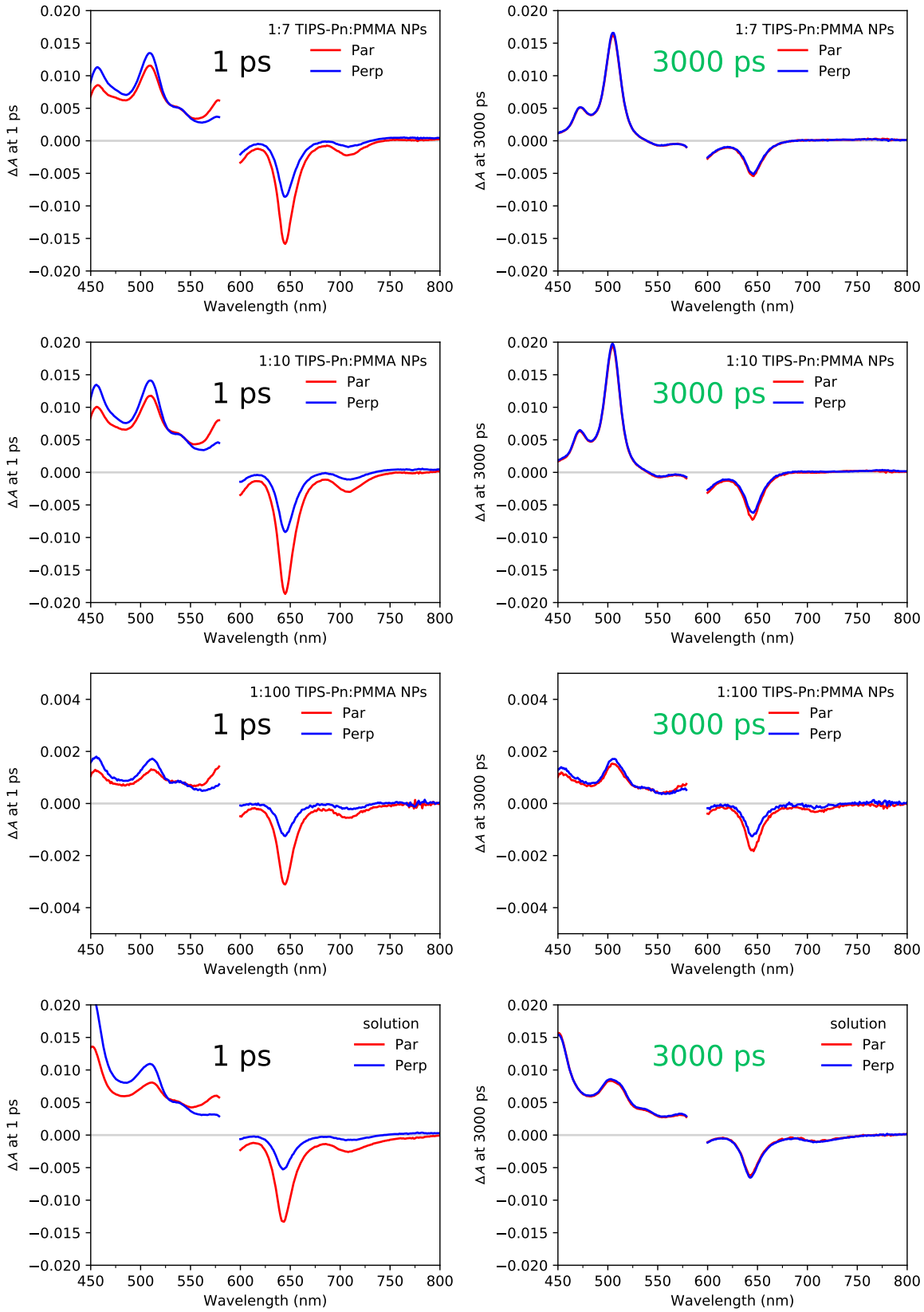

Figure 5.13: ΔA detected parallel and perpendicular to the excitation polarisation for the 1:7 to 1:100 TIPS-Pn:PMMA NPs as well as $\sim 10^{-4}$ M TIPS-Pn in THF.

5.6.3 Estimation of Rotational Correlation Time

The rotational correlation time, θ, of a sphere is the average time for it to rotate one radian, and is given by[91]

$$\theta = \frac{\eta V}{RT} = \frac{\eta(\frac{4}{3}\pi r^3)}{RT}, \tag{5.4}$$

where η is the viscosity, T is temperature, R is the gas constant, V is the volume of the rotating unit and r is the radius of the rotating unit.

TIPS-Pn molecules

TIPS-Pn molecules can be considered to be around 1.2 nm long (refer to Figure 2.5 in Section 2.4.1.3). Using the viscosity of THF, 4.8×10^{-4} Pa s, we estimate the rotational correlation time of TIPS-Pn molecules to be

$$\begin{aligned}\theta &= \frac{4.8 \times 10^{-4}\,\mathrm{Pa\,s}\ (\frac{4}{3}\pi(0.6 \times 10^{-9}\,\mathrm{m})^3)}{8.314\,\mathrm{m^3\,Pa\,K^{-1}\,mol^{-1}} \times 294\,\mathrm{K}} \times 6.022 \times 10^{23}\,\mathrm{mol^{-1}} \\ &\approx 108\,\mathrm{ps}\end{aligned}$$

Nanoparticles

The NPs have been found to have a diameter of ∼40 nm.[115] Using the viscosity of water, 8.90×10^{-4} Pa s, we estimate the rotational correlation time of our NPs to be

$$\begin{aligned}\theta &= \frac{8.90 \times 10^{-4}\,\mathrm{Pa\,s}\ (\frac{4}{3}\pi(20 \times 10^{-9}\,\mathrm{m})^3)}{8.314\,\mathrm{m^3\,Pa\,K^{-1}\,mol^{-1}} \times 294\,\mathrm{K}} \times 6.022 \times 10^{23}\,\mathrm{mol^{-1}} \\ &\approx 7\,\mu\mathrm{s}\end{aligned}$$

This is significantly larger than the 3 nanosecond time window of the anisotropy measurements, so the rotation of TIPS-Pn molecules can be assumed to have negligible effect on the anisotropy of the NP samples.

CHAPTER 6
Monte Carlo Simulation of TIPS-Pn/PMMA Nanoparticles

In this chapter we present results from the Monte Carlo (MC) simulation of our 6,13-bis(triisopropylsilylethynyl) pentacene (TIPS-Pn)/poly(methyl methacrylate) (PMMA) nanoparticle (NP) systems. Simulated steady-state absorption and emission spectra are presented. The mean squared displacement (MSD) plots give insight into how far a singlet diffuses within the NP systems. Simulated time-resolved fluorescence and anisotropy traces were obtained by modifying the amount of singlet fission (SF) sites and SF rate. With the SF model used in our MC simulation, the experimental fluorescence and anisotropy data could only be reproduced by assuming a degree of clustering of TIPS-Pn within the NP systems. The MC simulation allows for separation of the effects of singlet migration and SF on the time-resolved fluorescence anisotropy.

6.1 Monte Carlo Simulation Structure

The MC simulation was based on a previous simulation by Tapping et al. [105] and modified by Jessica M. de la Perrelle to simulate our TIPS-Pn/PMMA NP systems. The MC simulation will be briefly described here. Full details can be found in Section 2.4.

The positions and transition dipole moments of the TIPS-Pn molecules were extracted from various timesteps of a simple molecular dynamics (MD) simulation to obtain a random and clustered distribution of chromophores (refer to Section 2.4.1). For each NP sample, the number of TIPS-Pn molecules in the cubic box of length 20 nm was determined by the TIPS-Pn:PMMA mass ratio. The energies of the TIPS-Pn molecules were generated from a normal distribution with a mean E_0 and standard deviation E_α.

The MC simulation then works as follows:

1. A randomly chosen TIPS-Pn molecule is excited to its singlet state.

2. The singlet can then hop to a neighbouring TIPS-Pn, undergo SF or decay to the ground state. The process chosen is the one with the smallest $\Delta t = -\frac{\ln(x)}{k}$, where k are the rate constants of singlet hopping, SF or decay, and x is a random variate over [0,1] chosen for each k.

3. If a hop is chosen, the total time is incremented by that Δt. The acceptor of migration is excited and step 2) is repeated for the new TIPS-Pn molecule.

4. If singlet decay or SF is chosen, energy and time histograms are populated and a new TIPS-Pn molecule is excited. Steps 1) – 4) are repeated from 1×10^5 excitations.

Once simulation trajectories are run, simulated results can be compared to experimental data, as highlighted in Section 2.4.5. Basically, by selection of a wavelength from the two-dimensional (2D) simulated fluorescence and anisotropy histograms, fluorescence and anisotropy kinetics can be generated to compare to the experimental data.

The singlet decay rate constant, k_d, is taken to be $\frac{1}{12}\mathrm{ns}^{-1}$ from the intrinsic lifetime of singlets.[57] Singlet migration occurs through a Förster resonance energy transfer (FRET) process in our MC simulation. The singlet migration rate constant, k_DA, is given in Section 1.4. The rate of singlet migration depends on the distance between the donor and acceptor molecules, the alignment of their transition dipoles, and their spectral overlap.

A simple model for SF is employed in our MC simulation, as the microscopic details of SF are not yet fully understood.[112] We assume SF occurs with a rate k_SF if a singlet molecule has a ground-state molecule within a distance of r_SF. Mathematically, we describe the rate of SF by

$$k_\mathrm{SF}^{D,A} = k_\mathrm{SF}\Theta(r_\mathrm{SF} - r^{D,A}), \tag{6.1}$$

where D and A denote the "donor" singlet molecule and "acceptor" ground-state molecule, respectively, $r^{D,A}$ is the distance between those two molecules and Θ is the Heaviside step function. The "SF radius", r_SF, is defined as the maximum distance between a donor and acceptor in order for SF to occur. In this model, $k_\mathrm{SF}^{D,A} = k_\mathrm{SF}$ if $r^{D,A} \leq r_\mathrm{SF}$ and $k_\mathrm{SF}^{D,A} = 0$ if $r^{D,A} > r_\mathrm{SF}$.

The SF rate constant, k_{SF}, and the SF radius, r_{SF}, are input parameters of the MC simulation. To find the best fit to the experimental fluorescence and anisotropy data, the MC simulation was run for numerous values of r_{SF} and k_{SF} for systems with randomly distributed as well as various degrees of clustered TIPS-Pn molecules.

6.2 Simulated Steady-state Absorption and Emission Spectra

The singlet migration rate depends on the spectral overlap between the donor and acceptor, calculated by integrating over the product of the emission spectrum of the donor and absorption spectrum of the acceptor.

The steady-state absorption and emission spectra of the TIPS-Pn molecules are simulated by a Franck-Condon progression as described in Section 2.4.3. The simulated steady-state absorption spectrum is generated by summing over the absorption spectra of all TIPS-Pn molecules. The simulated steady-state fluorescence spectrum is generated by summing over only those that decay during the MC simulation.

Figure 6.1 shows the simulated and experimental steady-state absorption and fluorescence spectra of the 1:10 TIPS-Pn:PMMA NPs. The characteristic 0–0 and 0–1 transitions, along with the distinct vibrational features, are well represented by the MC simulation. The Stokes shift is replicated since a higher proportion of lower energy chromophores fluoresce.

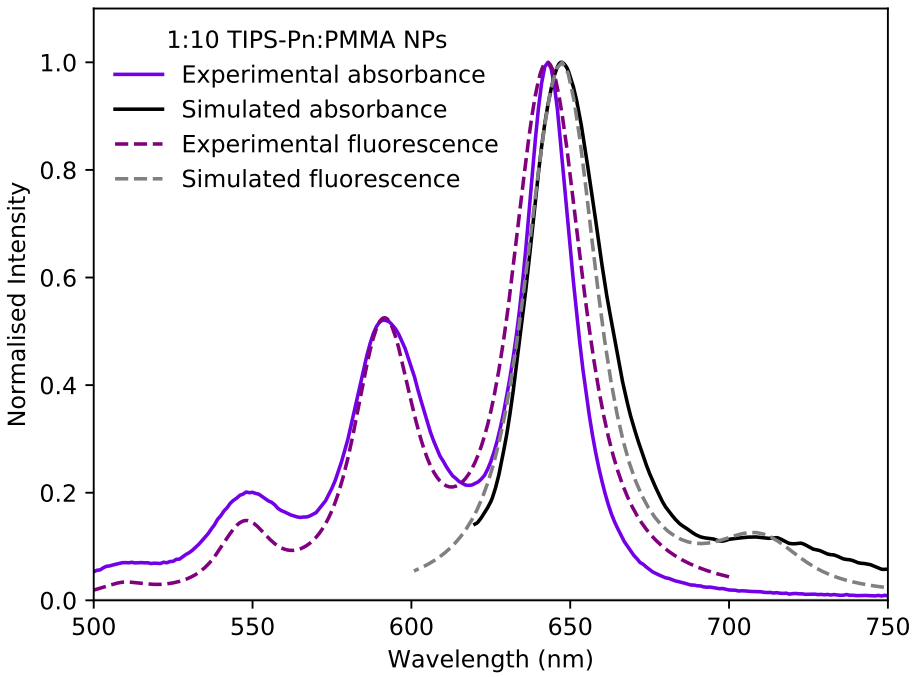

Figure 6.1: Experimental and simulated steady-state absorption and fluorescence emission for the 1:10 TIPS-Pn:PMMA NPs. Section 2.4.3 contains a detailed description of the method employed to obtain the simulated data.

6.3 Effect of r_{SF} and k_{SF}

We will now discuss the effect that changing the input parameters, r_{SF} and k_{SF}, has on our simulated fluorescence and anisotropy decay.

6.3.1 Fluorescence

Increasing the SF radius, r_{SF}, was found to increase the rate of the simulated fluorescence decay. This can be explained by an increased r_{SF} effectively increasing the number of SF sites. A larger number of SF sites would result in a singlet having to hop fewer times to reach a SF and be able to undergo SF. Hence, the overall ensemble rate of SF would increase. This would result in more singlets undergoing SF, rather than singlet decay, so fluorescence is quenched faster and the rate of fluorescence emission decay is increased.

Increasing the rate of SF, k_{SF}, was also found to increase the rate of fluorescence decay. This is explained in a similar way, as an increased rate effectively increases the amount of SF relative to singlet decay, and so fluorescence is again quenched faster.

Although increasing r_{SF} and k_{SF} increase the rate of fluorescence decay, they have slightly different effects on the fluorescence decay shape. It must therefore be noted that there exists only one unique set of r_{SF} and k_{SF} that results in the simulated data matching the experimental data of a specific NP sample.

6.3.2 Fluorescence Anisotropy

Increasing r_{SF} effectively increases the amount of SF sites and thus increases the overall SF rate. Increasing k_{SF} also increases the overall rate of SF. Consequently, increasing either r_{SF} or k_{SF} results in a greater competition between SF and singlet migration. Increasing either r_{SF} or k_{SF} does not significantly affect the fluorescence anisotropy at early times, suggesting that singlet migration is dominant at these times. At intermediate times (3 to $\sim$50 ps), increasing r_{SF} or k_{SF} slows down the fluorescence anisotropy decay, suggesting that SF is significantly competing with singlet migration. As SF becomes more dominant, the fluorescence anisotropy changes from decreasing to slightly increasing over this timescale. At later times, the fluorescence anisotropy decay rate is not significantly affected by r_{SF} or k_{SF}, suggesting negligible SF occurs due to possible singlet trap sites, and slow migration dominates the fluorescence anisotropy decay.

6.4 Simulated Fluorescence and Anisotropy Assuming a Random Distribution of TIPS-Pn within the NPs

We first consider TIPS-Pn molecules within the NPs to be randomly distributed. The coordinates and transition dipole moments were extracted from the MD simulation just after energy minimisation to ensure no TIPS-Pn molecules are overlapping (refer to Section 2.4.1.3).

The MC simulation was run for the different NP systems with a variety of reasonable r_{SF} values (ranging from 0.9 to 1.4 nm) and various k_{SF} values which could possibly reproduce the experimental fluorescence (ranging from 5×10^{10} to 5×10^{11} s^{-1}).[57] The

MC simulation was run for 1×10^5 excitations, and the experimental and simulated fluorescence data scaled to 1 to compare the fluorescence decay.

The MC simulation show agreement with the fluorescence decay of the 1:0 sample with $r_{\mathrm{SF}} = 1.1\,\mathrm{nm}$ and $k_{\mathrm{SF}} = 1 \times 10^{11}\,\mathrm{s}^{-1}$, but none of the data of the other NP systems could be fit with these same values of r_{SF} and k_{SF}. This phenomenon is highlighted in Figure 6.2. The shape of the experimental fluorescence decay is somewhat reproduced for the 1:1 and 1:3 samples, but the MC simulation fails to reproduce the experimental data for the higher mass ratios.

The corresponding experimental, fitted and simulated time-resolved fluorescence anisotropy is shown in Figure 6.3. The experimental fluorescence anisotropy show ultrafast depolarisation occurring on a timescale <100 fs, below the instrument response time. Ultrafast fluorescence depolarisation can be attributed to geometrical changes due to strong coupling between electronic and nuclear degrees of freedom.[105] These geometrical changes result in an initial fluorescence anisotropy value lower than 0.4, which is the expected value with perfect correlation of absorption and emission polarisations. The absence of ultrafast depolarisation in the MC simulation that is observed in the experimental data highlights some deficiencies in the MC simulation. We therefore focus on the shape of the fluorescence anisotropy rather than the initial anisotropy value. The shape of the fluorescence anisotropy is somewhat replicated by the MC simulation only for the 1:0, 1:1 and 1:3 samples. Nevertheless, it is evident that the MC simulation fails to replicate the shape of the fluorescence anisotropy decay for the higher mass ratio samples.

As the MC simulation cannot reproduce data for all mass ratios with one set of r_{SF} and k_{SF}, we consider the limitations of the MC simulation. Firstly, the lack of fit could be attributed to the simple SF model used. It is assumed that there is a defined cut-off distance between a singlet and a neighbouring ground-state molecule, and that within this distance, the SF rate is constant. This is a very simple model, as it would be expected that the rate of SF is somehow dependent on the distance between the singlet and ground-state molecule that are undergoing SF. SF is effectively the reverse process of triplet-triplet annihilation, which is related to the Dexter excitation transfer (DET) mechanism. Accordingly, one might assume that SF depends exponentially on the distance between the singlet and ground-state molecule, as observed by Tian et al. in rubrene-doped organic films.[122] Hence, an alternative SF rate was trialled,

$$k_{\mathrm{SF}}^{D,A} = k_{\mathrm{SF}_0} \exp(-\beta r^{D,A}), \tag{6.2}$$

where D and A denote the "donor" singlet molecule and "acceptor" ground-state molecule, respectively, $r^{D,A}$ is the distance between those two molecules, k_{SF_0} is the maximum rate of SF, and β is a constant.

Although this model of SF is more comprehensive, the MC simulation fails to produce a fluorescence decay that resembles the experimental data. There are several issues with this model:

1. no combination of k_{SF_0} and β was found to fit the data. The early time decay could be replicated but then the fluorescence decay would be too fast at late times.

2. Increasing k_{SF_0} would increase the fluorescence decay at early times while increasing β was found to decrease the fluorescence decay. k_{SF_0} and β were not independent, so similar simulation curves could be produced with numerous sets.

3. No one set of parameters could fit the early fluorescence decay of all the NP samples.

Comprehending the SF model by assuming the SF rate to be exponentially dependent on the distance does not resolve the issue encountered by using the simplified SF rate model. It only causes further problems and does not fit the data. We therefore return to the simple SF model discussed earlier (in Section 6.1).

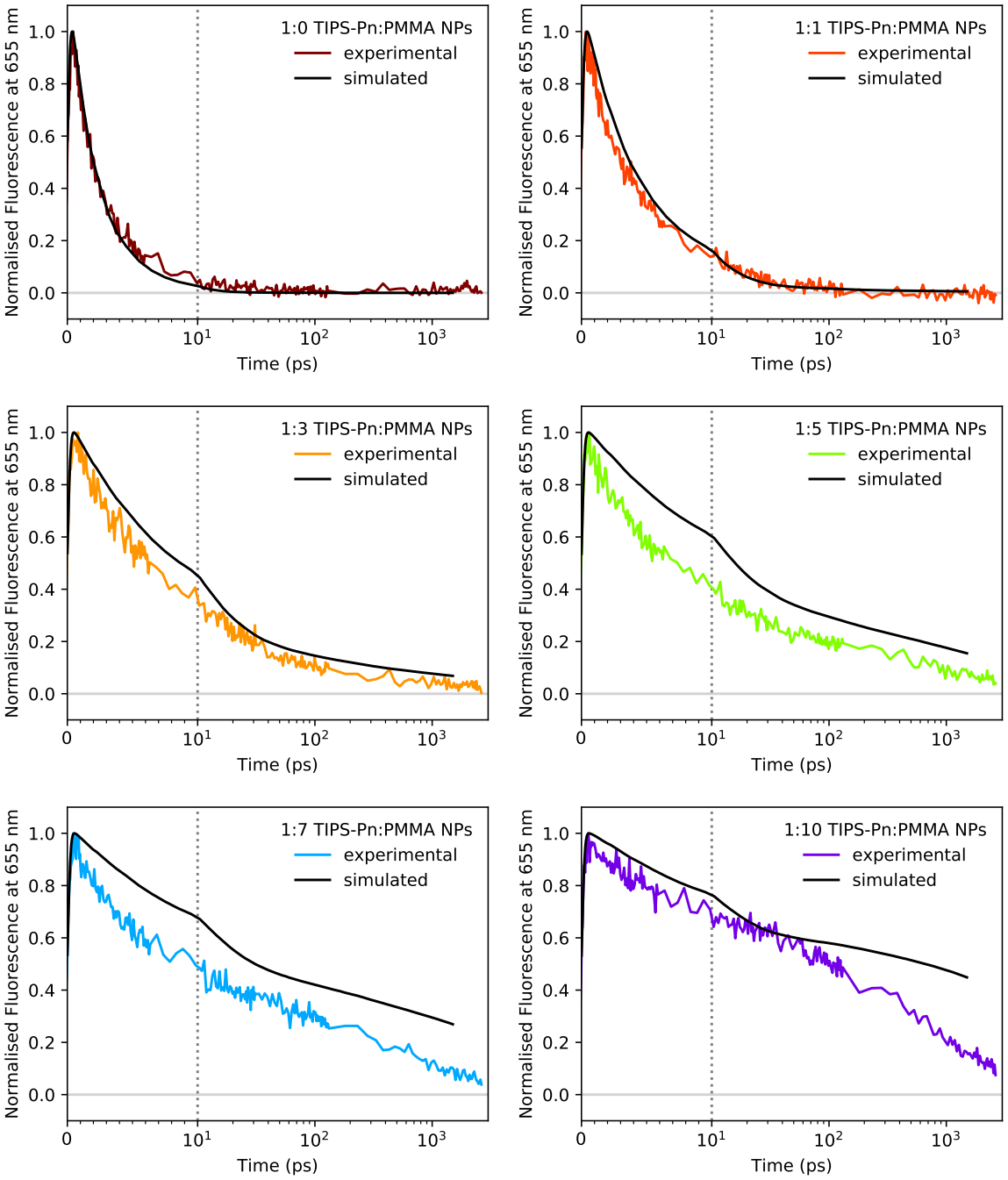

Figure 6.2: Experimental and simulated magic-angle fluorescence data for various TIPS-Pn/PMMA NPs. The simulated data was obtained assuming a random distribution of TIPS-Pn molecules, with $r_{\mathrm{SF}} = 1.1\,\mathrm{nm}$ and $k_{\mathrm{SF}} = 1.0 \times 10^{11}\,\mathrm{s}^{-1}$. The dotted grey lines indicate a change from a linear to logarithmic scale.

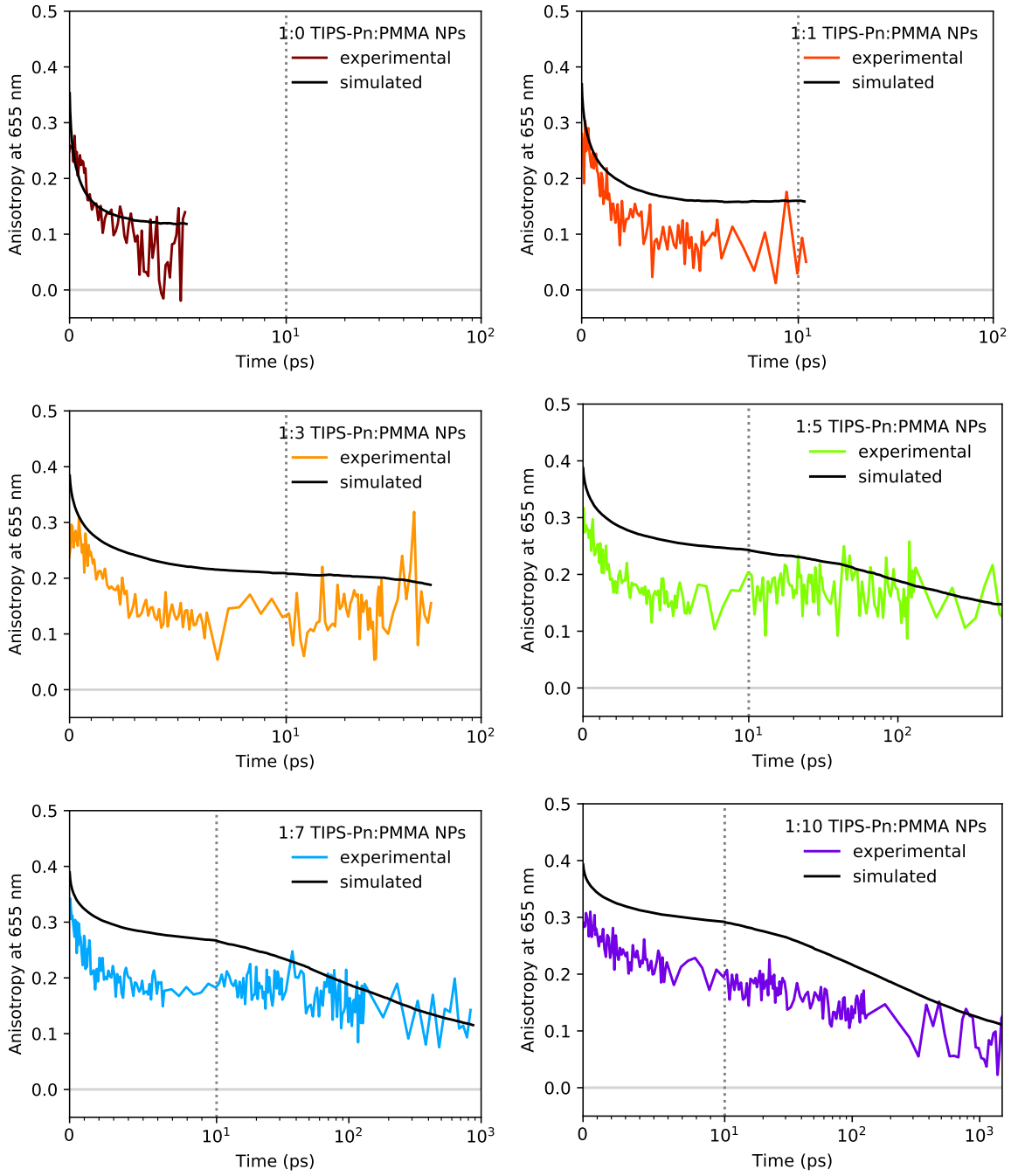

Figure 6.3: Experimental and simulated time-resolved fluorescence anisotropy for various TIPS-Pn/PMMA NPs. The simulated data was obtained assuming a random distribution of TIPS-Pn molecules, with $r_{SF} = 1.1\,\text{nm}$ and $k_{SF} = 1.0 \times 10^{11}\,\text{s}^{-1}$. The dotted grey lines indicate a change from a linear to logarithmic scale.

Up until this point, we have assumed TIPS-Pn molecules to be randomly distributed within our NPs. However, it is possible that during the NP formation TIPS-Pn-TIPS-Pn or PMMA-PMMA interactions are favoured, driving some degree of phase separation. This would result in TIPS-Pn molecules forming a more "clustered" distribution within the NPs. Consequently, the positions and transition dipole moments were extracted from the MD simulation at various timesteps (corresponding to different degrees of clustering) and used as input for the MC simulation. The various degrees

of clustering will be discussed in Section 6.5.1. We return to the simplified SF model and run the MC simulation with a variety of r_{SF} and k_{SF} for several different TIPS-Pn distributions within our NP systems.

6.5 Simulated Fluorescence and Anisotropy Assuming Clustering of TIPS-Pn within the NPs

Assuming TIPS-Pn molecules to be randomly distributed within the NPs did not allow the MC simulation to reproduce the experimental fluorescence and anisotropy decay. Although the steady-state spectra provide evidence that the NPs are amorphous, the idea that the NPs consist of amorphous TIPS-Pn clusters cannot be excluded. Hence, the MC simulation was run on several different amorphous TIPS-Pn distributions.

It was found that the MC simulation could reproduce the experimental fluorescence decay with $r_{SF} = 1.1\,\text{nm}$ and $k_{SF} = 1.0 \times 10^{11}\,\text{s}^{-1}$ for all NP samples when different clustered distributions of TIPS-Pn was assumed. The simulated fluorescence and anisotropy curves with these parameters are shown alongside the experimental data in Figures 6.4 and 6.5. The corresponding degree of clustering for each NP sample is shown in Figure 6.8. We explain in the following section how we quantify the degree of clustering.

The simulated fluorescence curves show excellent agreement with the experimental fluorescence curves, especially for the samples with lower proportions of PMMA. The simulated fluorescence of the 1:10 sample, however, is only able to fit at early times. As the 1:10 sample has the lowest proportion of TIPS-Pn, it is thus most sensitive to the preparation procedure. Subtle differences in preparation of these NPs may lead to large differences in morphology that are not captured by our simulation. Regardless, the simulated fluorescence of the 1:10 sample is still reproduced more accurately assuming a clustered distribution than a random distribution of TIPS-Pn molecules.

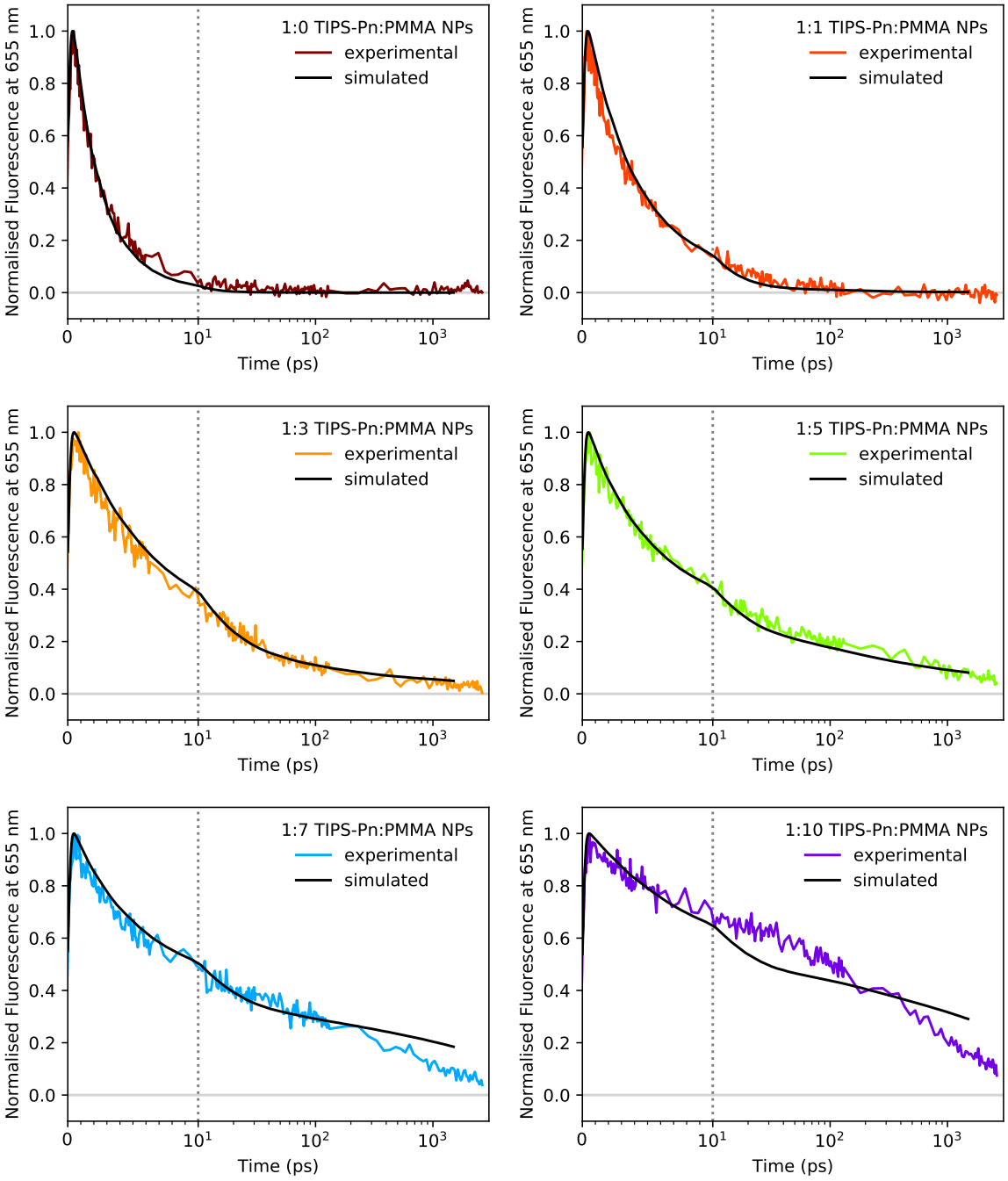

Figure 6.4: Experimental and simulated magic-angle fluorescence data for various TIPS-Pn/PMMA NPs. The simulated data was obtained assuming a clustered distribution of TIPS-Pn molecules, with $r_{\mathrm{SF}} = 1.1\,\mathrm{nm}$ and $k_{\mathrm{SF}} = 1.0 \times 10^{11}\,\mathrm{s}^{-1}$. The dotted grey lines indicate a change from a linear to logarithmic scale.

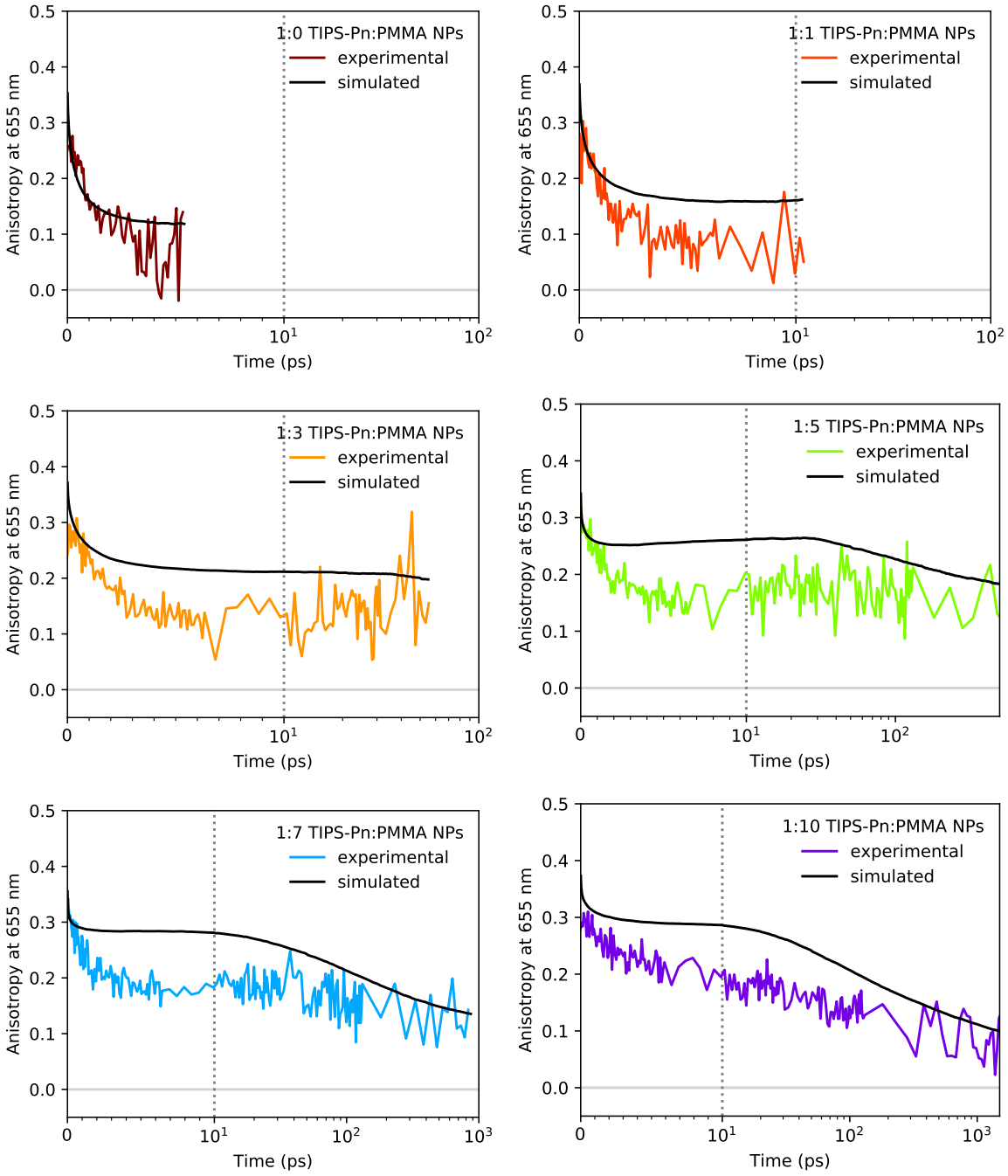

Figure 6.5: Experimental and simulated time-resolved fluorescence anisotropy for various TIPS-Pn/PMMA NPs. The simulated data was obtained assuming a clustered distribution of TIPS-Pn molecules, with $r_{SF} = 1.1\,\text{nm}$ and $k_{SF} = 1.0 \times 10^{11}\,\text{s}^{-1}$. The dotted grey lines indicate a change from a linear to logarithmic scale.

6.5.1 Quantifying the Degree of Clustering of TIPS-Pn molecules

The MC simulation could reproduce the experimental fluorescence data by assuming a degree of clustering of TIPS-Pn within the NPs. Aiming to find a way to quantify this degree of clustering, we follow the convention of Felfer et al., who demonstrated a method to assess if clusters are present beyond what is expected in a random distribution.[123]

Firstly, we discuss the distribution of individual molecules (or "points") and how to determine whether these molecules are "clustered". To determine whether a molecule has neighbouring molecules closer to it than what would be expected in a random distribution, we define a concentration field based on the positions of individual molecules. The concentration of an individual molecule, c_{molecule}, is the inverse of the region in space v_{V_0} that the molecule uniquely occupies ($c_{\text{molecule}} = \frac{1}{v_{\text{V}_0}}$). v_{V_0} is the volume closer to this molecule than any other molecule. This is referred to as the "Voronoi volume" of the molecule and has been described in Section 2.5.1.

Molecules are considered "clustered" when c_{molecule} is greater than some threshold density, c_{thresh}. In other words, if a molecule has a Voronoi volume smaller than some threshold v_{thresh}, then the molecules are more likely to belong to the random distribution than to a clustered distribution. The Voronoi volumes of the individual molecules are used for analysis as their distribution is easier to display, but the reader is reminded that this is just the inverse of the concentration and so c_{molecule} and v_{V_0} can be used interchangeably. To quantify the amount of clustered molecules, the Voronoi volume distribution of a system with randomly distributed molecules needs to be known. One can then determine how the Voronoi volume distribution of a more clustered system differs to that of a random distribution.

We approximate TIPS-Pn molecules as points and obtain the Voronoi volumes for every molecule in our NP systems. The Voronoi volume distributions of the random and the clustered distribution of TIPS-Pn are displayed in Figure 6.6. The random distribution for each system is taken from the MD simulation just after energy minimisation and the clustered distribution taken at a timestep corresponding to the best MC simulated fit to the experimental fluorescence data.

As expected, the clustered distribution shows a shift to smaller Voronoi volumes relative to the random distribution. Consequently, the clustered distribution also has a higher proportion of TIPS-Pn molecules with a larger Voronoi volume than the random distribution. These results are most easily explained by the illustration in Figure 6.7.

The histograms for the Voronoi volume distributions are well represented by a gamma distribution and were thus used to help analyse the data. Therefore, histograms for the random and clustered distributions were fit with the probability density function for gamma,

$$f(x, a) = \frac{x^{a-1}\exp(-x)}{\Gamma(a)}, \tag{6.3}$$

where $x \geq 0$, $a > 0$ is an integer, and Γ refers to the gamma function. We then subtract the random distribution from the clustered distribution (which we term the "difference" curve) and define v_{thresh}, the Voronoi volume below which TIPS-Pn molecules are more likely to belong to the random than the clustered distribution. To determine the percentage of "clustered" TIPS-Pn molecules, the difference curve is integrated up to v_{thresh}. The corresponding percentage of clustering for each NP sample

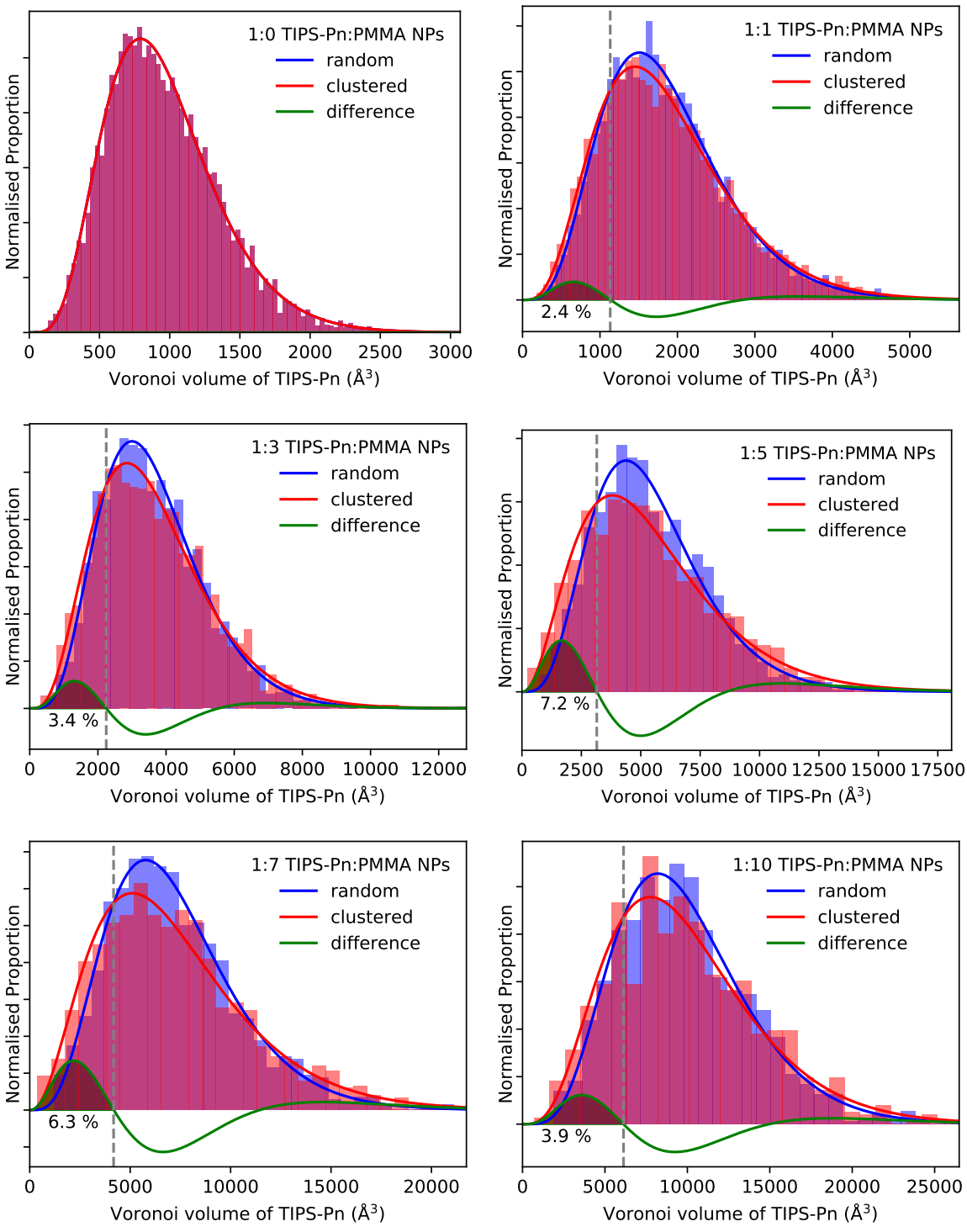

Figure 6.6: Voronoi analysis of the TIPS-Pn molecules in the TIPS-Pn/PMMA NPs. The random distribution for each NP sample is taken from the MD simulation just after energy minimisation and the clustered distribution taken at a timestep corresponding to the best MC simulated fit to the experimental fluorescence data. TIPS-Pn molecules are considered "clustered" if they are not likely to belong to the random distribution. This is calculated by integrating the difference between the clustered and randomly distributed curves from 0 up to v_{thresh} (dashed grey line), as indicated by the green shaded area.

is displayed in Figure 6.8. The percentage of clustering refers to the number of clustered TIPS-Pn molecules divided by the total number of TIPS-Pn molecules in the NP. As the different NP systems have different number of TIPS-Pn molecules within the 20 nm MD simulation box, comparing the percentage of clustering between different mass ratios of TIPS-Pn:PMMA NPs is not very insightful. Instead, we are interested in how different degrees of clustering affect the amount of SF sites present in the NPs. Figure 6.9 displays the percentage of SF sites within the NP samples for the random and clustered TIPS-Pn distributions.

We conclude that in order to fit the experimental data with our MC simulation,

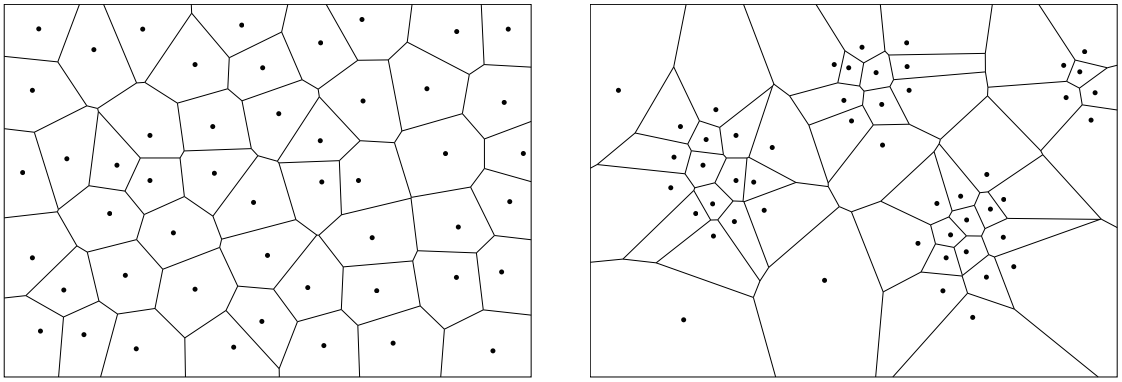

Figure 6.7: Voronoi diagrams for a random (left) and clustered (right) TIPS-Pn distribution, where TIPS-Pn are represented as points. Note that this diagram is a 2D representation of the three-dimensional (3D) NP system. Although the average Voronoi volume is equal for both distributions, the *distributions* of Voronoi volumes are different. The system with a random TIPS-Pn distribution has Voronoi volumes which can be described by a normal distribution. The system with a clustered TIPS-Pn distribution has a Voronoi volume distribution with a larger number of smaller volumes and consequently also a higher proportion of larger volumes than the random TIPS-Pn distribution. These different distributions are evident in Figure 6.6.

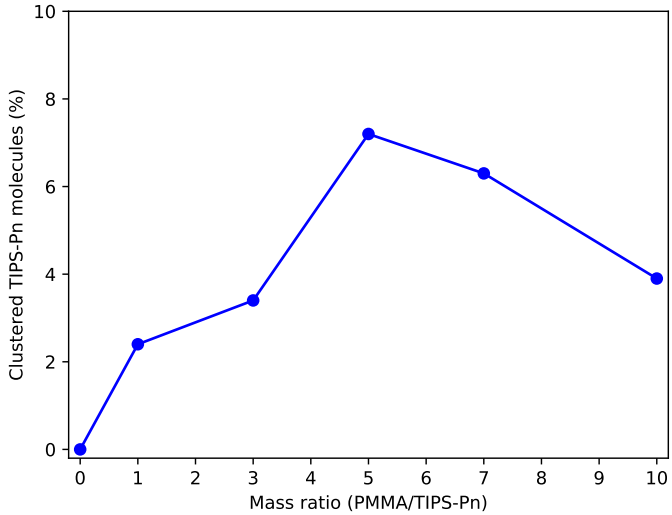

Figure 6.8: The percentage of TIPS-Pn molecules which are required to be "clustered" within each of the TIPS-Pn/PMMA NP systems in order for the MC simulation to fit the experimental data. TIPS-Pn molecules are considered "clustered" if they are not likely to belong to the random distribution.

more SF sites in our NPs are required than would be achieved if TIPS-Pn molecules were to be randomly distributed within these NPs. In other words, there is a requirement for a certain degree of clustered TIPS-Pn molecules.

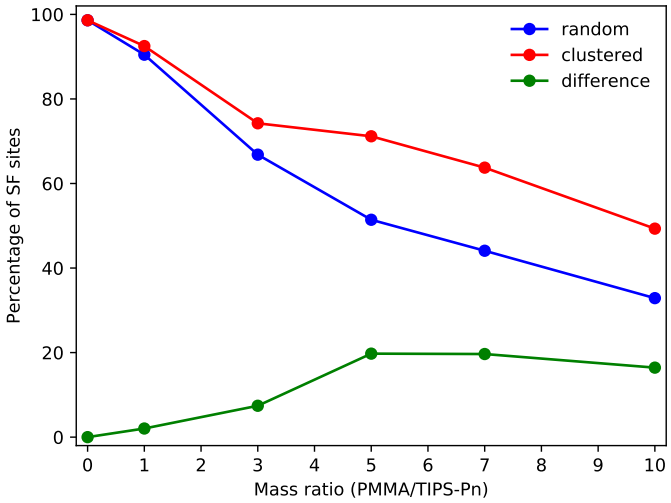

Figure 6.9: The percentage of SF sites for each of the TIPS-Pn/PMMA NPs for random and clustered TIPS-Pn distributions. A chromophore is considered to be a "SF site" if it has another chromophore within 1.1 nm of it (as $r_{SF} = 1.1\,\text{nm}$ is used in the MC simulation).

6.6 Effect of Singlet Fission

The advantage of the MC simulation is that the amount of SF and the SF rate can be controlled. By turning off SF we are able to obtain results due to purely singlet migration within the various NP systems. Comparing this to the results with SF allows us to examine the effect SF has on the time-resolved fluorescence anisotropy. The results presented in the following sections involve using the parameters ($r_{SF} = 1.1\,\text{nm}$, $k_{SF} = 1.0 \times 10^{11}\,\text{s}^{-1}$) and the clustered distributions of TIPS-Pn which were found to allow the MC simulation to best fit the experimental fluorescence and anisotropy data.

6.6.1 Effect of Singlet Fission on Singlet Hopping and the Mean Squared Displacement of Singlets

The number of singlet hops before decay or SF is displayed in Figure 6.10. Figure 6.11 shows the MSD of singlets over time. Let us first focus on the singlet hop and MSD plots from the MC simulation in which SF does not occur (Figure 6.10a and 6.11a, respectively). Singlet hopping thus only competes with singlet decay. The number of hops was restricted to 10 to increase simulation speed, with minimal affect on the data. Proportionally more hops occur in systems with a lower proportion of PMMA (i.e. NPs with a shorter average intermolecular TIPS-Pn separation). This trend is consistent with expectations, as the rate of hopping is faster for shorter distances between chromophores (refer to Equations 1.3 and 1.4 in Section 1.4.1). The MSD due to singlet migration only (Figure 6.11a) further confirms faster singlet diffusion in NP systems with a shorter average intermolecular TIPS-Pn separation. Although the hopping distance in the 1:0 sample is shorter compared to the other mass ratios,

faster diffusion (i.e. more hops) means the singlets diffuse further (as seen by the larger limiting MSD value).

We now focus on singlet hop and MSD plots from the MC simulation in which SF can occur (Figure 6.10b and 6.11b, respectively). Hopping competes with SF as well as singlet decay, resulting in a decrease in the number of hops for all mass ratios. If the amount of SF were to be equal for each NP sample, the hop distributions would look similar to Figure 6.10a, but with all mass ratios positively skewed. However, in Chapter 4 we identified that more SF occurs for the NP samples with a lower proportion of PMMA. Although the rate of singlet hopping is still faster in the 1:0 sample, SF is also more pronounced in the 1:0 sample, resulting in less hops compared to the other mass ratios. Fewer hops and a shorter hopping distance for the 1:0 sample means the singlets do not diffuse as far compared to in the system where no SF occurs. The maximum MSD of singlets with migration and SF (Figure 6.11b) is significantly lower than that of singlets with migration only (Figure 6.11a).

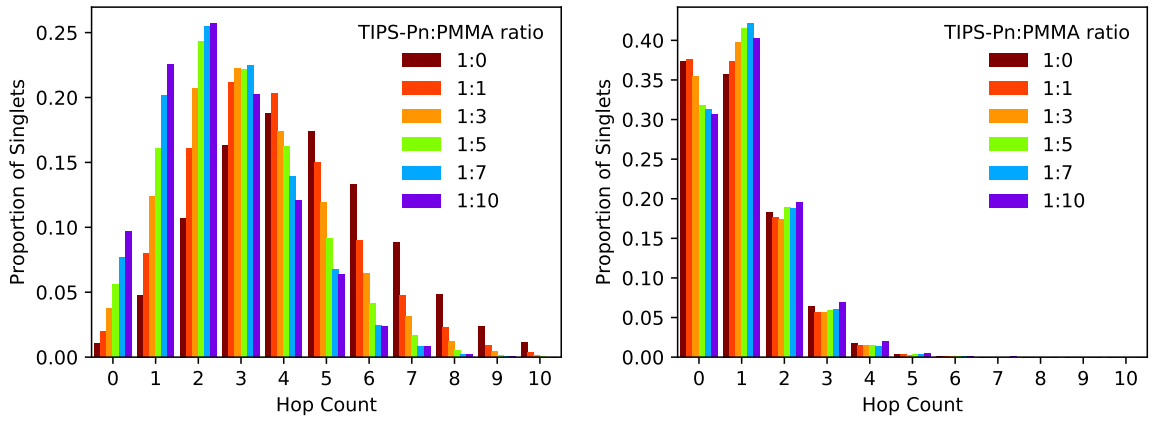

(a) migration only **(b)** migration + SF

Figure 6.10: Hop count histogram for the different TIPS-Pn/PMMA NP systems from the MC simulation run **a)** without SF, "migration only", and **b)** with SF, "migration + SF".

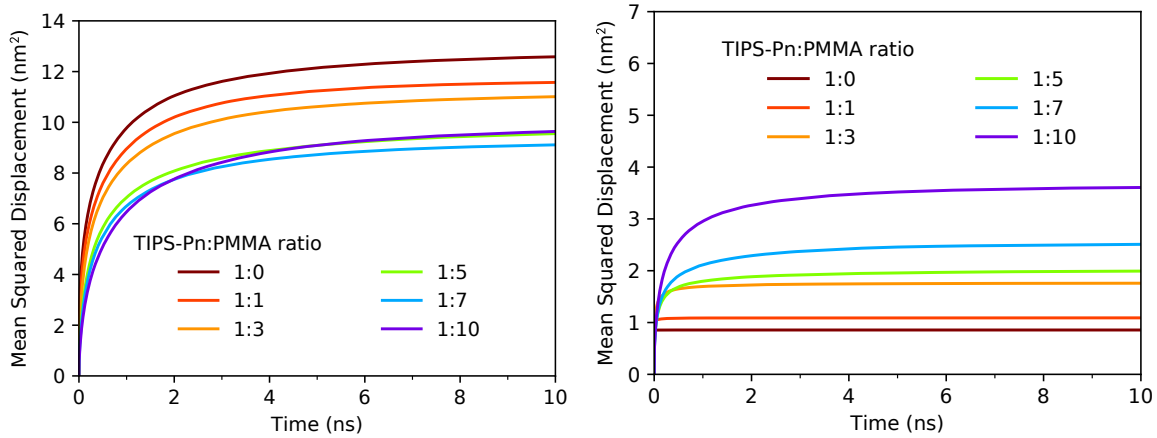

(a) migration only **(b)** migration + SF

Figure 6.11: MSD of the singlets in the different TIPS-Pn/PMMA NP systems from the MC simulation run **a)** without SF, "migration only", and **b)** with SF, "migration + SF".

6.6.2 Effect of Singlet Fission on the Fluorescence Anisotropy

Time-resolved fluorescence anisotropy can give a measurement of the rate of singlet migration within the NP systems, if it were the only cause of depolarisation. In Chapter 5 it was concluded the fluorescence anisotropy decay decreased faster for NP samples with a shorter average intermolecular TIPS-Pn separation. However, a significant amount of SF is present in our NPs and we must consider the effect it could have on the time-resolved fluorescence anisotropy. In Section 5.1.1, details on how diffusion-limited SF could affect the anisotropy were discussed. Briefly, diffusion-limited SF describes the process in which a singlet must first migrate to a specific site where it can undergo SF, termed "SF site". A singlet is more likely going to have reached a SF site if it has undergone faster migration. Faster migration however, results in faster loss of correlation with the initial excitation polarisation. Consequently, diffusion-limited SF would selectively eliminate less correlated singlets and thereby could act to increase the anisotropy.

The influence of diffusion-limited SF on the fluorescence anisotropy can be investigated by comparing the simulated time-resolved fluorescence anisotropy of systems in which the singlets can and cannot undergo SF. We have already presented the simulated fluorescence and anisotropy data obtained from adjusting the SF parameters and TIPS-Pn clustering such that the simulated curves fit the experimental data. By turning SF off, we obtain the simulated time-resolved fluorescence anisotropy due to migration only, in the same systems. These data are presented in Figure 6.12. Direct comparison allows a clear detection of the effect of SF on the fluorescence anisotropy.

As expected, the simulated fluorescence anisotropy due to migration only show a faster decrease in anisotropy for systems with a shorter average TIPS-Pn intermolecular separation. SF makes analysis of the time-resolved fluorescence anisotropy slightly more complicated. From the black traces in Figure 6.12, it can be seen that diffusion-limited SF acts to increase the fluorescence anisotropy (relative to the anisotropy from just migration). As explained, this can be attributed to diffusion-limited SF eliminating less correlated singlets.

The shape of the time-resolved fluorescence anisotropy is determined by the two processes affecting the anisotropy: singlet migration and diffusion-limited SF. The amount of singlet migration decreases with time, as shown by the red curve in Figure 6.13. The amount of diffusion-limited SF increases as singlets migrate to SF sites, but then decreases as singlets are eliminated by SF,[57] as shown by the green curve in Figure 6.13. The rate of singlet migration determines the rate of decrease of correlated singlets. Due to diffusion-limited SF eliminating less correlated singlets, the amount of SF over time determines the rate of increase in the proportion of correlated singlets. The interplay between the effects of singlet migration and diffusion-limited SF determines the shape of the measured time-resolved fluorescence anisotropy, as illustrated by the black curve in Figure 6.13.

When comparing the simulated and experimental time-resolved fluorescence anisotropy, we will *not* focus on the absolute offset, as the simulated fluorescence anisotropy is scaled to start at the theoretical maximum of 0.4, but the initial anisotropy for the experimental data starts below 0.4, as discussed in Section 6.4. Instead, we focus on how the simulated fluorescence anisotropy is able to reproduce the *shape* of the experimental anisotropy.

Figure 6.12 shows that the "migration only" fluorescence anisotropy does not capture the correct shape of the experimental fluorescence anisotropy for the systems

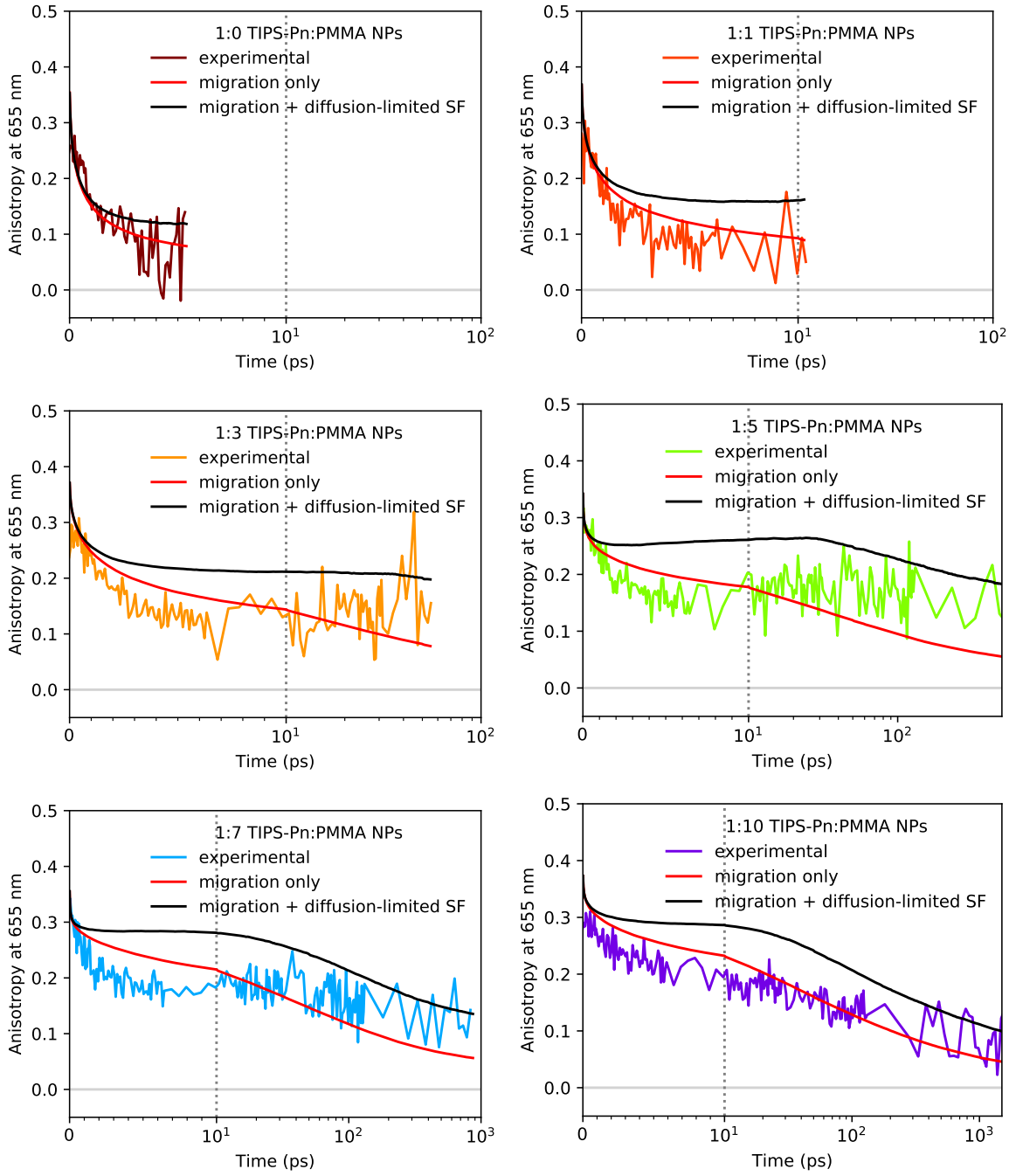

Figure 6.12: Experimental and simulated time-resolved fluorescence anisotropy for various TIPS-Pn/PMMA NPs. The "migration only" simulated time-resolved fluorescence anisotropy was obtained by turning SF off (i.e. by setting $r_{\mathrm{SF}} = 0$). The dotted grey lines indicate a change from a linear to logarithmic scale.

with a higher proportion of PMMA. The shape of the "migration only" MC simulation shows good agreement with the experimental fluorescence anisotropy at early times but completely overestimates the decay at late times. The "migration + SF" simulated fluorescence anisotropy is able to capture the overall shape of the experimental anisotropy (the slight rise in the anisotropy from ∼10 ps to 100 ps), but does not exhibit sufficiently fast decay at early times. The simulated curve increases too early relative to the experimental data, possibly because SF acts too early. This re-

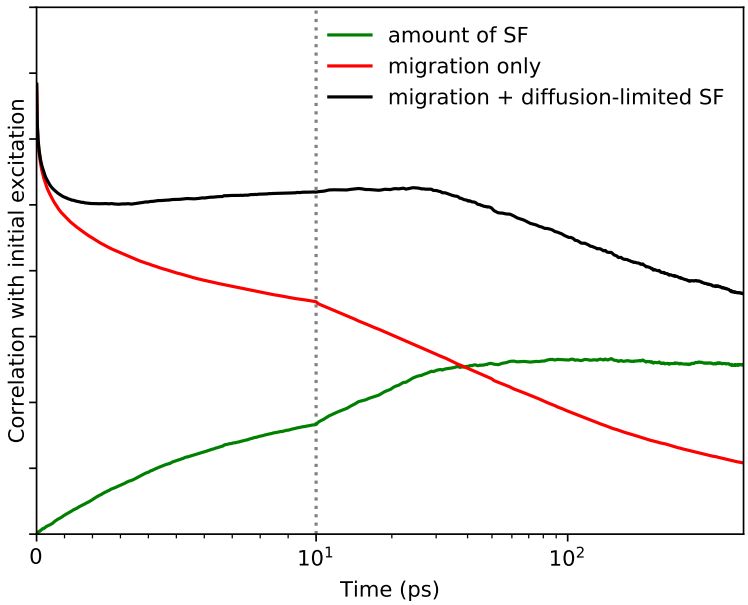

Figure 6.13: The amount of SF (green) and the rate of migration (red) affect the proportion of singlets showing a correlation with the initial excitation polarisation (black).

sult brings us to another limitation of the SF model used in the MC simulation. It has been demonstrated that SF preferentially occurs for certain relative orientations of singlet and ground-state molecules. In the MC simulation, however, a singlet does not require a ground-state molecule to have a specific relative orientation in order for SF to occur. For diffusion-limited SF, an orientational dependence on SF sites would affect the anisotropy. Requiring a singlet to have a ground-state molecule with some optimal relative orientation for SF to occur essentially decreases the amount of potential SF sites (for a given set of r_{SF} and k_{SF}). A singlet would, on average, then have to hop further to reach a SF site. As the overall ensemble rate of SF would be slower, one may expect SF to affect the fluorescence anisotropy less at early times. This may result in a simulated fluorescence anisotropy curve that is more similar to the anisotropy due to migration only at early times, but still captures the increasing anisotropy at the intermediate time range. Thus, it is possible that the experimental data could be fit better if the MC simulation included an orientational dependence on SF.

6.7 Conclusions

The MC simulation of the TIPS-Pn/PMMA NP systems was able to reproduce the experimental magic-angle fluorescence data, by assuming only a very simple SF model and a degree of clustering of TIPS-Pn within the NP systems. Furthermore, the MC simulation allowed for separation of the effects of singlet migration and diffusion-limited SF on the fluorescence anisotropy. It is clear that SF competes with singlet migration, reducing the average number of singlet hops and significantly decreasing the MSDs of singlets. Comparing MC simulations with and without SF clearly reveals that diffusion-limited SF acts to increase the fluorescence anisotropy. In our amorphous NP systems, this is explained by diffusion-limited SF selectively eliminating singlets which are less correlated with the initial excitation polarisation.

CHAPTER 7
Conclusions and Future Directions

SF has the potential to increase the theoretical efficiency of conventional solar cells beyond the Shockley-Queisser limit. However, the lack of concrete understanding of the SF process restricts the effective implementation of a SF layer into a photovoltaic device. In this thesis, the effect of average interchromophore separation on SF and exciton migration was studied using time-resolved spectroscopy and a MC simulation.

Chapter 3 describes the amorphous TIPS-Pn/PMMA NPs studied in this thesis. These NPs degraded by ∼10% over the course of one week but showed colloidal stability for over nine weeks. The resemblance of their steady-state absorption spectra to that of TIPS-Pn in THF provides evidence that TIPS-Pn does not form crystalline domains within the NPs. By varying the TIPS-Pn:PMMA mass ratios within the NPs, these NPs provide a unique way of controlling the average intermolecular TIPS-Pn separation. Therefore, this system allows us to investigate the effect of average interchromophore separation on SF dynamics, exciton migration and related processes.

In Chapter 4, time-resolved spectroscopic fluorescence data reveal a faster depletion of the singlet population for shorter average intermolecular TIPS-Pn separations. TA spectroscopic data in the visible and NIR regions display a concurrent rise of triplet ESA features with the decay of singlets. This result confirms that SF is present in the NPs, as triplets formed on a timescale too fast to be attributed to ISC.[54] A faster rate of SF was observed for NP samples with a shorter average intermolecular TIPS-Pn separation.

Time-resolved fluorescence and TA polarisation anisotropy data were obtained and presented in Chapter 5 to understand SF and the exciton migration within our NPs. In the NP samples, rotational diffusion of TIPS-Pn molecules is slow and has negligible effect on the anisotropy. Fluorescence anisotropy is a representation of the depolarisation of the singlet population, and was found to decay faster for NP samples with a shorter average intermolecular TIPS-Pn separation. However, we demonstrate that SF affects the fluorescence anisotropy, resulting in constant (or even a slightly increased) anisotropy between 5 and 100 ps.

TA anisotropy offers the opportunity to monitor the migration of different excited-state species, if a specific wavelength can be assigned to just one excited-state species. However, the TA spectra of our NPs have contributions from the GSB, SE and ESA at most wavelengths. Therefore, no single wavelength can be assigned to the ESA of the pure singlet or triplet. However, at both 650 nm (containing the GSB, SE and possibly some ESA) and at 508 nm (ESA of singlets and triplets), the TA anisotropy was found to decay more rapidly for NP samples with a shorter average intermolecular TIPS-Pn separation. The TA in the NIR region has singlet and triplet features that are more clearly separated. At 1350 nm, the TA is mainly due to ESA of singlets. The TA anisotropy decay kinetic at this wavelength reflects that of the fluorescence anisotropy, confirming this assignment but providing no further information. At 990 nm, the TA is mainly due to ESA of triplets. However, nearly all correlation is lost at this wavelength at early times, and so triplet migration cannot be analysed using this signal.

To investigate the effect of SF on the fluorescence anisotropy and with a potential future aim to also analyse the TA anisotropy, a MC simulation of the TIPS-Pn/PMMA NP systems was developed and discussed in Chapter 6. Singlet migration, singlet decay and SF were simulated. Singlet migration was simulated as a FRET process and thus the hopping rate depends on the distance between the donor and acceptor molecules, the alignment of their transition dipoles and their spectral overlap. The singlet decay rate constant was fixed to the intrinsic singlet lifetime found by Stuart et al.[57] A simple SF model was employed, as the microscopic details of SF are not yet fully understood.[112] In this model, it is assumed that SF occurs with a rate of k_{SF} if a singlet molecule has a ground-state molecule within a distance of r_{SF}. These two parameters, k_{SF} and r_{SF}, were adjusted to obtain the best simulated fits to the experimental time-resolved fluorescence and anisotropy data. It was demonstrated that the MC simulation cannot reproduce the time-resolved fluorescence data at magic angle by assuming TIPS-Pn molecules to be randomly distributed within the NPs. As it is possible for TIPS-Pn to form amorphous clusters within the NPs, a simple MD simulation of the NP systems was used to obtain MC simulation input coordinates corresponding to clustering of TIPS-Pn molecules. Assuming different amounts of clustered TIPS-Pn molecules in each system, the MC simulation can fit the fluorescence data at magic angle and the shape of the fluorescence anisotropy with a r_{SF} of 1.1 nm and k_{SF} of $1.0 \times 10^{11}\,\mathrm{s}^{-1}$.

The clustered TIPS-Pn distribution has consequences on the overall rate of SF within the NP systems. Compared to a random distribution, a clustered chromophore distribution may result in a higher SF yield due to the closer distance between chromophores. However, singlet migration may be restricted to a local cluster. Consequently, singlets excited to clusters containing only a few or a single chromophore may become "trapped" and can thus only undergo decay.

The MC simulation also allows for separation of the effects of singlet migration and diffusion-limited SF on the fluorescence anisotropy. Comparing MC simulations with and without SF clearly reveals that diffusion-limited SF acts to increase the fluorescence anisotropy. In our amorphous NP systems, this is explained by diffusion-limited SF selectively eliminating singlets which are less correlated with the excitation polarisation. It is clear that a singlet migration rate cannot be directly extracted from the fluorescence anisotropy of an amorphous system which undergoes diffusion-limited SF, unless the effects of singlet migration and SF are separated.

Microscopic modelling of NP systems can offer a means to analyse SF and exciton migration, but further knowledge on the geometry dependence of SF is necessary for refinement of our MC simulation. It would be interesting to modify the SF rate to include an orientational dependence on SF, although this work is out of the scope of this thesis. This may result in simulated fluorescence anisotropy decays that match the experimental data. Future work should also be focused on extending the MC simulation past the SF event by incorporating triplets and their migration through the system. Simulating the ESA of the singlet and triplet, along with the steady-state absorption spectra (to give the GSB component) and fluorescence spectra (to give the SE component), would allow reconstruction of the TA spectra. By optimising MC simulation parameters to match the TA signals at magic angle and the anisotropy data, it would then be possible to obtain simulated TA anisotropy curves corresponding to distinct species (i.e. singlet and triplet). To monitor the triplet migration rate, experimental TA anisotropy on a nanosecond timescale may be required.

The TIPS-Pn/PMMA NPs presented in this thesis provide a useful means to study the effect of average interchromophore separation on SF and exciton migration. Time-resolved polarisation anisotropy is a useful tool to study exciton migration. Our findings show that diffusion-limited SF acts to increase (or suppress the decay of) the fluorescence anisotropy in an amorphous system. It is important in future work to separate the effects of singlet migration and SF before extracting singlet migration rates from fluorescence anisotropy of amorphous systems undergoing diffusion-limited SF. Analyses of TA anisotropy data are further complicated by the many components present in the TA spectra, and these components must be separated to extract migration rates of single species. A significant result of this study is that with the SF model employed in our MC simulation, the experimental fluorescence and anisotropy data can only be reproduced by assuming a degree of clustering of TIPS-Pn within the NP systems. This result suggests that the TIPS-Pn molecules form amorphous clusters within the NP systems, having implications on future interpretations of the distribution of chromophores embedded in a polymer matrix in NPs prepared by the reprecipitation method. In conclusion, the data presented in this thesis highlight the applications of time-resolved polarisation anisotropy which, along with a MC simulation, provides a means to model and analyse the dependence of morphology on SF and exciton migration in amorphous systems.

References

[1] International Energy Agency, Key World Energy Statistics. 2018; `https://webstore.iea.org/download/direct/2291?fileName=Key_World_2018.pdf`, Accessed: 26/11/2018.

[2] Shafiee, S.; Topal, E. When Will Fossil Fuel Reserves Be Diminished? *Energy Policy* **2009**, *37*, 181–189.

[3] Grätzel, M. Solar Energy Conversion by Dye-Sensitized Photovoltaic Cells. *Inorg. Chem.* **2005**, *44*, 6841–6851.

[4] Cook, J.; Nuccitelli, D.; Green, S. A.; Richardson, M.; Winkler, B.; Painting, R.; Way, R.; Jacobs, P.; Skuce, A. Quantifying the Consensus on Anthropogenic Global Warming in the Scientific Literature. *Environ. Res. Lett.* **2013**, *8*, 024024.

[5] Cook, J.; Oreskes, N.; Doran, P. T.; Anderegg, W. R. L.; Verheggen, B.; Maibach, E. W.; Carlton, J. S.; Lewandowsky, S.; Skuce, A. G.; Green, S. A.; Nuccitelli, D.; Jacobs, P.; Richardson, M.; Winkler, B.; Painting, R.; Rice, K. Consensus on Consensus: A Synthesis of Consensus Estimates on Human-caused Global Warming. *Environ. Res. Lett.* **2016**, *11*, 048002.

[6] Lewis, N. S. Toward Cost-Effective Solar Energy Use. *Science* **2007**, *315*, 798–801.

[7] Jean, J.; Brown, P. R.; Jaffe, R. L.; Buonassisi, T.; Bulovic, V. Pathways for Solar Photovoltaics. *Energy Environ. Sci.* **2015**, *8*, 1200–1219.

[8] Yu, J.; Zheng, Y.; Huang, J. Towards High Performance Organic Photovoltaic Cells: A Review of Recent Development in Organic Photovoltaics. *Polymers* **2014**, *6*, 2473–2509.

[9] Shockley, W.; Queisser, H. J. Detailed Balance Limit of Efficiency of P-N Junction Solar Cells. *J. Appl. Phys.* **1961**, *32*, 510–519.

[10] Bremner, S. P.; Levy, M. Y.; Honsberg, C. B. Analysis of Tandem Solar Cell Efficiencies Under AM1.5G Spectrum Using a Rapid Flux Calculation Method. *Prog. Photovoltaics Res. Appl.* **2008**, *16*, 225–233.

[11] Tayebjee, M. J. Y.; Gray-Weale, A. A.; Schmidt, T. W. Thermodynamic Limit of Exciton Fission Solar Cell Efficiency. *J. Phys. Chem. Lett.* **2012**, *3*, 2749–2754.

[12] Tayebjee, M. J. Y.; McCamey, D. R.; Schmidt, T. W. Beyond Shockley–Queisser: Molecular Approaches to High-Efficiency Photovoltaics. *J. Phys. Chem. Lett.* **2015**, *6*, 2367–2378.

[13] Lee, J.; Jadhav, P.; Reusswig, P. D.; Yost, S. R.; Thompson, N. J.; Congreve, D. N.; Hontz, E.; Voorhis, T. V.; Baldo, M. A. Singlet Exciton Fission Photovoltaics. *Acc. Chem. Res.* **2013**, *46*, 1300–1311.

[14] Conibeer, G. Third-generation Photovoltaics. *Mater. Today* **2007**, *10*, 42–50.

[15] Archer, M. D.; Bolton, J. R. Requirements for Ideal Performance of Photochem-

ical and Photovoltaic Solar Energy Converters. *J. Phys. Chem.* **1990**, *94*, 8028–8036.

[16] National Renewable Energy Laboratory, Best Research-Cell Efficiencies. 2018; `https://www.nrel.gov/pv/assets/pdfs/pv-efficiencies-07-17-2018.pdf`, Accessed: 26/11/2018.

[17] Alharbi, F. H.; Kais, S. Theoretical Limits of Photovoltaics Efficiency and Possible Improvements by Intuitive Approaches Learned from Photosynthesis and Quantum coherence. *Renew. Sust. Energy Rev.* **2015**, *43*, 1073–1089.

[18] Congreve, D. N.; Lee, J.; Thompson, N. J.; Hontz, E.; Yost, S. R.; Reusswig, P. D.; Bahlke, M. E.; Reineke, S.; Van Voorhis, T.; Baldo, M. A. External Quantum Efficiency Above 100% in a Singlet-Exciton-Fission-Based Organic Photovoltaic Cell. *Science* **2013**, *340*, 334–337.

[19] Smith, M.; Michl, J. Singlet Fission. *Chem. Rev.* **2010**, *110*, 6891–6936.

[20] Smith, M. B.; Michl, J. Recent Advances in Singlet Fission. *Annu. Rev. Phys. Chem.* **2013**, *64*, 361–386.

[21] Wilson, M. W. B.; Rao, A.; Ehrler, B.; Friend, R. H. Singlet Exciton Fission in Polycrystalline Pentacene: From Photophysics toward Devices. *Acc. Chem. Res.* **2013**, *46*, 1330–1338.

[22] Monahan, N.; Zhu, X.-Y. Charge Transfer-Mediated Singlet Fission. *Annu. Rev. Phys. Chem.* **2015**, *66*, 601–618.

[23] Rao, A.; Friend, R. H. Harnessing Singlet Exciton Fission to Break the Shockley–Queisser Limit. *Nat. Rev. Mater.* **2017**, *2*, 17063.

[24] Xia, J.; Sanders, S. N.; Cheng, W.; Low, J. Z.; Liu, J.; Campos, L. M.; Sun, T. Singlet Fission: Progress and Prospects in Solar and Cells. *Adv. Mater.* **2017**, *29*, 1601652.

[25] Casanova, D. Theoretical Modeling of Singlet Fission. *Chem. Rev.* **2018**, *118*, 7164–7207.

[26] Monahan, N. R.; Sun, D.; Tamura, H.; Williams, K. W.; Xu, B.; Zhong, Y.; Kumar, B.; Nuckolls, C.; Harutyunyan, A. R.; Chen, G.; Dai, H.-L.; Beljonne, D.; Rao, Y.; Zhu, X.-Y. Dynamics of the Triplet-Pair State Reveals the Likely Coexistence of Coherent and Incoherent Singlet Fission in Crystalline Hexacene. *Nat. Chem.* **2017**, *9*, 341–346.

[27] Singh, S.; Jones, W. J.; Siebrand, W.; Stoicheff, B. P.; Schneider, W. G. Laser Generation of Excitons and Fluorescence in Anthracene Crystals. *J. Chem. Phys.* **1965**, *42*, 330–342.

[28] Hanna, M. C.; Nozik, A. J. Solar Conversion Efficiency of Photovoltaic and Photoelectrolysis Cells with Carrier Multiplication Absorbers. *J. Appl. Phys.* **2006**, *100*, 074510.

[29] Jadhav, P. J.; Brown, P. R.; Thompson, N.; Wunsch, B.; Mohanty, A.; Yost, S. R.; Hontz, E.; Voorhis, T. V.; Bawendi, M. G.; Bulović, V.; Baldo, M. A. Triplet Exciton Dissociation in Singlet Exciton Fission Photovoltaics. *Adv. Mater.* **2012**, *24*, 6169—6174.

[30] Ehrler, B.; Walker, B. J.; Böhm, M. L.; Wilson, M. W.; Vaynzof, Y.; Friend, R. H.; Greenham, N. C. In Situ Measurement of Exciton Energy in Hybrid Singlet-Fission Solar Cells. *Nat. Commun.* **2012**, *3*, 1019.

[31] Yang, L.; Tabachnyk, M.; Bayliss, S. L.; Böhm, M. L.; Broch, K.; Greenham, N. C.; Friend, R. H.; Ehrler, B. Solution-Processable Singlet Fission Photovoltaic Devices. *Nano Lett.* **2015**, *15*, 354–358.

[32] Johnson, J. C.; Nozik, A. J.; Michl, J. The Role of Chromophore Coupling in Singlet Fission. *Acc. Chem. Res.* **2013**, *46*, 1290–1299.

[33] Wu, Y.; Liu, K.; Liu, H.; Zhang, Y.; Zhang, H.; Yao, J.; Fu, H. Impact of Intermolecular Distance on Singlet Fission in a Series of TIPS Pentacene Compounds. *J. Phys. Chem. Lett.* **2014**, *5*, 3451–3455.

[34] Burdett, J. J.; Müller, A. M.; Gosztola, D.; Bardeen, C. J. Excited State Dynamics in Solid and Monomeric Tetracene: The Roles of Superradiance and Exciton Fission. *J. Chem. Phys.* **2010**, *133*, 144506.

[35] Zimmerman, P. M.; Bell, F.; Casanova, D.; Head-Gordon, M. Mechanism for Singlet Fission in Pentacene and Tetracene: From Single Exciton to Two Triplets. *J. Am. Chem. Soc.* **2011**, *133*, 19944–19952.

[36] Havenith, R. W.; de Gier, H. D.; Broer, R. Explorative Computational Study of the Singlet Fission Process. *Mol. Phys.* **2012**, *110*, 2445–2454.

[37] Chan, W.-L.; Berkelbach, T. C.; Provorse, M. R.; Monahan, N. R.; Tritsch, J. R.; Hybertsen, M. S.; Reichman, D. R.; Gao, J.; Zhu, X.-Y. The Quantum Coherent Mechanism for Singlet Fission: Experiment and Theory. *Acc. Chem. Res.* **2013**, *46*, 1321–1329.

[38] Wan, Y.; Guo, Z.; Zhu, T.; Yan, S.; Johnson, J.; Huang, L. Cooperative Singlet and Triplet Exciton Transport in Tetracene Crystals Visualized by Ultrafast Microscopy. *Nat. Chem.* **2015**, *7*, 785–792.

[39] Stern, H. L.; Musser, A. J.; Gelinas, S.; Parkinson, P.; Herz, L. M.; Bruzek, M. J.; Anthony, J.; Friend, R. H.; Walker, B. J. Identification of a Triplet Pair Intermediate in Singlet Exciton Fission in Solution. *Proc. Natl. Acad. Sci. U.S.A.* **2015**, *112*, 7656–7661.

[40] Dover, C. B.; Gallaher, J. K.; Frazer, L.; Tapping, P. C.; Petty II, A. J.; Crossley, M. J.; Anthony, J. E.; Kee, T. W.; Schmidt, T. W. Endothermic Singlet Fission Is Hindered by Excimer Formation. *Nat. Chem.* **2018**, *10*, 305–310.

[41] Thampi, A.; Stern, H. L.; Cheminal, A.; Tayebjee, M. J. Y.; Petty, A. J.; Anthony, J. E.; Rao, A. Elucidation of Excitation Energy Dependent Correlated Triplet Pair Formation Pathways in an Endothermic Singlet Fission System. *J. Am. Chem. Soc.* **2018**, *140*, 4613–4622.

[42] Marciniak, H.; Pugliesi, I.; Nickel, B.; Lochbrunner, S. Ultrafast Singlet and Triplet Dynamics in Microcrystalline Pentacene Films. *Phys. Rev. B* **2009**, *79*, 235318.

[43] Rao, A.; Wilson, M. W. B.; Hodgkiss, J. M.; Albert-Seifried, S.; Bässler, H.; Friend, R. H. Exciton Fission and Charge Generation and via Triplet and Excitons in and Pentacene/C60 Bilayers. *J. Am. Chem. Soc.* **2010**, *132*, 12698–12703.

[44] Zimmerman, P. M.; Zhang, Z.; Musgrave, C. B. Singlet Fission in Pentacene Through Multi-exciton Quantum States. *Nat. Chem.* **2010**, *2*, 648–652.

[45] Wilson, M. W. B.; Rao, A.; Clark, J.; Kumar, R. S. S.; Brida, D.; Cerullo, G.; Friend, R. H. Ultrafast Dynamics of Exciton Fission in Polycrystalline Pentacene. *J. Am. Chem. Soc.* **2011**, *133*, 11830—11833.

[46] Zeng, T.; Hoffmann, R.; Ananth, N. The Low-Lying Electronic States of Pentacene and Their Roles in Singlet Fission. *J. Am. Chem. Soc.* **2014**, *136*, 5755–5764.

[47] McDonough, T. J.; Zhang, L.; Roy, S. S.; Kearns, N. M.; Arnold, M. S.; Zanni, M. T.; Andrew, T. L. Triplet Exciton Dissociation and Electron Extraction in Graphene-templated Pentacene Observed with Ultrafast Spectroscopy. *Phys. Chem. Chem. Phys.* **2017**, *19*, 4809–4820.

[48] Refaely-Abramson, S.; da Jornada, F. H.; Louie, S. G.; Neaton, J. B. Origins of Singlet Fission in Solid Pentacene from an ab initio Green's Function Approach. *Phys. Rev. Lett.* **2017**, *119*, 267401.

[49] Hart, S.; Silva, W. R.; Frontiera, R. R. Femtosecond Stimulated Raman Evidence for Charge-transfer Character in Pentacene Singlet Fission. *Chem. Sci.* **2018**, *9*, 1242–1250.

[50] Pensack, R. D.; Ostroumov, E. E.; Tilley, A. J.; Mazza, S.; Grieco, C.; Thorley, K. J.; Asbury, J. B.; Seferos, D. S.; Anthony, J. E.; Scholes, G. D. Observation of Two Triplet-Pair Intermediates in Singlet Exciton Fission. *J. Phys. Chem. Lett.* **2016**, *7*, 2370–2375.

[51] Ramanan, C.; Smeigh, A. L.; Anthony, J. E.; Marks, T. J.; Wasielewski, M. R. Competition between Singlet Fission and Charge Separation in Solution-Processed Blend Films of 6,13-Bis(triisopropylsilylethynyl)pentacene with Sterically-Encumbered Perylene-3,4:9,10-bis(dicarboximide)s. *J. Am. Chem. Soc.* **2012**, *134*, 386–397.

[52] Walker, B. J.; Musser, A. J.; Beljonne, D.; Friend, R. H. Singlet Exciton Fission in Solution. *Nat. Chem.* **2013**, *5*, 1019–1024.

[53] Herz, J.; Buckup, T.; Paulus, F.; Engelhart, J. U.; Bunz, U. H. F.; Motzkus, M. Unveiling Singlet Fission Mediating States in TIPS-pentacene and its Aza Derivatives. *J. Phys. Chem. A* **2015**, *119*, 6602–6610.

[54] Pensack, R. D.; Tilley, A. J.; Parkin, S. R.; Lee, T. S.; Payne, M. M.; Gao, D.; Jahnke, A. A.; Oblinsky, D. G.; Li, P.-F.; Anthony, J. E.; Seferos, D. S.; Scholes, G. D. Exciton Delocalization Drives Rapid Singlet Fission in Nanoparticles of Acene Derivatives. *J. Am. Chem. Soc.* **2015**, *137*, 6790–6803.

[55] Tayebjee, M. J. Y.; Schwarz, K. N.; MacQueen, R. W.; Dvořák, M.; Lam, A. W. C.; Ghiggino, K. P.; McCamey, D. R.; Schmidt, T. W.; Conibeer, G. J. Morphological Evolution and Singlet Fission in Aqueous Suspensions of TIPS-Pentacene Nanoparticles. *J. Phys. Chem. C* **2016**, *120*, 157–165.

[56] Tamura, H.; Huix-Rotllant, M.; Burghardt, I.; Olivier, Y.; Beljonne, D. First-Principles Quantum Dynamics of Singlet Fission: Coherent versus Thermally Activated Mechanisms Governed by Molecular π Stacking. *Phys. Rev. Lett.* **2015**,

115, 107401.

[57] Stuart, A. N.; Tapping, P. C.; Schrefl, E.; Huang, D. M.; Kee, T. W. Controlling the Efficiency of Singlet Fission in 6,13-Bis(triisopropylsilylethynyl)pentacene/Polymer Composite Nanoparticles. *J. Phys. Chem. C* **2019**, Accepted, awaiting publication.

[58] Grieco, C.; Kennehan, E. R.; Rimshaw, A.; Payne, M. M.; Anthony, J. E.; Asbury, J. B. Harnessing Molecular Vibrations to Probe Triplet Dynamics During Singlet Fission. *J. Phys. Chem. Lett.* **2017**, *8*, 5700–5706.

[59] Lee, S.; amd Seok Il Jung, D. H.; Kim, D. Electron Transfer from Triplet State of TIPS-Pentacene Generated by Singlet Fission Processes to CH3NH3PbI3 Perovskitez. *J. Phys. Chem. Lett.* **2017**, *8*, 884–888.

[60] Pensack, R. D.; Grieco, C.; Purdum, G. E.; Mazza, S. M.; Tilley, A. J.; Ostroumov, E. E.; Seferos, D. S.; Loo, Y.-L.; Asbury, J. B.; Anthony, J. E.; Scholes, G. D. Solution-processable, Crystalline Material for Quantitative Singlet Fission. *Mater. Horiz.* **2017**, *4*, 915–923.

[61] Folie, B. D.; Haber, J. B.; Refaely-Abramson, S.; Neaton, J. B.; Ginsberg, N. S. Long-Lived Correlated Triplet Pairs in a π-Stacked Crystalline Pentacene Derivative. *J. Am. Chem. Soc.* **2018**, *140*, 2326–2335.

[62] Grieco, C.; Kennehan, E. R.; Kim, H.; Pensack, R. D.; Brigeman, A. N.; Rimshaw, A.; Payne, M. M.; Anthony, J. E.; Giebink, N. C.; Scholes, G. D.; Asbury, J. B. Direct Observation of Correlated Triplet Pair Dynamics during Singlet Fission Using Ultrafast Mid-IR Spectroscopy. *J. Phys. Chem. C* **2018**, *122*, 2012–2022.

[63] Lee, T. S.; Lin, Y. L.; Kim, H.; Pensack, R. D.; Rand, B. P.; Scholes, G. D. Triplet Energy Transfer Governs the Dissociation of the Correlated Triplet Pair in Exothermic Singlet Fission. *J. Phys. Chem. Lett.* **2018**, *9*, 4087–4095.

[64] Pensack, R. D.; Tilley, A. J.; Grieco, C.; Purdum, G. E.; Ostroumov, E. E.; Granger, D. B.; Oblinsky, D. G.; Dean, J. C.; Doucette, G. S.; Asbury, J. B.; Loo, Y.-L.; Seferos, D. S.; Anthony, J. E.; Scholes, G. D. Striking the Right Balance of Intermolecular Coupling for High-efficiency Singlet Fission. *Chem. Sci.* **2018**, *9*, 6240–6259.

[65] Korovina, N. V.; Das, S.; Nett, Z.; Feng, X.; Joy, J.; Haiges, R.; Krylov, A. I.; Bradforth, S. E.; Thompson, M. E. Singlet Fission in a Covalently Linked Cofacial Alkynyltetracene Dimer. *J. Am. Chem. Soc.* **2016**, *138*, 617–627.

[66] Ito, S.; Nagami, T.; Nakano, M. Rational Design of Doubly-bridged Chromophores for Singlet Fission and Triplet-triplet Annihilation. *RSC Adv.* **2017**, *7*, 34830–34845.

[67] Korovina, N. V.; Joy, J.; Feng, X.; Feltenberger, C.; Krylov, A. I.; Bradforth, S. E.; Thompson, M. E. Linker-Dependent Singlet Fission in Tetracene Dimers. *J. Am. Chem. Soc.* **2018**, *140*, 10179–10190.

[68] Wang, L.; Olivier, Y.; Prezhdo, O. V.; Beljonne, D. Maximizing Singlet Fission by Intermolecular Packing. *J. Phys. Chem. Lett.* **2014**, *5*, 3345–3353.

[69] Sanders, S. N.; Kumarasamy, E.; Pun, A. B.; Trinh, M. T.; Choi, B.; Xia, J.;

Taffet, E. J.; Low, J. Z.; Miller, J. R.; Roy, X.; Zhu, X.-Y.; Steigerwald, M. L.; Sfeir, M. Y.; Campos, L. M. Quantitative Intramolecular Singlet Fission in Bipentacenes. *J. Am. Chem. Soc.* **2015**, *137*, 8965–8972.

[70] Zirzlmeier, J.; Lehnherr, D.; Coto, P. B.; Chernick, E. T.; Casillas, R.; Basel, B. S.; Thoss, M.; Tykwinski, R. R.; Guldi, D. M. Singlet Fission in Pentacene Dimers. *Proc. Natl. Acad. Sci.* **2015**, *112*, 5325–5330.

[71] Ito, S.; Nagami, T.; Nakano, M. Design Principles of Electronic Couplings for Intramolecular Singlet Fission in Covalently-Linked Systems. *J. Phys. Chem. A* **2016**, *120*, 6236–6241.

[72] Lukman, S.; Chen, K.; Hodgkiss, J. M.; Turban, D. H. P.; Hine, N. D. M.; Dong, S.; Wu, J.; Greenham, N. C.; Musser, A. J. Tuning the Role of Charge-transfer States in Intramolecular Singlet Exciton Fission Through Side-group Engineering. *Nat. Commun.* **2016**, *7*, 13622.

[73] Zirzlmeier, J.; Casillas, R.; Reddy, S.; Brana Coto, P.; Lehnherr, D.; T Chernick, E.; Papadopoulos, I.; Thoss, M.; R Tykwinski, R.; M. Guldi, D. Solution-Based Intramolecular Singlet Fission in Cross-Conjugated Pentacene Dimers. *Nanoscale* **2016**, *8*, 10113–10123.

[74] Basel, B. S.; Zirzlmeier, J.; Hetzer, C.; Phelan, B. T.; Krzyaniak, M. D.; Reddy, S. R.; Coto, P. B.; Horwitz, N. E.; Young, R. M.; White, F. J.; Hampel, F.; Clark, T.; Thoss, M.; Tykwinski, R. R.; Wasielewski, M. R.; Guldi, D. M. Unified Model for Singlet Fission Within a Non-conjugated Covalent Pentacene Dimer. *Nat. Commun.* **2017**, *8*, 15171.

[75] Khan, S.; Mazumdar, S. Diagrammatic Exciton Basis Theory of the Photophysics of Pentacene Dimers. *J. Phys. Chem. Lett.* **2017**, *8*, 4468–4478.

[76] Trinh, M. T.; Pinkard, A.; Pun, A. B.; Sanders, S. N.; Kumarasamy, E.; Sfeir, M. Y.; Campos, L. M.; Roy, X.; Zhu, X.-Y. Distinct Properties of the Triplet Pair State from Singlet Fission. *Sci. Adv.* **2017**, *3*, e1700241.

[77] Thorsmølle, V. K.; Averitt, R. D.; Demsar, J.; Smith, D. L.; Tretiak, S.; Martin, R. L.; Chi, X.; Crone, B. K.; Ramirez, A. P.; Taylor, A. J. Morphology Effectively Controls Singlet-Triplet Exciton Relaxation and Charge Transport in Organic Semiconductors. *Phys. Rev. Lett.* **2009**, *102*, 017401.

[78] Renaud, N.; Sherratt, P. A.; Ratner, M. A. Mapping the Relation between Stacking Geometries and Singlet Fission Yield in a Class of Organic Crystals. *J. Phys. Chem. Lett.* **2013**, *4*, 1065–1069.

[79] Schrauben, J. N.; Ryerson, J. L.; Michl, J.; Johnson, J. C. Mechanism of Singlet Fission in Thin Films of 1,3-Diphenylisobenzofuran. *J. Am. Chem. Soc.* **2014**, *136*, 7363–7373.

[80] Eaton, S. W.; Miller, S. A.; Margulies, E. A.; Shoer, L. E.; Schaller, R. D.; Wasielewski, M. R. Singlet Exciton Fission in Thin Films of tert-Butyl-Substituted Terrylenes. *J. Phys. Chem. A* **2015**, *119*, 4151–4161.

[81] Arias, D. H.; Ryerson, J. L.; Cook, J. D.; Damrauer, N. H.; Johnson, J. C. Polymorphism Influences Singlet Fission Rates in Tetracene Thin Films. *Chem. Sci.* **2016**, *7*, 1185–1191.

[82] Margulies, E. A.; Logsdon, J. L.; Miller, C. E.; Ma, L.; Simonoff, E.; Young, R. M.; Schatz, G. C.; Wasielewski, M. R. Direct Observation of a Charge-Transfer State Preceding High-Yield Singlet Fission in Terrylenediimide Thin Films. *J. Am. Chem. Soc.* **2017**, *139*, 663–671.

[83] Sutton, C.; Tummala, N. R.; Beljonne, D.; Brédas, J.-L. Singlet Fission in Rubrene Derivatives: Impact of Molecular Packing. *Chem. Mater.* **2017**, *29*, 2777–2787.

[84] Wehner, J.; Baumeier, B. Intermolecular Singlet and Triplet Exciton Transfer Integrals from Many-Body Green's Functions Theory. *J. Chem. Theory Comput.* **2017**, *13*, 1584–1594.

[85] Le, A. K.; Bender, J. A.; Arias, D. H.; Cotton, D. E.; Johnson, J. C.; Roberts, S. T. Singlet Fission Involves an Interplay between Energetic Driving Force and Electronic Coupling in Perylenediimide Films. *J. Am. Chem. Soc.* **2018**, *140*, 814–826.

[86] Kolata, K.; Breuer, T.; Witte, G.; Chatterjee, S. Molecular Packing Determines Singlet Exciton Fission in Organic Semiconductors. *ACS Nano* **2014**, *8*, 7377–7383.

[87] Mou, W.; Hattori, S.; Rajak, P.; Shimojo, F.; Nakano, A. Nanoscopic Mechanisms of Singlet Fission in Amorphous Molecular Solid. *Appl. Phys. Lett.* **2013**, *102*, 173301.

[88] Akselrod, G. M.; Deotare, P. B.; Thompson, N. J.; Lee, J.; Tisdale, W. A.; Baldo, M. A.; Menon, V. M.; Bulović, V. Visualization of Exciton Transport in Ordered and Disordered Molecular Solids. *Nat. Commun.* **2014**, *5*, 3646.

[89] Xiaoyu, X.; Haibo, M. Opposite Anisotropy Effects of Singlet and Triplet Exciton Diffusion in Tetracene Crystal. *ChemistryOpen* **2016**, *5*, 201–205.

[90] Li, X.; Tang, M. L. Triplet Transport in Thin Films: Fundamentals and Applications. *Chem. Commun.* **2017**, *53*, 4429–4440.

[91] Lakowicz, J. R. *Principles of Fluorescence Spectroscopy*, 3rd ed.; Springer US, 2006.

[92] Roberts, S. T.; McAnally, R. E.; Mastron, J. N.; Webber, D. H.; Whited, M. T.; Brutchey, R. L.; Thompson, M. E.; Bradforth, S. E. Efficient Singlet Fission Discovered in a Disordered Acene Film. *J. Am. Chem. Soc.* **2012**, *134*, 6388–6400.

[93] Kasai, H.; Nalwa, H. S.; Oikawa, H.; Okada, S.; Matsuda, H.; Minami, N.; Kakuta, A.; Ono, K.; Mukoh, A.; Nakanishi, H. A Novel Preparation Method of Organic Microcrystals. *Jpn. J. Appl. Phys.* **1992**, *31*, L1132–L1134.

[94] Tuncel, D.; Demir, H. V. Conjugated Polymer Nanoparticles. *Nanoscale* **2010**, *2*, 484–494.

[95] Kasai, H.; Oikawa, H.; Okada, S.; Nakanishi, H. Crystal Growth of Perylene Microcrystals in the Reprecipitation Method. *Bull. Chem. Soc. Jpn.* **1998**, *71*, 2597–2601.

[96] Kurokawa, N.; Yoshikawa, H.; Hirota, N.; Hyodo, K.; Masuhara, H. Size-Dependent Spectroscopic Properties and Thermochromic Behavior in

Poly(substituted thiophene) Nanoparticles. *ChemPhysChem* **2004**, *5*, 1609–1615.

[97] Clafton, S. Synthesis of Conjugated Polymer Nanoparticles and Investigation into the Role of Conjugation Defects. Undergraduate Honours Thesis, The University of Adelaide, Department of Chemistry, 2008.

[98] Tapping, P. C. Theoretical and Spectroscopic Studies of Energy and Charge Transport in Organic Semiconductors. Ph.D. thesis, The University of Adelaide, Department of Chemistry, 2017.

[99] Fuemmeler, E. G.; Sanders, S. N.; Pun, A. B.; Kumarasamy, E.; Zeng, T.; Miyata, K.; Steigerwald, M. L.; Zhu, X.-Y.; Sfeir, M. Y.; Campos, L. M.; Ananth, N. A Direct Mechanism of Ultrafast Intramolecular Singlet Fission in Pentacene Dimers. *ACS Cent. Sci.* **2016**, *2*, 316–324.

[100] Mauck, C. M.; Hartnett, P. E.; Wu, Y.-L.; Miller, C. E.; Marks, T. J.; Wasielewski, M. R. Singlet Fission within Diketopyrrolopyrrole Nanoparticles in Water. *Chem. Mater.* **2017**, *29*, 6810–6817.

[101] Davis, N. J. L. K.; Allardice, J. R.; Xiao, J.; Petty, A. J.; Greenham, N. C.; Anthony, J. E.; Rao, A. Singlet Fission and Triplet Transfer to PbS Quantum Dots in TIPS-Tetracene Carboxylic Acid Ligands. *J. Phys. Chem. Lett.* **2018**, *9*, 1454–1460.

[102] Hu, J.; Xu, K.; Shen, L.; Wu, Q.; He, G.; Wang, J.-Y.; Pei, J.; Xia, J.; Sfeir, M. Y. New Insights into the Design of Conjugated Polymers for Intramolecular Singlet Fission. *Nat. Commun.* **2018**, *9*, 2999.

[103] Montero, R.; Martínez-Martínez, V.; Longarte, A.; Epelde-Elezcano, N.; Palao, E.; Lamas, I.; Manzano, H.; Agarrabeitia, A. R.; López Arbeloa, I.; Ortiz, M. J.; Garcia-Moreno, I. Singlet Fission Mediated Photophysics of BODIPY Dimers. *J. Phys. Chem. Lett.* **2018**, *9*, 641–646.

[104] Harada, T.; McTernan, H. L.; Pham, D.-T.; Lincoln, S. F.; Kee, T. W. Femtosecond Transient Absorption Spectroscopy of the Medicinal Agent Curcumin in Diamide Linked γ-Cyclodextrin Dimers. *J. Phys. Chem. B* **2015**, *119*, 2425–2433.

[105] Tapping, P. C.; Clafton, S. N.; Schwarz, K. N.; Kee, T. W.; Huang, D. M. Molecular-Level Details of Morphology-Dependent Exciton Migration in Poly(3-hexylthiophene) Nanostructures. *J. Phys. Chem. C* **2015**, *119*, 7047–7059.

[106] Torii, H. Time-Domain Calculations of the Polarized Raman Spectra, the Transient Infrared Absorption Anisotropy, and the Extent of Delocalization of the OH Stretching Mode of Liquid Water. *J. Phys. Chem. A* **2006**, *110*, 9469–9477.

[107] Schalk, O.; Brands, H.; Balaban, T. S.; Unterreiner, A.-N. Near-Infrared Excitation of the Q Band in Free Base and Zinc Tetratolyl-porphyrins. *J. Phys. Chem. A* **2008**, *112*, 1719–1729.

[108] Berera, R.; van Grondelle, R.; Kennis, J. T. M. Ultrafast Transient Absorption Spectroscopy: Principles and Application to Photosynthetic Systems. *Photosynth. Res.* **2009**, *101*, 105–118.

[109] Mark, J. E., Ed. *Polymer Data Handbook*; Oxford University Press, Inc., 1999.

[110] Kim, C. H.; Yaghmazadeh, O.; Tondelier, D.; Jeong, Y. B.; Bonnassieux, Y.;

Horowitz, G. Capacitive Behavior of Pentacene-based Diodes: Quasistatic Dielectric Constant and Dielectric Strength. *J. Appl. Phys.* **2011**, *109*, 083710.

[111] Vaklev, N. L.; Müller, R.; Muir, B. V. O.; James, D. T.; Pretot, R.; van der Schaaf, P.; Genoe, J.; Kim, J.; Steinke, J. H. G.; Campbell, A. J. High-Performance Flexible Bottom-Gate Organic Field-Effect Transistors with Gravure Printed Thin Organic Dielectric. *Adv. Mater. Interfaces* **2014**, *1*, 1300123.

[112] Izadnia, S.; Schonleber, D. W.; Eisfeld, A.; Ruf, A.; LaForge, A. C.; Stienkemeier, F. Singlet Fission in Weakly Interacting Acene Molecules. *J. Phys. Chem. Lett* **2017**, *8*, 2068–2073.

[113] Barford, W.; Bittner, E. R.; Ward, A. Exciton Dynamics in Disordered Poly(p-phenylenevinylene). 2. Exciton Diffusion. *J. Phys. Chem. A* **2012**, *116*, 10319–10327.

[114] Yamagata, H.; Norton, J.; Hontz, E.; Olivier, Y.; Beljonne, D.; Brédas, J. L.; Silbey, R. J.; Spano, F. C. The Nature of Singlet Excitons in Oligoacene Molecular Crystals. *J. Chem. Phys.* **2011**, *134*, 204703.

[115] Stuart, A. N. A Kinetic and Spectroscopic Analysis of Distance-dependent Singlet Fission in TIPS-Pentacene. M.Sc. thesis, The University of Adelaide, Department of Chemistry, 2017.

[116] James, D. T.; Frost, J. M.; Wade, J.; Nelson, J.; Kim, J.-S. Controlling Microstructure of Pentacene Derivatives by Solution Processing: Impact of Structural Anisotropy on Optoelectronic Properties. *ACS Nano* **2013**, *7*, 7983–7991.

[117] Thorley, K. J.; Finn, T. W.; Jarolimek, K.; Anthony, J. E.; Risko, C. Theory-Driven Insight into the Crystal Packing of Trialkylsilylethynyl Pentacenes. *Chem. Mater.* **2017**, *29*, 2502–2512.

[118] Abu-Sen, L.; Morrison, J. J.; Horn, A. B.; Yeates, S. G. Concentration- and Solvent-Dependent Photochemical Instability of 6,13-Bis(triisopropysilylethynyl)pentacene. *Adv. Opt. Mater.* **2014**, *2*, 636–640.

[119] Yost, S. R.; Lee, J.; Wilson, M. W. B.; Wu, T.; McMahon, D. P.; Parkhurst, R. R.; Thompson, N. J.; Congreve, D. N.; Rao, A.; Johnson, K.; Sfeir, M. Y.; Bawendi, M. G.; Swager, T. M.; Friend, R. H.; Baldo, M. A.; Voorhis, T. V. A Transferable Model for Singlet-Fission Kinetics. *Nat. Chem.* **2014**, *6*, 492–497.

[120] Min, C.-K.; Joo, T.; Yoon, M.-C.; Kim, C. M.; Hwang, Y. N.; Kim, D.; Aratani, N.; Yoshida, N.; Osuka, A. Transient Absorption Anisotropy Study of Ultrafast Energy Transfer in Porphyrin Monomer, Its Direct Meso–meso Coupled Dimer and Trimer. *J. Chem. Phys.* **2001**, *114*, 6750–6758.

[121] Wallin, S.; Davidsson, J.; Modin, J.; Hammarström, L. Femtosecond Transient Absorption Anisotropy Study on $[Ru(bpy)3]^{2+}$ and $[Ru(bpy)(py)4]^{2+}$. Ultrafast Interligand Randomization of the MLCT State. *J. Phys. Chem. A* **2005**, *109*, 4697–4704.

[122] Tian, X.; Zhou, L.; Chen, X.; Meng, Y.; Xiong, Z.; Zhou, X.; Zhang, Y. Nanoscale Exponential Distance Dependence and Electron-transfer Model for Intermolecular Singlet Exciton Fission Observed in Rubrene-doped Organic Films. *Org.*

Electron. **2017**, *50*, 429–434.

[123] Felfer, P.; Ceguerra, A.; Ringer, S.; Cairney, J. Detecting and Extracting Clusters in Atom Probe Data: A Simple, Automated Method Using Voronoi Cells. *Ultramicroscopy* **2015**, *150*, 30–36.